# SPECTROSCOPIC ELLIPSOMETRY OF PALLADIUM THIN FILMS

by

BRIAN THOMAS SULLIVAN

B.Sc., University of Alberta, 1980

M.Sc., University of British Columbia, 1982

A THESIS SUBMITTED IN PARTIAL FULFILMENT OF

THE REQUIREMENTS FOR THE DEGREE OF

DOCTOR OF PHILOSOPHY

in

THE FACULTY OF GRADUATE STUDIES

PHYSICS

We accept this thesis as conforming

to the required standard

THE UNIVERSITY OF BRITISH COLUMBIA

June 1987

4 6

PHYSICS

The University of British Columbia
2075 Wesbrook Place
Vancouver, Canada
V6T 1W5

Date: June 1987

# ABSTRACT

Spectroscopic ellipsometry is a nondestructive, ambient surface analysis technique for studying surfaces, interfaces and thin films. To take advantage of this method an automatic spectroscopic ellipsometer was designed and constructed for the microstructural characterization of thin films. This high precision instrument is capable of measuring in real–time the optical properties of bulk or thin film materials over the visible–UV region (1.5 – 6.0 eV). The microstructure of thin films can be determined from an effective medium theory analysis of the spectroellipsometric data to investigate how the film morphology evolves with varying preparation conditions and to determine the optimum deposition parameters.

In this thesis the pseudodielectric function of palladium films prepared by dc planar magnetron sputtering was measured while the substrate temperature, argon partial pressure and rf–induced substrate bias were varied independently during deposition. The film data are in excellent agreement with the effective medium theory of Sen, Scala, and Cohen, relevant for a random coated–particle microstructure where the grains are optically isolated from each other.

With increasing substrate temperature, the Pd volume fraction in the bulk was found to decrease slightly, while the rms microroughness of the film surface increased in magnitude. At $190°$C, the rms microroughness was $80 \pm 3\overset{\circ}{A}$ with the Pd volume fraction in the bulk region falling slightly to $97 \pm 1\%$ relative to the film deposited at $22°$C.

For argon partial pressures below a transition pressure, $P_t \simeq 15$ mTorr, the films consisted of densely packed grains, corresponding to the zone T in Thornton's structure zone model. Above this transition pressure, the films developed into a more voided columnar structure, characteristic of the zone 1 region. A microstructural analysis

indicated a general trend towards increased porosity and microroughness of the films with higher argon pressures. The zone 1 region was best described optically by a random coated–particle microstructure and the electron microscopy confirmed that for thin films prepared at argon pressures higher than $P_t$, the grains became isolated by void boundaries. The optical data could not distinguish whether or not the films were 2– or 3–dimensionally isotropic.

With increasing rf–induced substrate biasing, the Pd film microstructure was modified in a manner similar to that obtained by varying the substrate temperature alone. Significant resputtering of the Pd films occurred, varying from 2 to 11 Å/sec for bias voltages of $-550$ V to $-1375$ V, respectively. The measured deposition rate while bias sputtering was significantly higher than that expected upon the measured resputtering rate and several mechanisms were proposed to account for the enhancement in the deposition rate. The films were best characterized by a 2–dimensional isotropy which was supported by the columnar nature of the films observed by electron microscopy.

Finally, the dielectric function of the "best" palladium film is compared to optical constants of Pd previously reported in the literature for bulk and thin film specimens. While all the authors quote essentially the same values for the real part of the dielectric function, regardless of the preparation or measurement technique, the imaginary part differs up to a factor of two. Surface microroughness, bulk porosity and oxide layers are unable to account for the difference. A possible grain boundary scattering mechanism is suggested.

# TABLE OF CONTENTS

# List of Tables

# List of Figures

# CHAPTER I. SPECTROSCOPIC ELLIPSOMETRY

## A. INTRODUCTION

The objective of this thesis was the development of a spectroscopic ellipsometer for the microstructural characterization of thin films. Spectroscopic ellipsometry is an ambient, optical technique well suited for the investigation of surfaces, interfaces and thin films in terms of microstructural characterization, detection and evolution of oxide or contamination overlayers, bandstructure of solids, and so on. Within the last twenty years the field of ellipsometry has expanded greatly with the advent of mini- and microcomputers for data analysis and instrumentation control. Prior to the easy availability of fast and inexpensive computers, the measurement process was manually controlled, and therefore often tedious, and essentially limited to single wavelengths. Furthermore, the complexity of ellipsometric equations even for relatively simple physical systems can be computationally quite formidable, with the result that the scope of possible applications had been greatly limited. New photometric instruments have essentially revolutionized the field introducing an automatic, spectroscopic capability necessary for proper characterization of thin films and surfaces. As well, the computational difficulties of the equations are no longer a deterrent and experimental results can be analyzed in real-time, allowing observations of the growth of surface contamination, oxide layers, etc. , .

Within the last fifteen years sputter deposition has also increased in importance, as a versatile thin film preparation technique. The invention of magnetron sputtering has led to significantly higher deposition rates, for example, compared to ordinary diode sputtering. Similarly, dc- or rf-induced substrate biasing during deposition has introduced added control over the physical properties of thin films. Since the

1

microstructure of thin films are significantly influenced by the preparation conditions, it is of paramount importance to be able to characterize thin films in terms of their optical properties to determine the optimum deposition parameters for a particular application. Spectroscopic ellipsometry, as will be seen, is a natural choice for this deposition/microstructure investigation, in conjunction with other surface analysis techniques. The relatively fast measurement time of the automatic spectroellipsometer gives it an important interactive capability whereby a newly deposited film can be quickly characterized and the information gained then applied to the deposition of the next film.

In this thesis, the microstructure of palladium films prepared by dc magnetron sputtering was studied as the deposition conditions were varied. Palladium was selected due to its technological importance in the areas of thin film hybrid circuitry and microelectronics, because of its noble–like metal properties and also as there have been relatively few characterization studies of Pd thin films.

The remainder of this chapter involves a general discussion of the field of ellipsometry, current instrumentation and the motivation for choosing the spectroscopic rotating–analyzer ellipsometer (RAE) design. In Chapter II the polarization state of light is defined and certain conventions involving the reflection of light are stated. The experimental quantity of interest in ellipsometry, the complex reflectance ratio, is then defined along with a description of how it is measured by the RAE followed by the theoretical calculation of the reflectance ratio for several simple multilayer structures. Chapter III is concerned with the technical details of the RAE. A broad overview of the ellipsometer is first given followed by a detailed examination of the critical areas of the ellipsometer including the optical elements, hardware design, data acquisition and software control. A brief review of dc planar magnetron sputtering along with a

description of the deposition system used to prepare palladium films is presented at the end of the chapter. Chapter IV deals with the critical alignment and calibration of the RAE, discussing the theory of both procedures as well as their practical implementation. Then the precision and accuracy of the ellipsometer is examined, with the optimum operating conditions being outlined along with the precision achieved during typical measurements. Chapter V discusses first the theoretical basis for the characterization of thin films using spectroscopic ellipsometry. The steps involved in the optical microstructural analysis are then described along with the software implementation. Chapter VI is concerned with the characterization of palladium thin films deposited by planar magnetron sputtering under different preparation conditions. First, the measured dielectric function of the Pd films is compared to previous studies in the literature on the optical constants of thin film and bulk Pd specimens. Then the Pd film microstructure is investigated as the substrate temperature, argon partial pressure and rf-induced substrate biasing are varied independently during film deposition. Furthermore, the deposition process involving the uniformity and net deposition rates is examined in detail for bias sputtering.

## B. HISTORY

A brief review of the history of ellipsometry, both theoretical and experimental, will be given here to provide a perspective on the recent developments in ellipsometry. The historical background of the field is covered in more detail by Whittaker,[7] in reviews by Rothen,[8] Hall,[9] Winterbottom,[10] and in standard optics texts such as Hecht and Zajac.[11]

Ellipsometry involves the measurement and analysis of the change in the polarization state of light after reflection off a surface or transmission through a

material. The field of ellipsometry therefore can trace its beginnings back to the discovery by Malus [12] in 1808 that the polarization state of light was altered upon reflection. Brewster [13] soon after in 1815 empirically derived the law named after him relating the index of refraction of a material to the angle of incidence ("Brewsters angle") at which the electric field p-component (parallel to the plane of incidence) vanishes. Then in 1818, Fresnel [14] was able to describe light polarization in terms of transversely propagating waves which provided a satisfactory explanation of the observed experimental results up to that time.

Experimental studies of reflection off liquids and solids then began to take place and over the next forty years it became clear that Fresnel's equations based on an abrupt ambient-surface interface were inadequate in fully explaining all the observed phenomena. In particular, Jamin [15] in 1850 observed that the p-component of the reflected light did not always vanish at Brewster's angle and that linearly polarized light reflected off a liquid became elliptically polarized. Lorenz [16] was the first to appreciate that the actual interface region between two media might be finite in nature and was able to explain the experimental data in terms of a thin film on the surface of a liquid. Thus, an important connection had been established between light reflection and the physical nature of the reflecting surface. Eventually in 1889, Drude [17] derived using Maxwell's equations a general (and exact) equation dealing with the reflection of light off a surface covered by a film of arbitrary thickness. In doing so, he formulated the fundamental law of ellipsometry relating the change in the polarization state of light upon reflection from a surface to the physical properties of the surface. Due to the complexity of these equations, however, a first-order expansion in terms of the parameter $(d/\lambda)$, where d is the thickness of the film and $\lambda$ is the wavelength of light, was required to interpret the experimental data.

On the experimental side, optical polarizers and compensators required to modify and analyze the polarization of light had been around since the middle of the nineteenth century. Early experimenters such as Rayleigh,[18] Drude[19] and others were able to use these optical elements to great advantage in developing the field of ellipsometry. After Rayleigh and Drude's experimental and theoretical work, the study of thin films on solids and liquids became of primary interest. Gradually, the instrumentation improved resulting in higher precision and accuracy[20], and just as important, sample preparation techniques also advanced. The now classic method of null ellipsometry to determine the polarization state of light was developed whereby a quarter-wave plate retarder and an analzyer were each rotated until the light reflected off a surface was extinguished.[1] The quarter-wave plate converted elliptically polarized light to linearly polarized light which was then extinguished by crossing the transmission axis of the analyzer with the azimuthal angle of the polarized light. By recording the azimuthal angles of the compensator and analyzer, the polarization state of the light could then be calculated. However, the visual determination of the null point could be difficult to discern, limiting the precision of the method although halfshade devices were able to circumvent this problem to a certain extent to improve the sensitivity of the instruments. In 1945, Rothen[21] described a new method of measuring film thicknesses and he named the apparatus an *ellipsometer*, thus giving the field its present name. Soon thereafter, photomultipliers became available, greatly increasing the sensitivity and versatility of the null ellipsometer by photoelectric detection of the light flux.

With the introduction of modern computers, one was no longer limited to first- or second-order expansions of the exact equations which now could be solved numerically. The improvement in the experimental instrumentation also continued with

new ellipsometer configurations as seen in the first Ellipsometry Symposium [2] held in 1963. However, up to this point the ellipsometers were still mostly manually controlled with relatively slow response times. This changed with the first design of an automated photometric ellipsometer by Cahan and Spanier [22] in 1969 using analog detection techniques. Other automatic ellipsometer designs soon followed and in 1973 Aspnes [23] described the first automatic scanning spectroscopic rotating-analyzer ellipsometer using Fourier detection of the polarization state of the reflected light. Since the late seventies, spectroscopic ellipsometry has become an important surface analysis technique as will be seen in the next section. The development of automatic ellipsometers will be described more fully below.

## C. ADVANTAGES OF ELLIPSOMETRY

In general, the inherent characteristics of an optical probe, viz., its intensity and polarization state, are altered after reflection or transmission through an interface separating two media. Reflectometry deals with the measurement of the change in intensity, ellipsometry is concerned with the change of the polarization state of light upon reflection from a surface and the technique of polarimetry involves the measurement of both quantities. [28]

Ellipsometry has several advantages over reflectometry in determining accurate optical constants of solids. First, ellipsometry measures two data points per wavelength as opposed to only one in reflectance measurements. This means that both the real and imaginary parts of the complex index of refraction or the dielectric function can be determined at a single wavelength. In reflectometry, the reflectance of an opaque sample would have to be accurately measured over the far infrared and into the uv and then a Kramers-Kronig relationship applied to the data to determine the optical

properties in the visible region. Secondly, ellipsometry is a more inherently precise technique as it measures only the relative change in the polarization state as opposed to absolute intensities. For the same reason, ellipsometry is less sensitive to macroscopic (i.e. light scattering) imperfections on the surface of a sample compared to reflectometry, because the light is usually scattered outside the field of view and consequently does not affect the measurement. Ellipsometry, however, is very sensitive to thin overlayers on a surface or very thin interfacial regions and whether this is considered an advantage or not may depend on your point of view!

Therefore, ellipsometry lends itself very well to the investigation of a number of topics in a wide diversity of fields. Aspnes has recently reviewed[24 - 29] a number of current applications of ellipsometry including : studying real-time formation of overlayers,[1,27,80] thin interfacial layers in multilayer structures,[24,27] nondestructive depth profiling,[30,27] determination of critical points in the band structure of solids,[73] determining the bandgap of materials as a function of composition,[34] measuring the optical properties of semiconductors,[33] characterization of thin film microstructure including surface roughness,[28,81] determining how the microstructure of a-Si is affected by preparation conditions[78,31,32] high quality surface preparation[25] to name but a few examples.

## D. CURRENT INSTRUMENTATION

Ellipsometers can be broadly separated into two categories: null and photometric, depending on how the state of polarization of the reflected light is measured. In null ellipsometry, the azimuth angle of a compensator and an analyzer are varied until the reflected light is extinguished. In photometric systems, on the other hand, the polarization state is typically determined by the modulation of the reflected light as the azimuth angle of one or more of the polarizer, analyzer or compensator is rotated

continuously. In the last thirty years there has been a proliferation of different ellipsometer designs varying from the classic null ellipsometer and interferometric ellipsometers to ellipsometers with response times of the order of microseconds to picoseconds or those with beam sizes on the order of microns. The current instrumentation has been recently discussed by Azzam and Bashara [1] and in review articles by Hauge,[35,36] Aspnes,[29] Winterbottom[10] and Muller.[37]

The origin of the automated rotating-analyzer ellipsometer (RAE) using Fourier detection can be traced to Budde[38] in 1961. He showed that the modulation of light through a rotating-analyzer could be Fourier analyzed to obtain the polarization state of light and demonstrated the applicability of the method. The first instance of using a continuously rotating analyzer appears to be that of Kent and Lawson[39] in 1937, based upon a principle similar to that of the null ellipsometer except that the compensator was adjusted until the reflected light was completely circularly polarized. This condition was achieved by nulling the modulation in the light transmitted through the rotating-analyzer. Automation of ellipsometers began in earnest in the 1960's, and by 1969 Cahan and Spanier[22] had designed the first automated, photometric, high speed ellipsometer. While the principle was the same as in Budde's method they used an analog detection system, as did a design employed by Greef[40], and both systems had a spectroscopic capability. This was soon followed by an automatic polarization-modulated ellipsometer by Jasperson and Schnatterly[41] with an automated wavelength-scanning mechanism. Aspnes[23] in 1973 introduced the first fully automated spectroscopic rotating-analyzer ellipsometer using Fourier detection of the polarization state. Hauge and Dill[42] at the same time reported on a similar Fourier detection ellipsometer used to automatically measure film thicknesses at a single wavelength. Since that time automatic ellipsometers have dominated the field due to their high speed

and spectroscopic capability. However, the number of automated ellipsometers is still relatively few due to the their technical complexity, although this is now changing.

The decision to construct a photometric RAE instrument similar to Aspnes' design for this thesis was based on the following considerations. First, this instrument has a large spectral range, from 1.5 – 6.0 eV, over the visible–near UV optical region. This spectroscopic capability allows the ellipsometer to characterize a sample over the optical regions where intraband and interband transitions play a prominent role. Secondly, this instrument is technically the simplest, although as will be seen in Chapter III, the details can still get rather complicated! With this ellipsometer, the incident light upon the sample is linearly polarized and the reflected light passes through a rotating analyzer. As no compensator is required, the only wavelength dependent optical element is the sample itself. Thirdly, the RAE can be automated and thin film samples can be measured on a routine basis. The typical time to measure the dielectric function of a sample across the entire spectrum is approximately 20 minutes. Finally, the precision of a RAE is very good approaching $1 \times 10^{-5}$ in the measured dielectric function[43] and allowing the third derivative of the measured dielectric function to be computed.

The disadvantages of a RAE are that it cannot determine the handedness of the polarization or distinguish between depolarized and circularly polarized light.[29] Also its accuracy is limited by detector nonlinearities so that it is currently not as accurate as the null ellipsometer. These limitations will be addressed more fully in the chapters dealing with the theoretical and experimental aspects of the spectroellipsometer.

## E. LITERATURE

The standard text in the field is *Ellipsometry and Polarized Light* by Azzam and Bashara,[1] a comprehensive work covering the experimental and theoretical aspects of ellipsometry. Valuable reviews and articles can be found in the proceedings of the five Ellipsometry Symposiums[2-6] held to date and in articles by Neal[44,45] and Paik.[46] In the area of spectroscopic ellipsometry, Aspnes has written two excellent reviews[28,29] along with a number of articles[24-27] dealing with the applications of spectroellipsometry in a wide variety of areas. Review articles specific to a certain topic will be referenced in the relevant sections of the thesis.

# CHAPTER II. THEORY

## A. INTRODUCTION

This chapter is essentially a review of the basic theory of ellipsometry with regard to the measurement and analysis of the change in the polarization state of light upon reflection from a surface. First, the propagation of electromagnetic fields in matter will be reviewed followed by a section dealing with polarized light and its mathematical representation. Next, the complex reflectance ratio, the experimental quantity of interest in ellipsometry, is defined and its measurement by a rotating-analyzer ellipsometer is then described. Finally, the complex reflectance ratio is related to the physical properties of several simple, isotropic, multilayer structures.

There are many excellent reviews in the literature on the topics covered in this chapter. In particular, for a complete discussion on electromagnetic fields and polarized light the reader is referred to Shurcliff,[47] Jackson,[48] Born and Wolf,[49] Hecht and Zajac,[11] as well as the other references mentioned in the previous chapter.

## B. ELECTROMAGNETIC FIELDS IN MATTER

The classical interaction of light with matter can be described by Maxwell's equations, the constitutive equations relating the electromagnetic fields in matter, and the appropriate boundary conditions.[48] Assuming a linear, isotropic, nonmagnetic medium then,

$$D = \epsilon E, \tag{2.1a}$$

$$B = H \tag{2.1b}$$

where E and H are the electric and magnetic field strengths, respectively; D and B are the electric and magnetic flux densities, respectively, (cgs units); and $\epsilon$ is the

complex dielectric function. For mathematical simplicity, a complex representation of the fields will be used and it will be implicitly assumed that the real part of complex field components will be taken to obtain the true physical fields.

From Maxwell's equations and the above constitutive equations, the wave equation for an electromagnetic field propagating in a nonmagnetic medium is given by,

$$( \nabla^2 - (\epsilon/c^2)(\partial^2/\partial^2 t) )E = 0 \tag{2.2}$$

For $E$ with an $e^{-i\omega t}$ time dependence, $\epsilon(\omega) = \epsilon_1 + i\sigma/\epsilon_0\omega = \epsilon_1 + i\epsilon_2$, where $\epsilon_0$ is the free-space electric permittivity and $\sigma$ is the frequency dependent optical conductivity. Note that in the constitutive equation, $D = \epsilon E$, the imaginary part of the dielectric function, $\epsilon_2 = \sigma/\epsilon_0\omega$, results in the response $D$ being out of phase with respect to the applied field $E$. In this equation, Ohm's law, $J = \sigma E$ has been implicitly assumed where $J$ is the current density. An alternative formulation is to state Ohm's law explicitly in the constitutive equations and to use $D = \epsilon_1 E$.

## C. POLARIZED LIGHT

An electric field of a light wave propagating in a direction $k_i$ can be represented by two transverse, orthogonal field components. The relationship between the relative amplitude and phase of the two components characterizes the light wave in terms of a polarization state.

For a local right-handed Cartesian coordinate system with the z-axis parallel to the direction of propagation, the plane-wave solution to (2.2) is given by,[48]

$$E(r,t) = (\widetilde{E}_x \hat{x} + \widetilde{E}_y \hat{y}) e^{i(kz - \omega t)} \tag{2.3a}$$

where,

$$\widetilde{E}_x = E_x\, e^{-i\delta_x}, \tag{2.3b}$$

$$\widetilde{E}_y = E_y\, e^{-i\delta_y} \tag{2.3c}$$

are the complex field amplitudes and $\omega$ is the angular frequency of the monochromatic electric field. The tip of the electric field vector will, in general, trace out an ellipse in a plane normal to the propagation direction as shown in Fig. 2.1a, hence the term elliptically polarized light. The polarization state of the light can be specified by two parameters, viz., the *azimuth angle* Q of the major axis and the *ellipticity*, $\widetilde{a}$, where $|\widetilde{a}|$ = minor/major axis ratio, with the sign determined by the rotation direction of the electric field. The light is defined to be right-hand ($\widetilde{a} < 0$) or left-hand ($\widetilde{a} > 0$) polarized if the electric field rotates clockwise (cw) or counterclockwise (ccw), respectively, looking into the source. The azimuth angle is positive when measured ccw from a reference plane looking into the source.[29]

In ellipsometry, a convenient reference plane is the plane of incidence defined by the incident wavevector, $k_i$, and the normal to the reflecting surface. The two orthogonal electric field components are then taken to be $\widetilde{E}_p$ ($=\widetilde{E}_x$, TM mode) and $\widetilde{E}_s$ ($=\widetilde{E}_y$, TE mode) which are parallel and perpendicular to the plane of incidence, respectively. The eigenmodes of an optical element correspond to the orthogonal electric field components that are reflected (or transmitted) without a change in their polarization state. For isotropic optical elements, the eigenpolarizations are $\widetilde{E}_p$ and $\widetilde{E}_s$, while for a quarter-wave compensator the eigenpolarizations are right- and left-handed circularly polarized light (As will be seen later, for optically active polarizers the eigenpolarizations no longer correspond to linearly polarized light and corrections to the ellipsometry analysis are required).

The polarization state of the electric field can be defined as,

a)

$$|a| = \frac{E'_{oy}}{E'_{ox}} = \frac{minor\ axis}{major\ axis}$$

$$Q = azimuth\ angle$$

b)
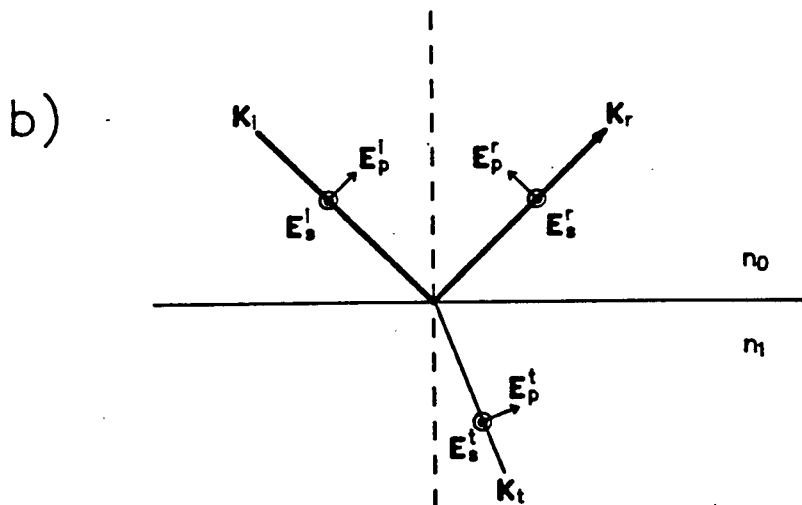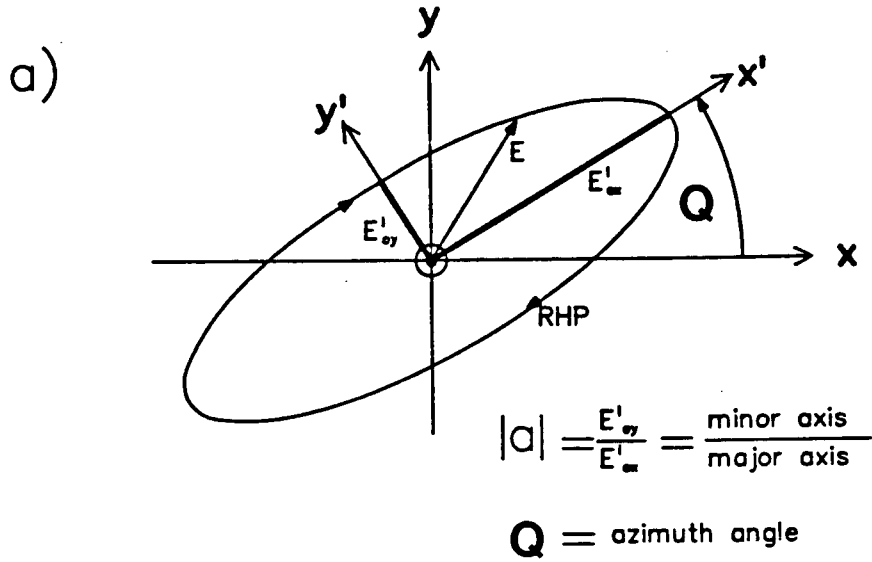
Figure 2.1. (a) Definition of polarization state of light. (b) Definition of incident, reflected and transmitted electric fields for s- and p-polarizations.

$$\chi = \tilde{E}_s / \tilde{E}_p = (E_s / E_p) \, e^{i(\delta_s - \delta_p)} \tag{2.4}$$

where $\chi$ is dependent only on the relative amplitude and phases of the p- and s-components.[1] For linearly polarized light, both $\tilde{E}_p$ and $\tilde{E}_s$ are in phase and $\chi$ is real while for right- and left-handed circularly polarized light, $\tilde{E}_s = -i\tilde{E}_p$ and $\tilde{E}_s = i\tilde{E}_p$, respectively, and $\chi$ is purely imaginary. In terms of the azimuth angle and the ellipticity, the polarization state is given by,[1]

$$\chi = \frac{\tan Q + i \cdot \tilde{a}}{1 - i \, \tilde{a} \cdot \tan Q} \tag{2.5}$$

For monochromatic electromagnetic fields, the light wave can be described as totally polarized since the two orthogonal electric field components have a constant amplitude and phase relationship between them; i.e., the field components are mutually coherent. A coherency time can be defined by the length of time in which the electric field exists in a definite polarization state. For incoherent light, the measurement time is greater than the coherence time, so the state of polarization changes rapidly and randomly. The incoherency in an ordinary light source arises from the fact that the light is emitted at random from many atoms, with no definite phase relationship between the light from the different atoms. This incoherent light is usually referred to as natural light and is essentially unpolarized, i.e., the state of polarization changes on the order of every $10^{-8}$ seconds. In general, a light beam is only partially polarized in the sense that the orthogonal field components are a mixture of coherent and incoherent light so that the degree of polarization of light can vary from being totally unpolarized to totally polarized.

The total polarization state of light, including the degree of polarization, can be represented by four parameters obtained by weighted time averages of the electric field

components. These *Stokes* parameters can be defined as follows:[11]

$$S = \{ S_0, S_1, S_2, S_3 \}$$

where

$$S_0 = <E_x^2> + <E_y^2> \qquad (2.6a)$$

$$S_1 = <E_x^2> - <E_y^2> \qquad (2.6b)$$

$$S_2 = <2E_x E_y \cos\delta> \qquad (2.6c)$$

$$S_3 = <2E_x E_y \sin\delta> \qquad (2.6d)$$

Here $\delta = \delta_x - \delta_y$, $E_x$ and $E_y$ are time dependent and $<>$ represents the time average. $S_0$ is the total intensity and $S_1$, $S_2$, and $S_3$ represent the degree of horizontally/vertically polarized light, $\pi/4$/$-\pi/4$ linearly polarized light (azimuth angle at $\pi/4$ and $-\pi/4$ with respect to the plane of incidence), and left-hand/ right-hand circularly polarized light, respectively. For example, if $\tilde{S}_1 = S_1/S_0$, then $-1 \leq \tilde{S}_1 \leq 1$, and for totally horizontally polarized light, $\tilde{S}_1 = +1$; for totally vertically polarized light, $\tilde{S}_1 = -1$; and for unpolarized light $\tilde{S}_1 = 0$. If the light is totally unpolarized, $S_1 = S_2 = S_3 = 0$, since $<E_x> = <E_y>$, while for totally polarized light, $S_0^2 = S_1^2 + S_2^2 + S_3^2$. The degree of polarization can therefore by defined as,[11]

$$V_p = ( S_1^2 + S_2^2 + S_3^2 )^{1/2} / S_0 \qquad (2.7)$$

so for totally unpolarized light, $V_p = 0$, while for totally polarized light, $V_p = 1$.

Another usual representation for a totally polarized electric field is given by the Jones vector,[1]

$$E = [ \tilde{E}_x, \tilde{E}_y ]^T \qquad (2.8)$$

where the time and spatial dependencies have been suppressed. Similarly, the effect of an optical element on the polarization state of an electric field can be specified by a

2 x 2 Jones matrix, J. Then the output polarization of an optical system consisting of a series of optical elements can be determined by simply multiplying the matrices of each individual optical element. If $E_{in}$ and $E_{out}$ are the input and output electric fields, respectively, of an optical system consisting of N optical elements then,

$$E_{out} = (J_N J_{N-1} \cdots J_2 J_1) \cdot E_{in} \tag{2.9}$$

The transmitted intensity through an optical system consisting of polarizers, compensators, etc., can therefore by calculated in a straightforward manner.

## D. COMPLEX REFLECTANCE RATIO

The complex Fresnel reflectance coefficients parallel $(r_p)$ and perpendicular $(r_s)$ to the plane of incidence are defined as follows,

$$r_p = \tilde{E}_p^r / \tilde{E}_p^i \tag{2.10a}$$

$$r_s = \tilde{E}_s^r / \tilde{E}_s^i \tag{2.10a}$$

Shown in Fig. 2.1b are the conventions used for the positive directions of the incident, reflected, and transmitted electric fields which define the signs of $r_p$ and $r_s$. The complex reflectance ratio, $\rho$, is defined by,[1]

$$\rho = r_p / r_s = (\tilde{E}_p^r/\tilde{E}_p^i)/ (\tilde{E}_s^r/\tilde{E}_s^i) = \chi^i / \chi^r \tag{2.11}$$

where $\chi^i$ and $\chi^r$ are the polarization states of the incident and reflected light, respectively. As $r_p$ and $r_s$ are generally not equal, the $\tilde{E}_p$ and $\tilde{E}_s$ components are reflected with different amplitude attenuations and phase differences, hence the change in the polarization state. For linearly polarized light incident upon a dielectric surface, the p and s components remain in phase resulting in the reflected light being linearly polarized, albeit with a different azimuth angle. In the case of an isotropic metallic surface, linearly polarized light will in general be reflected off elliptically polarized

unless the incident light is polarized parallel or perpendicular to the plane of incidence. The calibration of the ellipsometer is based upon this fact, and will be discussed later on. If $\chi^i$ is known and $\chi^r$ can be measured, then $\rho$ is characteristic of a surface for a given angle of incidence, $\phi$, and is the experimental quantity of interest. Traditionally, $\rho$ is written in the form

$$\rho = \tan\psi \, e^{i\Delta}, \qquad (2.12)$$

where $\tan\psi$ is the relative amplitude attenuation and $\Delta$ is the relative phase change between the incident and reflected polarization states. For reflection from a bare substrate, the pseudo–Brewster angle, $\phi_B$, is defined as the angle for which $\tan\psi$ is a minimum. The principal angle, $\phi_P$, is defined as the angle where $\Delta = -\pi/2$, and for a dielectric surface these two angles are the same. Typical values for $\tan\psi$ and $\Delta$ for various absorbing and dielectric surfaces can be found in the text by Azzam and Bashara.[1]

If the incident light is linearly polarized at an azimuth angle P, and $(Q, \tilde{a})$ is the measured polarization state of the reflected light, then from (2.5) and (2.11) the experimental $\rho$ is given by,[53]

$$\rho = \tan P \cdot \frac{\cot Q - i\,\tilde{a}}{1 + i\,\tilde{a} \cdot \cot Q} \qquad (2.13)$$

Here, Q and P are measured with respect to the plane of incidence and the polarizing elements are assumed to be isotropic.

## E. A NOTE ON CONVENTIONS

It is perhaps not an understatement to say that the possibilities for confusion in ellipsometry are somewhat endless due to all the different possible conventions. Equations derived under one set of conventions may be totally incompatible with equations derived under a different set of conventions. Muller [50] proposed a consistent set of conventions to eliminate the confusion. The conventions stated in the previous sections follow those used by Aspnes [29] and are similar to the Muller-Nebraska conventions [50 - 52] except that the standard physics convention, $e^{-i\omega t}$, is used instead of the optics convention, $e^{+i\omega t}$. With the standard physics convention, the complex dielectric function is given by $\epsilon(\omega) = \epsilon_1 + i\epsilon_2$, while the complex conjugate is obtained with the optics convention. In any case, once a convention has been decided upon, it should be strictly adhered to, for as P.S. Hauge [52] aptly quoted, "No man can serve two masters..."

## F. POLARIZATION STATE MEASUREMENT

The rotating-analyzer ellipsometer (RAE) measures the complex reflectance ratio photometrically by the modulation of the reflected light transmitted through the analyzer. [54] In this instrument, the quasi-monochromatic incident light is linearly polarized as it passes through the polarizer at an azimuth angle P. The light is then reflected off a sample and through an analyzer rotating at a constant angular frequency, $\omega_A$. The detected light signal is modulated at a frequency of $2\omega_A$, due to the optical symmetry of the analyzer, with the sinusoidal modulation depending upon the polarization state of the reflected light. It can easily be seen that the modulation is a maximum for linearly polarized light, while disappearing for circularly polarized or totally depolarized light. Furthermore, a rotation in the azimuth angle of the reflected

light results in a phase shift of the modulated light signal. Intuitively, therefore, one expects the polarization state information to be contained in the amplitude modulation and phase of the transmitted intensity.

If $A = \omega_A t$ is the azimuth angle of the analyzer with respect to the plane of incidence, then the electric field transmitted by the analyzer is,

$$E_A = \hat{E}_0 [ \cos(Q-A) + i\tilde{a}\sin(Q-A) ] \tag{2.14}$$

The transmitted intensity is then given by,

$$I_A = E_A \cdot E_A^* = I_0 \{ 1 + \alpha\cos 2A + \beta\sin 2A \} \tag{2.15}$$

where,[53]

$$2Q = \arctan(\beta / \alpha) \tag{2.16a}$$

$$\tilde{a} = \pm [ (1-\zeta) / (1+\zeta) ]^{\frac{1}{2}}, \tag{2.16b}$$

$$\zeta^2 = \alpha^2 + \beta^2 \tag{2.16c}$$

By computing the Fourier transform of the detected light signal and normalizing the Fourier coefficients with respect to the dc coefficient, the normalized second harmonic Fourier coefficients $\alpha$ and $\beta$ can be determined to obtain $( Q, |\tilde{a}| )$. This method is known as Fourier transform detection of the polarization state and will be discussed more fully in the experimental section. For linearly polarized light, $\tilde{a} = 0$, implies that $\zeta = 1$ so that the ac amplitude modulation is a maximum as expected, while for circularly polarized light $\tilde{a} = 1$ and $\zeta = 0$. In practice, the equations (2.16) will have to be modified to take into account the optical activity[53] of the analyzer and the low-pass filtering of the voltage signal, which phase shifts and attenuates the signal thereby causing an apparent change in the polarization state.[54]

It should be emphasized that in the RAE only the magnitude of $\tilde{a}$ can be

measured, so that the handedness of the reflected light cannot be measured. The ellipsometric parameters measured by a RAE are therefore $\tan\psi$ and $\cos\Delta$ and not $\Delta$ due to this indeterminate handedness in the reflected light. In spectroscopic ellipsometry, this is not a real limitation as the sign of $\tilde{a}$, and therefore that of $\sin\Delta$, can usually be determined as will be seen in the next section. Another limitation of the RAE is it cannot distinguish between circularly polarized light and depolarized light. For smooth reflecting surfaces, however, depolarization is essentially negligible and so this is not a major concern.[29]

## G. AMBIENT-SUBSTRATE SYSTEM

An electromagnetic wave incident upon an interface between two media, characterized by a discontinuity in the dielectric function, will be partially reflected due to the impedance mismatch at the interface. For an ideal ambient-substrate system, where the substrate has no surface roughness and is optically opaque, a single interface can be used to calculate the dielectric function of the substrate. First, the complex reflectance ratio for a single interface is calculated from Maxwell's equations, the constitutive equations and the usual boundary conditions. If $\epsilon_a$ and $\epsilon_s$ are the effective dielectric functions for the ambient and substrate respectively, then,[1,29]

$$\rho = \frac{\sin^2\phi - \cos\phi[(\epsilon_s/\epsilon_a) - \sin^2\phi]^{1/2}}{\sin^2\phi + \cos\phi[(\epsilon_s/\epsilon_a) - \sin^2\phi]^{1/2}} \qquad (2.17)$$

where $\phi$ is the angle of incidence. Thus, knowing $\rho$, $\epsilon_s$ can be solved,

$$\epsilon_s/\epsilon_a = \sin^2\phi + \sin^2\phi \cdot \tan^2\phi[(1-\rho)/(1+\rho)]^2 \qquad (2.18)$$

If the surface being measured is analyzed under the assumption that it contains no overlayers (oxide or contamination layers), surface roughness, porosity, etc., then the

value calculated using (2.18) is known as the pseudodielectric function [28] and is represented by $<\epsilon_s>$. It is convenient sometimes to plot the the experimental data, $\rho$, in the form of the pseudodielectric function as will be seen later.

As mentioned previously, only $\cos\Delta$ is determined from a ellipsometric measurement on a RAE, but for an absorbing (metallic) surface the following restrictions on $\rho$ apply,[29]

$$0 \leq \tan\psi \leq 1 \tag{2.19a}$$

$$-\pi \leq \Delta \leq 0 \tag{2.19b}$$

so that $\Delta$ is completely determined. In terms of the ellipticity $\tilde{a}$ of the reflected light, this corresponds to the condition,

$$\tilde{a} \cdot \tan P \geq 0 \tag{2.20}$$

so for $\tan P \geq 0$, the light reflected off a bare, absorbing substrate is left-handed polarized.

## H. AMBIENT-FILM-SUBSTRATE SYSTEM

If the substrate now has an overlayer on it, the calculation of the complex reflectance ratio has to take into account two interfaces and the multiple reflections occurring in the overlayer. The theoretical complex reflectance ratio for this system is given by,[1,29]

$$\rho = \tilde{r}_p / \tilde{r}_s, \tag{2.21a}$$

where,

$$\tilde{r}_\nu = \frac{r_{\nu,af} + r_{\nu,fs} \cdot \exp(i2\beta)}{1 + r_{\nu,af} r_{\nu,fs} \cdot \exp(i2\beta)} \quad , \quad \nu = p,s \tag{2.21b}$$

and,

$$\beta = 2\pi(d/\lambda)[\epsilon_f - \epsilon_a \sin^2 \phi]^{1/2} \qquad (2.21c)$$

is the film phase thickness and d is the overlayer thickness. The complex Fresnel coefficients $r_{\nu,af}$ and $r_{\nu,fs}$, $\nu = p,s$, correspond to the ambient-film and film-substrate interface, respectively, and $\epsilon_f$ is the dielectric function of the film.

Since only two data points are measured at a given wavelength, only two unknowns can be solved for in the above equation. Assuming that $\epsilon_s$ is known, then for a transparent film ($\epsilon_{2f}=0$), the film's index of refraction and the thickness can be deduced. Alternatively, if the film is partially absorbing and the film thickness is known, then $\epsilon_f$ can be solved.[55-59]

Note that no restrictions can be made on $\rho$ for this system, so that the handedness of the reflected light must be determined in a different manner. Spectroscopically, the handedness of the reflected light off a transparent film can be determined from the observation that the sign of $\sin\Delta$ is opposite to the sign of the first derivative of $\tan\psi$.

These results can also be extended to an arbitrary number of isotropic or anisotropic planar layers[60] to determine the theoretical complex reflectance ratio for any multilayer structure, with the most general being that of Lin-Chung and Teitler.[61] The optical characterization of thin films and substrates using spectroscopic ellipsometry will be discussed in Chapter V.

# CHAPTER III. EXPERIMENTAL DETAILS

> "... But have you ever noticed one encouraging thing about me, Marilla? I never make the same mistake twice."
>
> "I don't know as that's much benefit when you're always making new ones."
>
> "Oh, don't you see, Marilla? There *must* be a limit to the mistakes one person can make, and when I get to the end of them, then I'll be through with them. That's a very comforting thought."
>
> *"Anne of Green Gables"*
> Lucy C. Montgomery

## A. INTRODUCTION

This chapter describes the rotating-analyzer ellipsometer that was designed and constructed as part of this thesis. The design was based upon that of Aspnes and Studna [54] whose work has been at the forefront in the field of spectroscopic ellipsometry. An overview of the ellipsometer is first given and then the various components of the ellipsometer are discussed in detail. The technical aspects of an automatic spectroellipsometer involve the fields of optics, electronics, mechanical hardware, computer interfacing and real-time software control. Therefore, by necessity, the technical descriptions will sometimes be brief in nature due to the wide diversity of topics. In the last section, a brief review of the sputtering process is also given along with a description of the dc planar magnetron sputtering system used to prepare the palladium thin films.

## B. OVERVIEW

The optical layout of the rotating-analyzer spectroellipsometer is shown in Fig. 3.1, based upon the design of Aspnes and Studna. [23,53,54,62,64] The light source is a 75W Xenon short-arc lamp providing a continuous broadband spectrum from 185 nm

# AUTOMATIC SPECTROSCOPIC ELLIPSOMETER
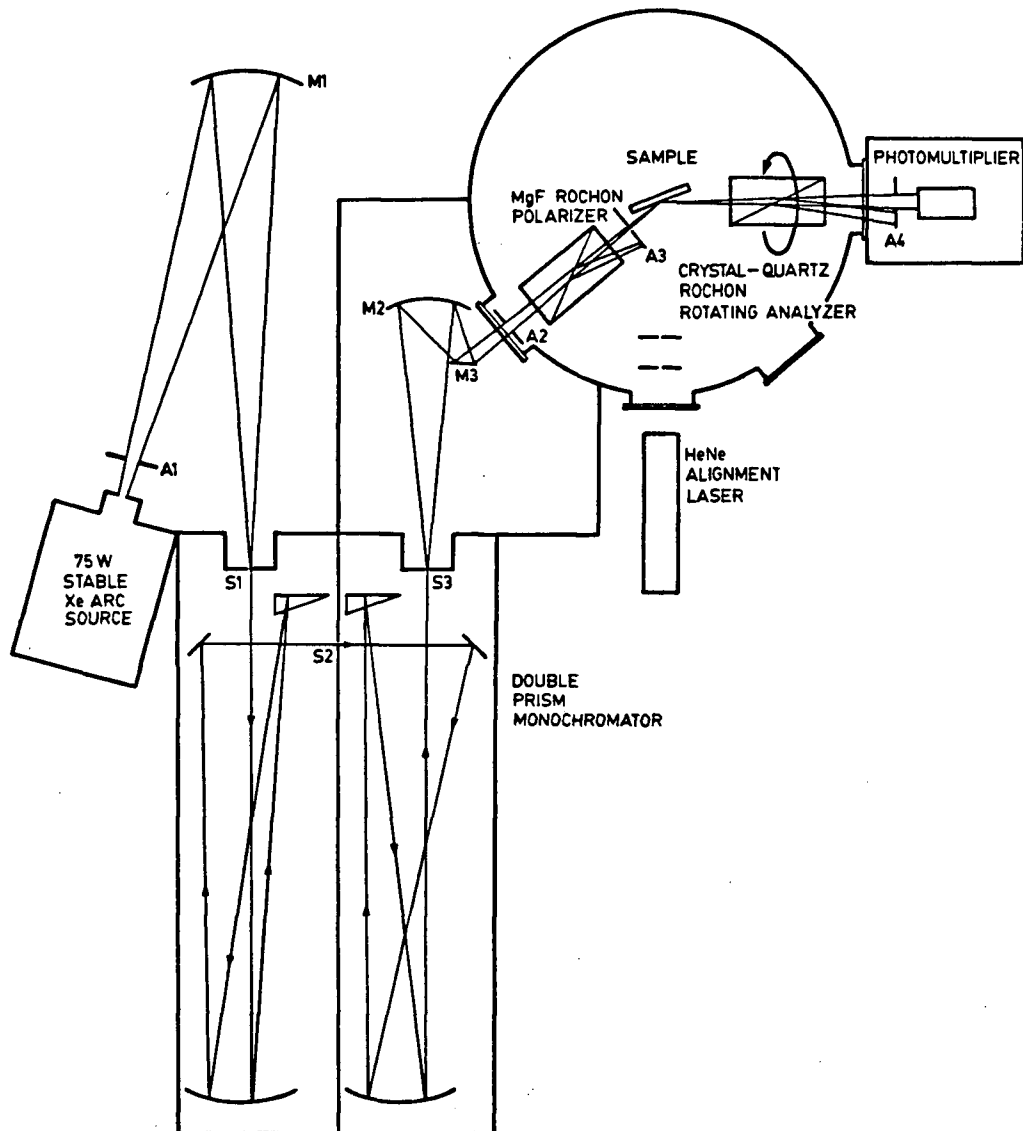


Figure 3.1. Optical layout of automatic spectroscopic ellipsometer.

into the infrared. The light is collected by a 20 cm focal mirror and focussed on the entrance slit of a double-prism monochromator (Cary-15). Quasi-monochromatic light leaves the exit slit through a shutter and is then reflected by transfer optics through the polarizer and focussed onto the sample holder. The incident light is therefore in a known polarization state when it is reflected off the sample at an angle of incidence of 67.50°. The reflected light then travels through a rotating analyzer and is detected by a photomultiplier tube.

Fourier transform detection of the polarization state of the reflected light is used as described in the previous chapter. Therefore, in the data acquisition process the detector output current signal has to be sampled at uniform intervals and signal averaged. Furthermore, to ensure maximum precision and accuracy, critical components in the ellipsometer have to be stabilized. In the following sections, the individual components comprising the ellipsometer system will be described along with the automation of the ellipsometer. The block diagram of the ellipsometer is shown in Fig. 3.2.

## C. ELLIPSOMETER CHAMBER

The polarizer, sample holder and analyzer are mounted inside a light-tight chamber, 60 cm in diameter and 25 cm in height, with five access ports. The light beam from the arc lamp, via the monochromator and transfer optics, enters through the first port and may travel either straight-through the chamber (no sample), or else exit through another port after reflection from a sample. The light from an alignment laser, mounted outside the chamber, enters through another port at an angle of 22.5° with respect to the first port. The photomultiplier can be attached onto either exit port, and will be described in more detail later on. The last port is used for electrical

| | | INTERACTIVE SOFTWARE |
|---|---|---|
| | | -Scan Control |
| | SAGE IV | -System Calibration |
| | Computer | -Graphics |
| | | -Signal Processing |

**Device Control Bus (Interrupt Driven)**

| 16 Bit Absolute Shaft Encoder | Incident Polarization Azimuthal Angle | | | | | Frequency Synthesizer |

| Shutter | Angle of Incidence | Monochromator Wavelength | DAC (Controls PMT HV Supply) | Power Amplifier |

BAGS OF LIGHT →

| PMT (1650-8500Å) | Program-mable HV Power Supply | Analyzer (4000 R.P.M. Hysteresis Synchronous Motor) |

Anode Current (Signal)

| Preamp. (I-V Converter) | Nonlinearity Feedback | Shaft Encoder (256 pulses/rev.) |

Triggers ~60μsec.

| Sample and Hold (S/H) | 16 Bit ADC (5 volt FSR, ~17μsec.) |

Figure 3.2. Block diagram of spectroellipsometer.

connections and a small port in the bottom of the chamber is used as a feedthrough for a $N_2$ line and a vacuum line. Underneath the chamber are four adjustable legs for adjusting the tilt and height of the chamber. The base of the chamber has a grid of holes spaced 2.5 cm apart for attaching further optical elements or accessories as needed. The inside of the chamber has been blackened wherever possible to reduce reflections of any scattered or stray light. As well, an interlock in the chamber turns off the photomultiplier tube if the lid is removed from the chamber by accident during the course of a measurement.

## D. INDIVIDUAL COMPONENTS

### 1. Light Source

The light source selected for the ellipsometer was a current-stabilized, convection-cooled, 75W Xenon short-arc lamp providing a continuous broadband spectrum from 185 nm to 1000 nm. The Hamamatsu lamp (L2174) was chosen for its high stability with typical fluctuations of $\simeq$ 0.3% p-p along with a Hamamatsu power supply C2177 with a highly regulated output current to operate the lamp.

When first set up, a fan was used to air cool the arc lamp housing; however, the fan vibrations introduced a 60 Hz ripple on the output light intensity. As a result, due to either the vibrations or possibly air density fluctuations, the precision of the ellipsometer decreased by about a factor of 20 compared with no forced air cooling. Therefore, the low power arc lamp was operated without any forced air cooling and no detrimental effects were observed

Also, when initially setting up the light source, the rf trigger starting of the arc lamp posed many difficulties. Due to poor rf shielding along the cables from the

power supply to the arc lamp housing and also on the input power line, there was a good chance of the IC's in nearby electronic devices (including the computer) being destroyed whenever the arc lamp was started. Proper shielding of all the cables and the arc lamp housing was required to eliminate this problem.

## 2. Monochromator

A double-prism Cary-15 monochromator with a spectral range of 185 nm to 800 nm was modified for use in the ellipsometer. This type of monochromator (or a foreprism/grating model) is absolutely crucial in automatic spectroscopic ellipsometry for two reasons. In a single element monochromator, the incident light can be scattered off either the grating or prism and pass through the exit slit. While this white light background may be negligible in the visible region of the spectrum, it can easily overcome any light signal in the near-UV region, especially if any of the optical components are weakly transmitting in the UV. Thus another dispersion element (usually a foreprism in order to maintain a larger spectral range) is used along with an intermediate slit to reduce the stray light component by several orders of magnitude. If a grating is used as a dispersive element, then a foreprism is also required to eliminate any second or higher order light from the optical spectrum. The dielectric function of silicon shown in Fig. 3.3 was measured with a single grating monochromator and then with the Cary-15. The difference at either end of the spectrum is dramatic, with the "infrared catastrophe" due to the second order UV-light and the "uv catastrophe" due to the stray light.

To rotate the scanning mechanism, a computer controlled stepping motor was added to the monochromator. The resolution of one motor step corresponded to 0.25 Å and the wavelength range from 200 nm to 800 nm could be scanned in
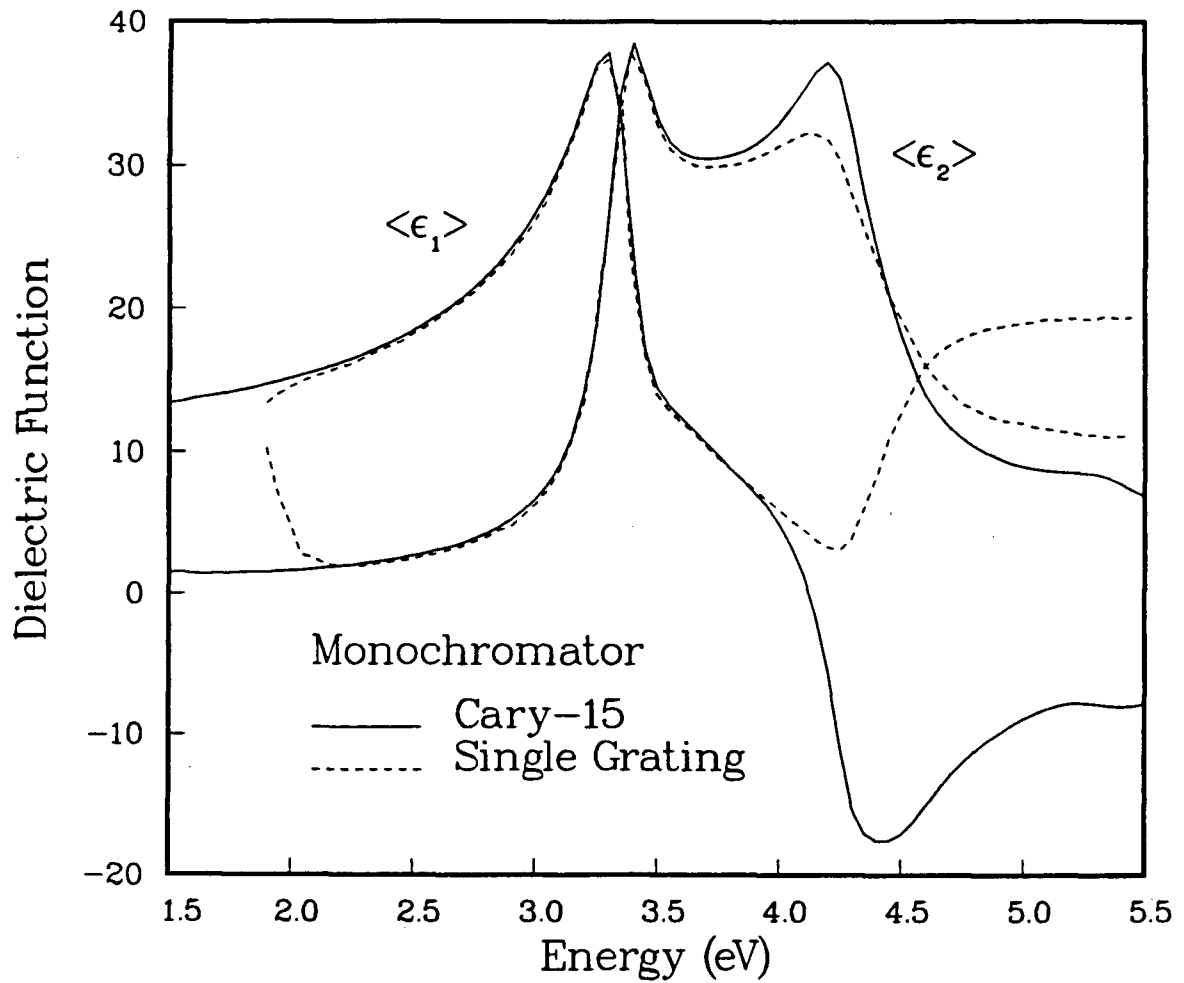
Figure 3.3. Comparison of dielectric function of Si measured on two different monochromators. The single grating monochromator without rejection of higher order spectra and no stray light suppression.

approximately 12 seconds. The slit width could be manually adjusted from 0 to 3 mm, with a typical width being 0.2 mm. A computer controlled shutter was also added to the exit port of the monochromator in order to block the light signal for part of the measurement cycle.

*a. Calibration*

A germicidal lamp, which has a strong, sharp, mercury line at 2536.52 Å was used to calibrate the monochromator. The current wavelength of the monochromator, displayed on a digital wheel readout attached to the scanning mechanism drive, was used to manually position the monochromator to the peak of this mercury line. The theoretical wavelength was then entered into the computer and the wavelength of the monochromator was thereafter obtained by software and stored permanently in a file whenever changed. The stepping motor on the monochromator was calibrated only in one direction because of the backlash of the gears.

## 3. Transfer Optics

The optics used to transfer the light from the source to the monochromator and subsequently to the sample holder were $MgF_2$ coated Al mirrors. The overcoat is necessary to preserve the high UV-reflectance properties of the Al mirror which would otherwise deteriorate with time. Concave mirrors, rather than lenses, with a focal length of 20 cm were used to focus the light as achromatic lenses have a limited spectral range, while the focal length of a quartz lens can vary by more than 1 cm over the 200 nm to 800 nm wavelength interval. The beam area of the light incident at the sample holder was approximately 2 mm in diameter.

## 4. Rochon Prism Polarizers

In nature, many crystals are *optically anisotropic*, i.e., the propagation of light through the crystal depends upon its orientation.[1,11,51,65,66] The anisotropy arises out of the lower symmetry of the atomic arrangement in the crystal and for uniaxial crystals such as crystal quartz, calcite, $MgF_2$, etc., an *optic axis* can be defined as the direction normal to a plane in which the atoms are arranged symmetrically. These uniaxial crystals are *birefringent* due to the different indices of refraction for directions parallel and perpendicular to the optic axis. The propagation of light through these crystals can be characterized depending upon the polarization of the light with respect to the optic axis. An ordinary−wave (o−wave) corresponds to light with the electric field linearly polarized perpendicular to the optic axis (or alternatively, parallel to the plane of symmetry) while an extraordinary−wave (e−wave) has the electric field polarized parallel to the optic axis (Fig. 3.4a). Hence, the o− and e−waves have indices of refraction $n_o$ and $n_e$, respectively, and the two waves propagate at different speeds. It is this asymmetry which forms the basis of many different polarizing devices.

One important type of polarizer, and that selected for the ellipsometer, is the Rochon prism beam−splitting device where two prisms of identical birefringent crystal are optically contacted together at a certain wedge angle, $\phi$. The "A" and "B" prisms, corresponding to the optic axes of the prisms being oriented parallel and perpendicular to the light propagation direction, respectively, are shown in Fig. 3.4a. First, the case where the polarizer is oriented such that the light is incident upon the face of the "A" prism is considered. At normal incidence, the light enters the polarizer undeviated and both orthogonal polarizations of the light form an o−wave. At the interface however, the incident light component polarized parallel to the optic axis in the "B" prism changes from an o−wave to an e−wave. This polarization component therefore

# ROCHON PRISM POLARIZERS

**POLARIZER**

$n_e > n_o$

(a)

**ANALYZER**

$n_e > n_o$

(b)
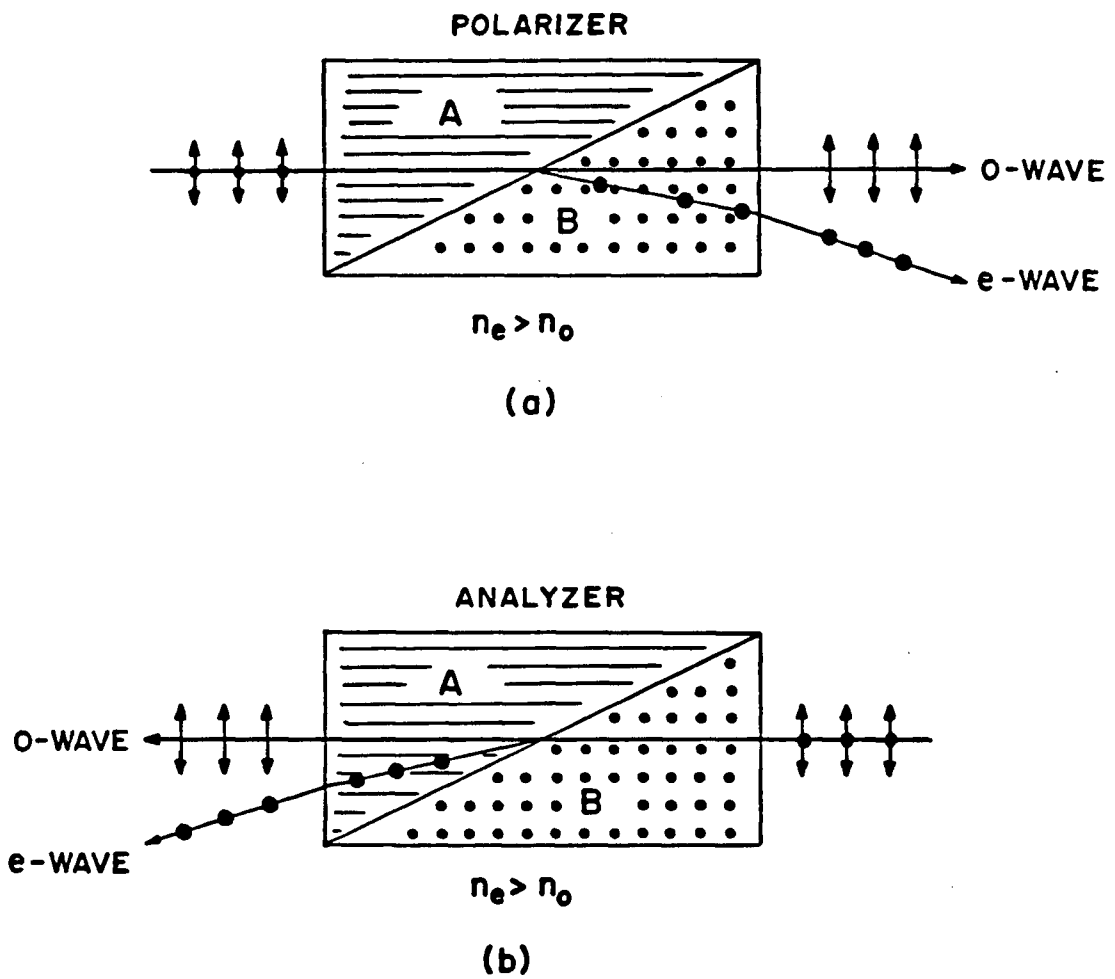
Figure 3.4. Separation of orthogonally linearly polarized light incident upon (a) prism A and (b) prism B.

sees a change in the index of refraction at the interface and is deviated. The polarization component of the incident light perpendicular to the optic axis of the "B" prism passes through undeviated. An alternative view is that the undeviated beam always remains polarized parallel to the plane of symmetry of the crystal in both prisms of the polarizer. In any case, two beams of orthogonally linearly polarized light exit the polarizer, with one beam deviated and the other undeviated. The deviation angle depends upon the difference in the index of refraction for the o- and e-waves at a given wavelength of light and the wedge angle of the two pieces. If the incident light enters the polarizer through the "B" prism, as in Fig. 3.4b, the situation described above remains essentially the same for $MgF_2$, but not for quartz, as seen in the next section. At normal incidence, both the o- and e-waves are undeviated but since $n_o > n_e$ (for quartz), the "B" prism acts as a retarder. However, as the orthogonal polarizations are separated at the interface, this phase change does not affect the operation of the polarizer.

The advantages of the Rochon beam-splitting polarizer include its high extinction ratio ($\simeq 10^6$) and a wide spectral range when constructed out of $MgF_2$ or quartz crystals. The disadvantage is the need to separate out the unwanted beam, but this is usually not a problem. Calcite polarizers are not recommended for spectroscopic ellipsometry as they transmit very little UV light for wavelengths under 300 nm.

*a. Optical Activity*

Crystal quartz has an additional property, *optical activity*, due to its left or right-handed helical crystal symmetry.[65] In optically active substances, the azimuth angle of linearly polarized light is rotated after propagating a distance parallel to the optic axis. For quartz, the rotation is 21.7° per mm at a wavelength of 530 nm. For

propagation directions off the optic axis, the optical activity drops quickly but a small degree of activity still exists even for propagation perpendicular to the optic axis.

For a Rochon prism the optical activity is actually beneficial in reducing systematic errors in ellipsometry,[53] however the polarizer has to be properly oriented depending on its application. For a polarizer, with the incident light unpolarized, the light must enter through the "A" prism first or else the output beam from the polarizer will remain essentially unpolarized. This is because for a light beam with a finite cross-section the path length traversed through the "A" prism will vary along the cross-section of the beam. Therefore, for a beam exiting through the "A" prism, the degree of azimuthal rotation of the linearly polarized light will vary substantially across the beam cross-section resulting in a pseudo-depolarized output beam. Since this pseudo-depolarization helps minimize any polarization sensitivities in a photomultiplier tube, crystal quartz was chosen for the analyzer. Thus for a properly oriented analyzer, the light must enter through the "B" prism first, where there is minimal optical activity, and exit the "A" prism. However, due to the small optical activity component in the "B" prism, the eigenpolarizations of the analyzer no longer correspond to orthogonally linear polarized light. A small correction must therefore be made to the analysis and this is addressed in the next chapter.

## 5. Polarizer

A $MgF_2$ Rochon polarizer, which is transparent across the spectral range from 140 nm to 7000 nm, was selected as the polarizer for the ellipsometer. For the nominally undeviated beam, any actual deviation is under 1/2 minute of arc while the minimum deviation angle for the other beam is $4.6°$ at $\lambda = 546$ nm. The output polarization quality of the $MgF_2$ polarizer changed dramatically depending on which face the light

was incident upon, although the two faces should be symmetric since $MgF_2$ is not optically active. With light incident upon one side of the polarizer, the output beams were not completely orthogonally linearly polarized and there was scattered light exiting the polarizer. After turning the polarizer around by $180°$, however, there were no problems and the two output beams were completely orthogonally polarized. The reason for this asymmetry is not known.

## a. Mechanical Design

The polarizer has a clear aperture of 9 x 12mm and is fixed inside a cylindrical housing. This housing is mounted inside a cylindrical brass carrier as shown in Fig. 3.5a. The polarizer is seated against one end of the carrier and its orientation relative to the carrier can be adjusted by three set screws as discussed in the next section on alignment.

The carrier, supported by two bearings on each end, is mounted inside an aluminum housing as shown in Fig. 3.6. The polarizer is rotated using a stepping motor and a worm/gear arrangement. The stepping motor, with a resolution of 400 steps/revolution, was mounted vertically, with a worm attached to its shaft. The worm is connected to an anti-backlash worm gear attached to the shaft of the polarizer carrier and the gear ratio of 140 : 1 gives a polarizer azimuth angle stepping resolution of $0.006°$. Various combinations of worms and worm gears were tried to reduce the variation in the azimuth stepping angle, until the best combination was found.

Mounted on the other end of the polarizer carrier shaft is a standard gear which rotates (1:1) an anti-backlash gear attached to a 16-bit ($0.005°$ resolution) absolute shaft encoder. The shaft encoder can be interrogated by the computer to

POLARIZER
ORIENTATION
ADJUSTMENT

BEARING

POLARIZER

CARRIER

**(a)**

POLARIZER
CARRIER

LASER

**(b)**
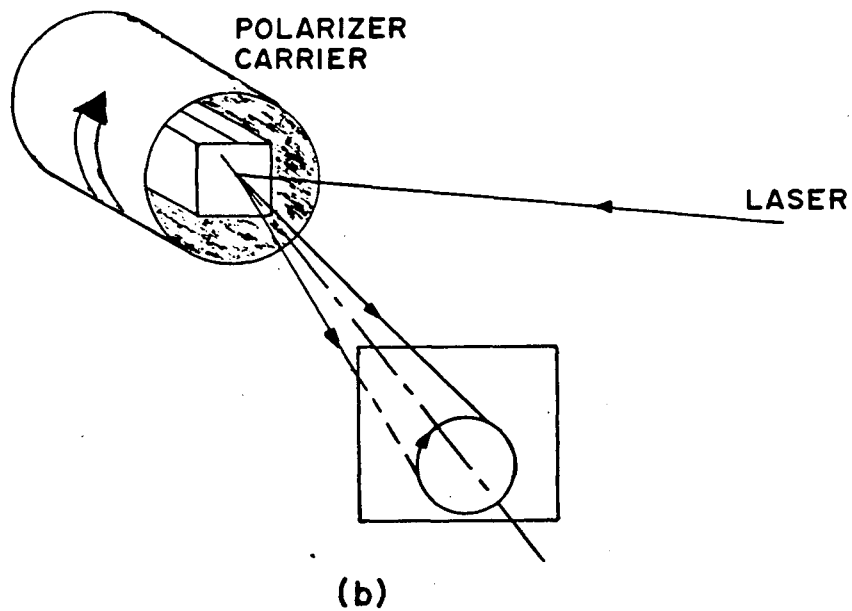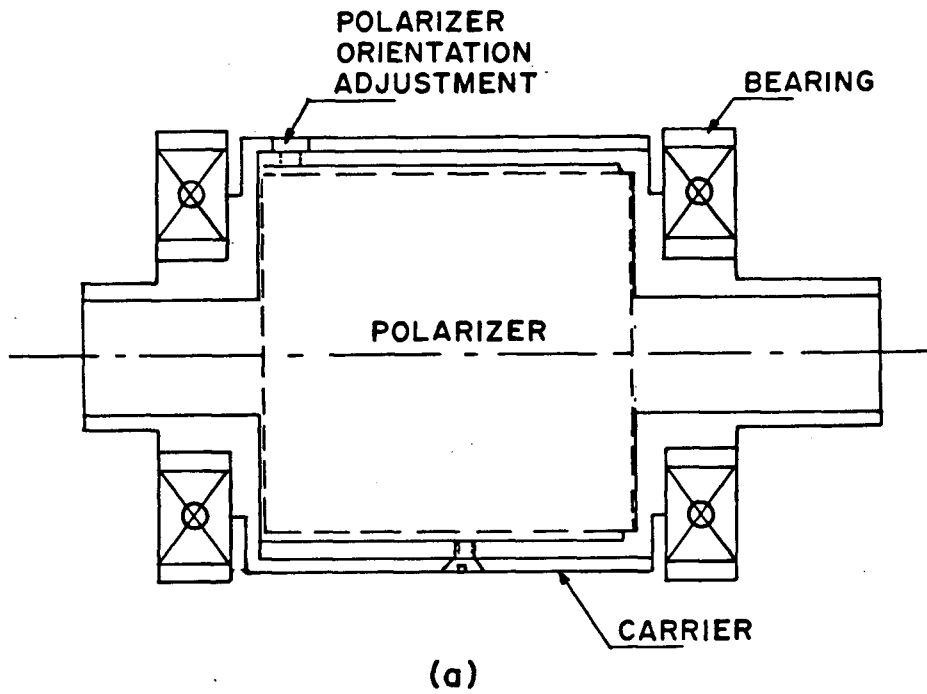
Figure 3.5. (a) Schematic of polarizer inside its housing. (b) alignment of polarizer with respect to rotation axis of carrier.

## POLARIZER ROTATION ASSEMBLY
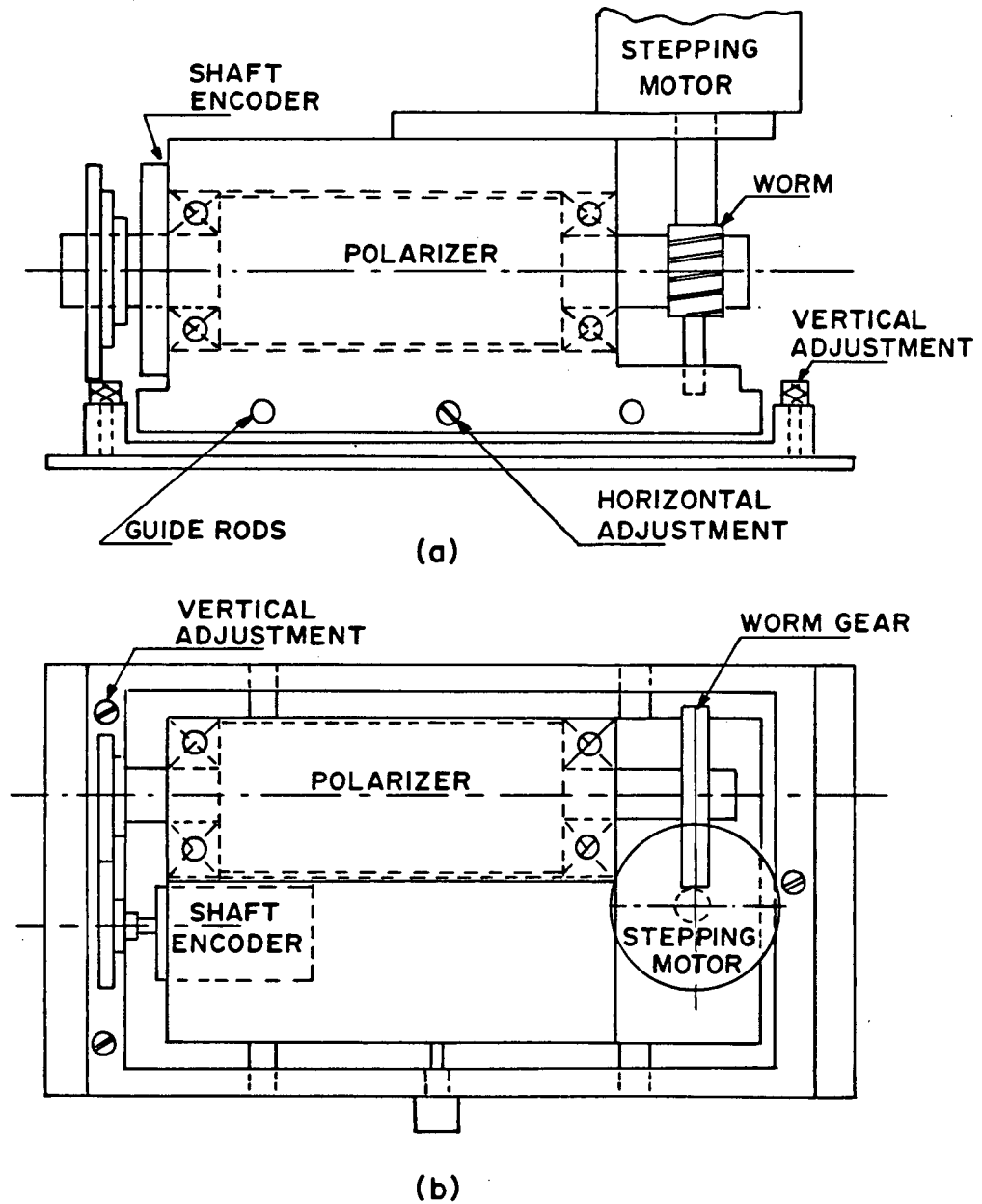
Figure 3.6. Schematic of polarizer assembly. (a) front view and (b) side view.

provide an absolute reading of the azimuth angle of the polarizer, and to check the rotation of the polarizer. In actual operation, the polarizer is rotated according to the shaft encoder reading so it is not critical if the stepping motor misses a step or if the worm gear arrangement has some periodic variation in it. The polarizer angle determined by the shaft encoder can be checked by passing light through the polarizer and measuring the azimuth angle of the output polarized light (in a straight-through position with no sample). Then rotating the polarizer to a new azimuth angle based upon the shaft encoder reading, the polarization of the light can be remeasured to see if the change in the azimuth angle measured corresponds to the expected angle. Slight variations $< 0.01°$ were observed, probably due to a shaft encoder-polarizer gear asymmetry. Even if no absolute shaft encoders are used, this method could be used to check that the stepping motor and worm gear combination are rotating the polarizer correctly.

It is important to align the polarizer carefully with respect to the incident light to minimize the possibility of systematic errors. The light beam entering the polarizer should be normal to the face of the polarizer and should be centered throughout the length of the polarizer. The base platforms of the polarizer and analyzer provide the degrees of freedom to properly align the polarizers. The platform allows the polarizer to be horizontally translated, while a pivot pin on the platform at one end of the polarizer allows the light to be centered horizontally. Micrometers on both ends of the platform provide the tilt and adjustment to align the polarizer vertically. Once the alignment has been made, the adjustment settings can be locked into place. It should be emphasized, however, a slight gradual movement of the polarizer or analyzer over a long period of time is not critical since the azimuth angles of both polarizers are normally calibrated prior to sample measurements.

*b. Alignment*

The normal to the polarizer face should be parallel to the rotation axis of the polarizer. This ensures that polarizer can be oriented such that the incident light is always normal to the face of the polarizer for any polarizer azimuth angle. This is accomplished by aligning the polarizer within the brass carrier as follows.

Once the polarizer has been inserted into carrier, two bearings are attached to either end of the carrier and the whole unit supported on a V-mount by the bearings. Next, light from a laser is directed onto the center of the polarizer face at an oblique angle and reflected toward a screen approximately 5 m away from the polarizer. If the polarizer face is not exactly perpendicular to the rotation axis, then the light reflected off the first face will trace out a circle on the screen as the polarizer is rotated (Fig. 3.5b). As the angle between the normal to the face and the rotation axis is decreased, the circle radius on the screen will decrease as well until, ideally, only a point is seen regardless of the polarizer azimuth orientation. This alignment is performed by making minute adjustments to the carrier set screws until the circle diameter is minimized. The degree of misalignment is determined by circle diameter and the polarizer-screen distance.

The reflection from the second face of the polarizer can also be seen, and it will always trace out a circle, even after aligning the front face of the polarizer. This does not indicate that the two polarizer faces are not parallel. This was demonstrated by turning the polarizer 180°, reflecting the laser light directly off the second face and observing the same degree of alignment. After the final alignment, a tiny drop of mild Loctite was placed on the set screws to ensure they would not loosen during rotation.

## 6. Sample Holder

The sample holder is mounted in the center of the chamber on top of a rotatable base. A computer controlled stepping motor underneath the chamber is attached to an anti-backlash worm/worm gear combination and, via a feedthrough, rotates the sample holder with a step resolution of $0.009°$. Care was taken during construction to ensure that the axis of rotation of the holder was perpendicular to the base of the chamber so that the beam reflected off the sample is parallel to the base, regardless of the angle of incidence.

During normal operation of the ellipsometer, the sample holder employed is a vacuum chuck with a polished stainless steel surface and the holder is oriented using tilt and horizontal translation adjustments. Different sample thicknesses can easily be accommodated by adjusting the horizontal stage. A tray at the bottom collects any solutions used to clean the sample prior to measurement. During initial alignment of the ellipsometer, a different holder is required as a laser beam has to be reflected off both sides of an alignment sample. This is discussed more fully in the next chapter.

## 7. Analyzer

The analyzer is a crystal quartz Rochon polarizer which is transparent from 185 nm into the infrared. The mounting of the analyzer inside the brass carrier and its alignment is similar to that of the polarizer. However, due to the optical activity in the crystal quartz, it is critical that the incident light enters the analyzer through the proper face. The correct orientation can be determined by first linearly polarizing a light beam (using another polarizer) and then passing the light through the analyzer. The undeviated output beam will be fully extinguished only in the proper orientation. After this orientation has been marked, the analyzer can be properly positioned in its

brass carrier.

## a. Mechanical Design

Similar to the polarizer carrier described previously, the analyzer carrier is supported by two bearings at either end in an aluminum housing. A delrin gear is mounted at one end of the carrier shaft and is connected in 1:1 gear ratio to an anti-backlash gear attached to the shaft of a hysteresis synchronous motor mounted horizontally above the carrier (Fig. 3.7). The rotor of an incremental shaft encoder was mounted on the shaft at the other end of the carrier, with the stator attached to the aluminum block. The shaft encoder generates 250 pulses per revolution along with an indexing pulse, and its operation is described in the data acquisition section. In the next design of the analyzer, a hollow-shaft motor to rotate the analyzer would be preferred because fewer moving parts would be required and there would be less vibration.

## b. Stablized Frequency Source

As will be discussed in the data acquisition section, it is critical to stabilize the frequency at which the analyzer is rotated.[54] This was accomplished by using a 5 MHz temperature-compensated crystal oscillator in a frequency synthesizer circuit to generate a 40-100 Hz signal. This signal is amplified to drive a four-pole hysteresis synchronous motor which rotates at exactly one-half the frequency at which it is driven. The frequency synthesizer, motor logic and amplifier were designed and built by the UBC Physics electronics department.

To test the short and long term frequency stability, the index pulse from the incremental shaft encoder was gated into a frequency counter and averaged over

# ANALYZER ROTATION ASSEMBLY
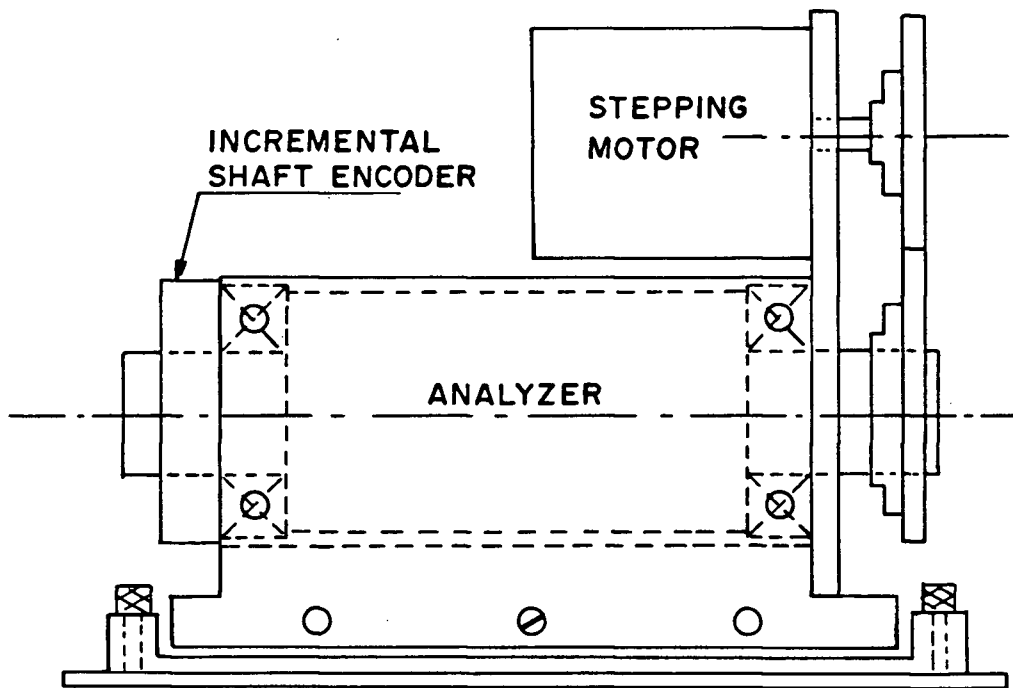


Figure 3.7. Schematic of the analyzer rotation assembly.

different time intervals. This measurement, encompassing the analyzer rotation, the shaft encoder and the index pulse triggering circuit, indicated that the frequency stability was better than 0.001% over a 10 minute period. There was no significant drift in the frequency as measured over a 24 hour period.

The analyzer rotation frequency was selected to minimize any possible harmonics of 60 Hz electrical or vibrational noise. If the analyzer is rotated at a frequency $f_d$, then any signal at this frequency will be sampled along with the desired light signal. Depending on the nature of the noise signal, this could affect the precision and accuracy of the measurement, even though ideally this noise can be subtracted out as will be seen in the data acquisition section. The criterion for maximum harmonic rejection of a frequency $f_r$ is that if $f_d/f_r = p/q > 1$, where (p,q) are least common multiple integers, then p should be as large as possible. Then all the harmonics except every (p−1)th harmonic of $f_r$ will be rejected after 'p' rotations. For $f_r = 60$ Hz, the driving frequency of 65.0 Hz was selected such that $f_d/f_r = 13/12$, so all the harmonics of 60 Hz, up to the 12th harmonic will be rejected. This was verified by sampling a 60 Hz signal and observing that only the 12th harmonic was picked out of the signal.

## 8. Photomultiplier Tube

The average light intensity reaching a detector can vary by three orders of magnitude over the typical measurement range, 1.5 − 6.0 eV. Therefore, a photomultiplier (PM) is the ideal choice due to its inherent low noise, wide dynamic gain and wide spectral response over the visible−near UV region. In a photomultiplier tube, the photons striking the photocathode emit photoelectrons which are focussed towards an amplification stage consisting of a series of dynodes. Each electron incident upon a

dynode generates 3 – 6 secondary electrons which are accelerated towards the next stage and so on until the electron current is finally collected by the anode.

The photomultiplier tube selected for the ellipsometer was a Hamamatsu R-376HA, 2.9 cm in diameter, with a wide spectral response from 160 nm to 850 nm. The head-on configuration of the PMT, where the light enters through the end of the tube, is relatively insensitive to the polarization state of the incident light; an important consideration in ellipsometry. The current amplification is provided by a 11 stage dynode structure, with an overall gain (ratio of anode current to cathode current) of $5 \times 10^5$ at a supply voltage of 1000V. The maximum average anode current is nominally 10 $\mu$A, but the ellipsometer was routinely operated at an average anode current of 15 $\mu$A with no difficulties.

The voltage-divider network of resistors to supply the proper voltage distribution to the cathode, dynodes and anode was designed to reduce the nonlinearity in the gain, G, in the PM. The PM was operated with the cathode at a high negative voltage and the anode at ground and the glass bulb was kept at the same potential as the cathode to reduce the probability of electrons striking the glass causing scintillation thereby generating a dark pulse. Since the detector nonlinearity may significantly affect the accuracy of the ellipsometry measurements, the cause of the PM nonlinearity is explained as follows.[62,64] First, assume that all the resistors, R, and hence the gain across each stage, are equal throughout the divider network. If $V_o$ is the voltage drop across an individual dynode, then the gain across one stage with no anode current is,

$$\delta = b V_o^g \qquad (3.1)$$

where typically $g \approx 0.8$. The total gain is then given by,

$$G_o = b^N V_o^N g^N \tag{3.2}$$

where N is the number of stages in the tube. In the presence of light an anode current, $i_a$, flows resulting in a *starvation* voltage drop across the last dynode–anode resistor, $\Delta V = i_a R$, leading to a slight loss in the collection efficiency of the anode. However, this voltage drop across the last resistor increases the total voltage across the amplification stage, i.e. the cathode–last dynode voltage. Therefore, the gain of the PM increases, and assuming $\Delta V$ is evenly redistributed across all the dynodes it can be shown to first order in the anode current that,

$$G = G_o(1 + g(i_a/i_t)) \tag{3.3}$$

where $i_t$ is the total current flowing through the PM.

Thus, (3.3) indicates the nonlinearity in the PM is proportional to the ratio of the anode current to (essentially) the divider network current and that this ratio should be kept as small as possible. Operating under constant anode current conditions, the nonlinearity increases as the PM supply voltage is decreased, since the total current decreases as well. Aspnes and Studna [62],[64] pointed out that any nonlinearity in the photomultiplier and detection circuits can be minimized by feeding back a voltage proportional to the anode current to decrease the supply voltage. This will be discussed more thoroughly in the next chapter.

The obvious method to reduce the PM nonlinearity is to maximize the current through the divider network by minimizing the resistor values. The minimum total resistance of the divider network is limited by the maximum output current rating of the power supply and the maximum power dissipation allowed for each resistor. With

29 kΩ resistors, the maximum total current drawn was 4 mA and the power dissipated was 0.5W per resistor. The resistors were mounted 5 cm away from the PM to prevent any dynodes from overheating when operating at high voltages and thus raise the dark current. As well, the resistors were heat sinked to metal plate using silver epoxy as an additional precaution. With a 15 $\mu$A average anode current, the ratio $i_a/i_t$ varied from 0.01 at 500V to 0.003 at 1450V. The actual nonlinearity of the current signal can be determined by a Fourier analysis of the light signal as will be described later.

The photomultiplier was mounted on a vibration isolation holder placed inside a light–tight box which can be attached to any port on the ellipsometer chamber. The vibration isolation holder consists of a mu–metal cylindrical shield (which surrounds the PM) supported by four springs to reduce the possibility of microphonic pickup noise in the PM. This arrangement also allows easy adjustment of the PMT orientation with respect to the incident light.

### a. Pre–amplifier

In the PM pre–amplifier, the anode current was lowpass filtered and converted into a voltage signal. The current–to–voltage converter consisted of a feedback resistor, $R_f$, across an op–amp, with an output voltage signal of $V_a = -R_f \, i_a$. The analog–to–digital (A/D) converter has a full scale range of 0 – 5V, so $R_f = 125 \, \Omega$ was selected to provide an average signal of 2 V for a constant anode current of 15 $\mu$A. This allows a safety margin to ensure the voltage peaks are not clipped when operating at slightly larger anode currents. The voltage signal was bandpass filtered at 3000 Hz and 165 Hz to reduce the noise bandwidth of the signal. Finally, the signal was buffered and sent to a sample–and–hold (S/H) circuit described later.

*b. Voltage Control*

The quantum efficiency of the PM and the light intensity incident upon the photocathode can vary substantially over the spectral range 1.5 – 6.0 eV. Consequently, the PM cathode current, and under constant gain the anode current, can vary by three orders of magnitude over the same range. Therefore to properly interface the voltage signal with the A/D converter the gain, and hence the supply voltage, of the PM has to be continuously adjusted to achieve a constant anode current.

The PM supply voltage was provided by a voltage programmable op-amp power supply capable of 0-2000V and 0-10 mA. In terms of precision, since the gain goes approximately as the 10th power of the supply voltage, the supply voltage stability should be a factor of ten better than that required for the gain stability. The power supply can be considered as an op-amp with a voltage gain of 200 so that a dynamic supply voltage range of 500 V to 1500 V requires an input or control voltage of 2.5 – 7.5 V. The PM voltage was controlled using a software algorithm to adjust the input voltage to the power supply amplifier which was controlled by the computer using a 12-bit D/A converter with a range of 0 to +5 V, summed to a reference 2.5 V. The algorithm was as follows. The average anode current was measured for two optical cycles of the analyzer, and the measured value was compared to the desired value. The control voltage, via the D/A, was then increased or decreased during the next optical cycle depending on whether the anode current was too low or high, respectively. After allowing an optical cycle for the anode current to resettle, the procedure was repeated until the desired average anode current was achieved. The typical time interval required to adjust the supply voltage for $i_a = 15 \ \mu A$ was $\simeq$ 200 ms.

Another approach is to use a feedback circuit to continuously adjust the supply

voltage for a constant anode current.[41,62,64] With this method, the reflected light is continuously monitored during a scan, except when measuring the stray light background.

## E. DATA ACQUISITION

### 1. Overview

The data acquisition system is concerned with the Fourier transform detection of the polarization state of the light reflected off the sample. The measurement cycle to obtain the Fourier coefficients of the modulated light signal at a given wavelength is as follows.

First, the shutter, normally in a closed state at the exit slit of the monochromator, was opened. The PM supply voltage was then adjusted from the previous setting to provide an average anode current of 15 $\mu$A. The voltage signal from the PM detector was then sampled uniformly 250 times per revolution of the analyzer and the values stored in memory. To increase the precision, signal averaging was performed for a certain number of optical cycles and then the shutter was closed. The stray light background and the voltage baseline were then measured and signal averaged as well. The discrete Fourier transforms of both the reflected light and background signals were calculated and the background coefficients were subtracted from the reflected light signal, which were then normalized to the dc coefficient. The normalized second harmonic Fourier coefficients were then saved along with the photon energy, and the measurement cycle continued with the next wavelength.

The following sections discuss the technical details of the data acquisition system and some of the possible systematic errors that may arise.

## 2. Signal Conditioning

The anode current is bandpass filtered at $f_1 = 3$ kHz and $f_0 = 165$ Hz to reduce the noise bandwidth of the signal. With the analyzer rotating at a frequency of 31.25 Hz, the sampling interval time is 128 $\mu$s. The $f_0$ time constant is $\simeq$ 1 ms, corresponding to a 8-point moving average of the sampled intensities. With the above low-pass filtering, the voltage signal phase shift is $\simeq$ 22° and the attenuation, $\eta \simeq 0.93$. Now, as mentioned in Chapter II, the attenuation and phase shift of the sinusoidal modulation of the signal corresponds to a change in the polarization state of the light beam. However, as long as the analyzer rotation frequency, $f_d$, is kept constant along with the low-pass breakpoint frequency, $f_0$, the attenuation and phase shift can be determined in the ellipsometer calibration procedure. If $f_d$ or $f_0$ were to drift substantially, however, between calibration and measurement, the accuracy could be significantly affected.[54] As well, if the stability in $f_d$ were relatively poor, this would have an adverse effect on the precision of the complex reflectance ratio. Therefore, a necessary requirement for accuracy and precision is a high stability for the analyzer rotation frequency, and the use of components with low temperature coefficients in the low-pass filtering circuits.

## 3. Sampling Algorithm

The data acquisition begins when a 68000 assembly language procedure is called, thereby enabling an A/D triggering circuit to start sampling the anode current at discrete azimuth angles of the analyzer. With the enable signal high and after receiving the indexing pulse from the analyzer, each pulse from the shaft encoder initiates a sequence of events. The PM voltage signal, connected to a 14-bit sample-and-hold (S/H) circuit, is continuously tracked until an encoder pulse is

received. Then the S/H amplifier enters into a "hold" mode and locks onto the instantaneous voltage of the signal. After a 12 $\mu$s interval to enable the S/H to stabilize, the 16-bit A/D conversion process starts, taking 16 $\mu$s to complete. Upon completion, an interrupt is sent to the computer which initiates an interrupt service routine to read in the 16-bit intensity value along with the pulse counter reading. The A/D value is then averaged with the A/D value measured during the previous cycle. A software count of the encoder pulses is also maintained for comparison with the hardware count. If the software and hardware counts do not match, a synchronization error is signalled and the data acquisition stops. If no errors occur the data acquisition continues, processing 250 pulses per revolution until the number of cycles specified for signal averaging has been completed. The measured voltage (intensity) readings are then stored in an array for further Fourier transform processing to obtain the normalized second harmonic coefficients. Note that the current limitation on the fastest analyzer frequency is the total sampling time of $\simeq$ 60 $\mu$sec.

## F. COMPUTER-ELECTRONICS INTERFACE

Automation of the spectroscopic ellipsometer involves the real-time software control of the monochromator, polarizer, analyzer, anode current, data acquisition, etc.,. This requires a computer/electronics interface which allows intercommunication and synchronization between the computer, a Sage IV (68000 microprocessor), and all the external devices. An interface between the computer bus and the "phys44" bus (connecting the external devices) was designed and built by the UBC Physics electronics department, as was most of the electronics used in the ellipsometer. This allowed any device to be accessed by the computer through io-memory mapped ports for sending and receiving data and commands.

In UCSD Pascal, semaphores are available which can force a process (i.e., a program) to wait until a signal has been given by an external device. Thus a computer, from a high level language, can request a device to perform a certain task and then wait (or continue with another process) until it has been completed. This has been implemented as follows. After the external device completes a task, it signals an interrupt controller chip which generates a computer interrupt. An interrupt service routine (ISR) responds to the interrupt by interrogating the controller for the device number which signalled the interrupt. This number is then used to signal a semaphore assigned to that device, allowing the computer to continue the process which was waiting on that device. This somewhat complicated procedure allows the computer programs and external devices to be synchronized. The required ISR's are automatically loaded into a safe location into memory via a startup program when the computer is booted-up.

## G. SOFTWARE

The control and analysis software on the Sage IV was written in UCSD Pascal except for a few time-critical applications written in 68000 assembly language. Probably the most important feature of this language is the ability to write and compile the code into separate units, as in Modula-2. Thus, any code which is self-contained and complete can be designed as a unit which can then be accessed by any other unit or program. Furthermore, the ability to perform type and parameter checking is still retained.

The menu-driven ellipsometer program allows the operator to:

1.      Automatically calibrate the ellipsometer.

2.      Measure automatically the complex reflectance ratio of a sample as a

function of photon energy, wavelength, polarizer azimuth angle or time.

3.   Control the monochromator, polarizer, angle of incidence, analyzer, and anode current individually.

4.   Determine the pseudodielectric function of sample.

5.   Plot a wide variety and combination of data files.

6.   Run diagnostic routines to check the ellipsometer.

7.   Transfer data and files between a mainframe computer and the microcomputer.

The current calibrated positions for the wavelength, polarizer azimuth angle, angle of incidence are all stored in a file along with the calibration parameters for the ellipsometer. This file is updated every time any of the parameters is changed, allowing the control program to know the state of ellipsometer at all times.

As an example, to perform a scan to measure the complex reflectance ratio as a function of photon energy, the operator specifies the start and end of the scan, if different from the previous scan, along with the number of photon energies to examine or the photon energy interval between measurements. Once the scan parameters have been entered, the scan begins at the push of a button and is fully automated as previously described. Typically, for 80 points in the spectral range 1.5 – 5.5 eV, a scan takes 20 minutes to complete. During the course of the scan, the measured $(\alpha,\beta)$ parameters are displayed along with the current photon energy, the average anode current and the current PM supply voltage.

### 1. Data Files

Once a scan measurement has been completed, the data are stored under a user-specified filename. The first block of the file (512 bytes) contains the system parameter information at the time of the measurement. Typically, the type of scan, the current calibrated system parameters, time and date of scan along with other relevant information are recorded in this block. This information is retrieved along with the scan variables and the $(\alpha,\beta)$ data in order to calculate the complex reflectance ratio or the pseudodielectric function. The advantage of storing the data and system parameters together is that the file remains self-contained and the relevant parameters for the data analysis are accessed automatically.

### H. DC PLANAR MAGNETRON SPUTTERING

Sputtering is a physical vapour deposition technique whereby a *sputtering target* is bombarded by ions resulting in the ejection of target atoms, some of which then condense upon the substrate to be coated. Practically any material, insulating or conducting, can be sputtered, making this a very versatile technique. Excellent reviews of sputter deposition can be found in many texts, most notably Chapman,[67] Vossen and Kern,[68] Bunshah *et al.*[69] and in several recent review articles by Thornton.[70 - 72]

A brief description of the dc planar magnetron sputtering system used to deposit palladium films is given here. The schematic of the dc planar magnetron sputtering system is shown in Fig. 3.8. Inside the high vacuum, diffusion-pumped chamber is a target composed of the coating material and the substrate separated, by a moveable shutter. The target was a 15 cm diameter palladium disk (99.98% purity) with the substrate holder at a typical distance of 8 −12 cm from the target. After pumping down the system to a low base pressure, typically $1\times10^{-6}$ Torr, high purity
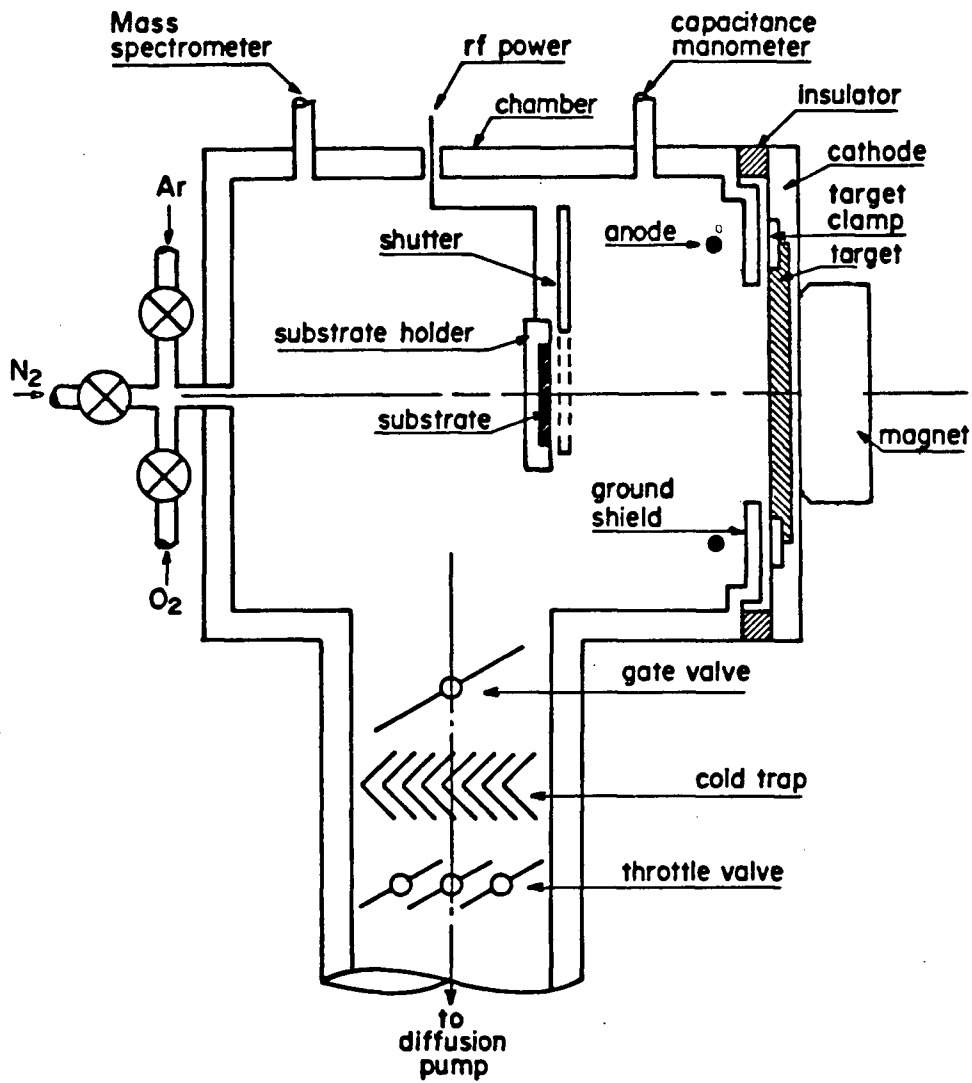
Figure 3.8. Schematic of dc planar magnetron sputtering system.

argon gas is introduced and the diffusion pump throttled to achieve an argon partial pressure in the range 5 – 30 mTorr. The partial pressure of the gases inside the chamber is monitored by a capacitance manometer.

To initiate the sputtering process, a large negative voltage is applied to the target (cathode) while the chamber walls form a grounded anode and the substrate holder is either grounded or electrically floating. A glow discharge, consisting of a neutral plasma then is established between the target and the substrate. A positive space–charge sheath is set up between the target and the plasma whose thickness depends upon the target geometry. Argon ions at the edge of the sheath in the plasma are then accelerated across the dark space and bombard the negative target. Momentum transfer from the argon atoms to the target surface results in some target atoms being ejected or sputtered away from the target. As well, fast secondary electrons are ejected by the argon ion bombardment to help sustain the glow discharge. The trajectory of the sputtered atoms from the target to the substrate may either be line–of–sight (essentially collisionless) or a random walk (diffusion process) depending on whether the argon partial pressure is low or high, respectively. Permanent magnets underneath the planar target create a magnetic field which traps the secondary electrons emitted from the target. These electrons significantly enhance the argon ionization above the target surface leading to a higher rate of bombardment, and hence, a higher rate of deposition. Furthermore, the temperature of the substrate is reduced as the fast secondary electrons are no longer able to bombard the substrate.

In this study, the voltage applied to the target is dc, but rf may be applied as well. Other deposition parameters such as the argon partial pressure, substrate temperature, substrate biasing, target–to–substrate distance, etc., may be varied as well

to determine the optimum preparation conditions. Further details on the sputtering system relevant to the characterization of the deposited thin films will be presented in Chapter VI.

## 1. Substrate Cleaning Procedure

Prior to deposition, the Corning 7059 glass substrates were cleaned using the following procedure. First the substrates were blown clean with high pressure $N_2$ to remove any dust or contaminants. Next, the substrates were placed on lens tissue paper, soaked with methanol, and lightly polished to remove any chemical residue on the substrates. After this they were placed in a trichloroethylene bath and mildly agitated for about a minute. Then the substrates were removed from the bath, rinsed with methanol to remove any solvents and then quenched in a methanol bath for another 30 seconds. Upon removal from this bath, the substrates were blown dry with $N_2$, and the surfaces of the substrates were inspected. If any residue was noticeable on the surface, the above procedure was repeated until the surface was free of blemishes.

With this cleaning technique, the surface of the deposited thin films were free of imperfections and no pinholes developed in the films. If the chemo-mechanical polishing step with methanol were bypassed, pinholes generally developed in the films after a couple of hours upon removal from the sputtering chamber.

# CHAPTER IV. ALIGNMENT AND CALIBRATION

## A. OPTICAL ALIGNMENT

### 1. Introduction

The primary objective of the optical alignment is to provide a light source beam that is properly centered with respect to all the optical components in the system[54] and has a well defined angle of incidence ($\phi$) with respect to the sample. As well, inserting a new sample and aligning it must be quick and precise.

To this end, all the optical elements in the system have been aligned around a laser, which has a secondary function of aligning a sample prior to measurement.

### 2. Initial Alignment

For the initial alignment of the ellipsometer as a whole, a He–Ne laser was mounted on an optical bench and adjusted until its beam was approximately parallel to the surface of the bench. The chamber, also on the bench, was then adjusted until the beam entering through its alignment laser port was parallel to its inside base.

The next step was to ensure that the alignment laser beam was perpendicular to, and intersected, the axis of rotation of the sample holder.[1] This is critical as the light beam and the sample is aligned with respect to this laser, and hence this determines the angle of incidence, $\phi$.

A steel gauge block, in which both sides are certified to be flat and parallel to each other within a certain tolerance, was mounted on a special holder. With this holder, the laser beam could be reflected off one side of the gauge block and then

the other after rotating the holder by 180°. By noting that a rotation of the sample holder by 0.01° can be visually discerned in this system, this sets a maximum tolerance limit of 18 arc-seconds on the non-parallelism of the gauge sides.

The alignment laser was then horizontally adjusted until the laser beam intersected the axis of rotation of the sample holder. Next the sample holder was rotated until the beam spot reflected back towards the laser was horizontally (but not necessarily vertically) aligned with the laser exit aperture. This vertical misalignment (distance between reflected beam spot and the exit aperture) was first reduced by one half by vertically tilting the laser and then eliminated altogether by adjusting the sample holder tilt. At this point the incident and reflected beams are parallel to each other.

Then the holder was rotated by exactly 180 degrees. If the laser beam had been perpendicular to the axis of rotation, the reflected beam would again be parallel to the incident beam and there would be no vertical misalignment after the rotation. If a vertical misalignment still existed, then the above procedure would be repeated, i.e., eliminating the misalignment by adjusting both the laser and the sample holder and then rotating by 180°. This iterative procedure actually converges quite quickly, usually within four or five rotations. If this does not occur, then the sides of the steel gauge block may not be parallel within the tolerance required. A horizontal misalignment after rotation might indicate that the sample holder was not rotated by exactly 180 degrees (the stepping motor may by missing some steps), or else the "vertical" adjustments may have had a slight horizontal movement.

At this stage, the laser beam reflected off the gauge block (independent of the angle of incidence) should be at the same height all along the base of the chamber. While not critical, this does give an indication how flat the base is and if the normal

to the base is parallel to the axis of rotation of the sample holder.

In order to properly define the angle of incidence in the next stage, it is crucial that the alignment sample be positioned directly over the axis of rotation of the holder. This can be done by rotating the sample by 90° with respect to the laser and translating the holder horizontally until the beam grazes the sample surface. Then the holder can be rotated by 180° and the beam should still be grazing the surface. As a further check, one can reflect the beam through one of the ports and determine trigonometrically whether the angle measured is the same as that selected.

## 3. Transfer Optics

The next step was to position the arc lamp with respect to the monochromator in order to focus the image of the arc onto the entrance slit. The arc lamp was positioned to the side of the monochromator as close as possible to minimize aberrations in its image, and the mirror M1 (see Fig. 3.1) was placed approximately 20 cm away from the entrance slit. A rough alignment was performed to focus the arc image onto the slit. As well a variable aperture was set up just in front of the arc lamp to adjust size of the light beam reaching the mirror M1 and as a further alignment check.

Next the monochromator and arc lamp positions were adjusted until the path length from the exit slit to the sample holder was sufficient for a magnification of two of the slit image onto the sample holder. Owing to the geometry of the chamber, a plane mirror M3 was required to direct the beam towards the sample holder. Another variable aperture was set up just in front of the entrance port of the chamber in order to limit the beam size through the polarizer, if necessary, and to reduce any stray light.

A shutter was placed inside the monochromator just after the exit slit and two horizontally oriented slits were adjusted to provide a sharply defined image at the sample. The small aperture of the shutter required it to be placed at the waist of the arc beam and so it was mounted by the exit slit of the monochromator.

At this point, the alignment gauge block was oriented so that the alignment laser beam was reflected back upon itself. Then the sample holder was rotated by exactly 22.50° so that the beam reflected off the sample went through the entrance port of the chamber. The monochromator was horizontally leveled until the entrance and exit slits were at approximately the same height as the laser. Next the plane mirror M3 and concave mirror M2 between the chamber and the exit slit were centered with respect to the laser beam, which was directed towards the center of the exit slit. The mirrors M2 and M3 were then adjusted until the laser beam passed through the entrance slit of the monochromator (at this point the slit widths should be the same as the laser beam diameter). Mirror M1 was then further adjusted until the laser beam passed through the center of the arc spacing in the lamp.

At this stage, the optics had been coarsely aligned. The next step was to turn the arc lamp on and center its beam about the laser beam (before the entrance slit), by adjusting the arc lamp along with mirror M1. With the slits wide open now, mirrors M2 and M3 were re-positioned more accurately such that the slit image on the sample was magnified by a factor of two. With this magnification, the image was kept fairly small, while the arc beam was not too divergent after reflection from the sample. Note that it is necessary to minimize the convergence and divergence of the beam in order to keep the beam diameter below the clear aperture diameter of the polarizer and analyzer where they are positioned along the beam path, while not limiting the optical speed of the ellipsometer.

The mirrors, along with the arc lamp, now had to be minutely adjusted until the arc beam was centered about the laser beam along the full path from the arc lamp to the alignment laser. This should not take more than two days.

Next, variable and fixed apertures were inserted into the beam path at certain critical points. First a fixed aperture was placed on the chamber base just before the alignment laser port, and is centered with respect to the incident laser beam. This was used for sample alignment later on, as well as for later system alignment checking. Next a small variable aperture was positioned just before the sample holder, and was also centered with respect to the laser beam. It served two purposes: one, as an alignment check and two, to block the deviated (and unwanted) beam from the polarizer. Of course, the size of the apertures during measurement were selected to reduce possible stray light or multiple reflections and to limit the size of the beam reaching the sample. These various considerations and others such as light intensity and possible noise (due to vibrations causing the apertures to chop the light) had to be balanced in choosing a final aperture size. Several other apertures along the beam path (as well as the monochromator slits) helped to check the alignment of the ellipsometer at later dates.

### 4. Angle of Incidence

The exit port was positioned such that the arc lamp beam reflected off a sample at $\phi \simeq 67.5°$ passed through approximately the center of the port. Thus an angle of incidence of exactly 67.50° was selected for this ellipsometer. As the arc beam was centered with respect to the laser beam, the angle of incidence was determined also with respect to the laser. Of course, since the beam from the arc lamp was slightly convergent, then the angle of incidence of 67.50° was actually an

average over the whole beam width.

While sample alignment will be discussed later on, the alignment technique is based on the fact that if the sample is rotated to a position such that laser beam is reflected back upon itself, then the sample is at $\phi = 45.00°$ with respect to the arc beam. Then it is a simple matter of rotating the sample holder a known number of steps until $\phi$ equals $67.50°$.

## 5. Polarizer Alignment

The first step was to position the polarizer such that the laser beam was centered with respect to the polarizer along its entire length. Two plugs, with 1 mm holes in the center, inserted into both ends of the polarizer mount simplified this part of the alignment. By either vertically or horizontally translating the polarizer, or tilting one end with respect to the laser beam, the light was made to pass through both 1mm holes. Next the plugs were removed and the laser beam reflection off the polarizer face was used to monitor further alignment. Minute adjustments to the polarizer were then made until the reflected beam was parallel to the incident beam. It remained parallel even as the polarizer was rotated if the polarizer had been aligned properly within its carrier as outlined earlier.

Note that the light beam diameter should be smaller than the clear aperture of the polarizer. If not, then some of the light may scatter off the sides of the polarizer or the inside of the carrier, thereby inadvertently decreasing the effective extinction ratio of the polarizer. Furthermore, since this polarizer is a beam-splitting device, the aperture following the polarizer must be positioned a distance away such that it blocks the deviated beam after the deviated and undeviated beam have been well separated. Since the deviation angle changes with wavelength, one should be careful that this

positioning is done at the minimum deviation wavelength.

### 6. Analyzer Alignment

The analyzer alignment proceeds basically along the same lines as that of the polarizer. If the ellipsometer is to be operated in the reflection mode, then the sample holder should be rotated by 45.00° with respect to the incident laser beam such that the reflected beam follows the same path as that of the arc lamp beam for the nominal angle of incidence of 67.50°.

In the straight-through mode, used for initial testing purposes, the sample holder would be rotated by 67.50° with respect to the laser beam.

A variable aperture is set up between the sample holder and the analyzer in order to reduce any stray light scattered off the target. As well, this aperture when stopped to its minimum, assists in the re-positioning of the sample holder whenever the sample thickness has changed.

A further blocking aperture is set up behind the analyzer to stop its deviated beam from reaching the photomultiplier.

### 7. Photomultiplier Alignment

The alignment of the PM can be critical to the proper alignment of the ellipsometer, as the reflection off the front face of the PM may be directed back towards the analyzer and then reflected back to the PM. Since the light transmission through the analyzer should be symmetric with regards to a 180° analyzer rotation, this symmetry might be lost because of improper PM or analyzer alignment. This symmetry is an important check on the optical alignment and will be discussed more fully below.

## B. FINAL OPTICAL ALIGNMENT

After turning on the arc lamp and opening up the monochromator slits, the light beam should be centered about all the apertures in the system. If not, there is still some misalignment which needs to be corrected.

Next, reducing the slit width and closing the shutter, the chamber lid should be placed onto of the chamber, and the cap on the alignment port should be screwed on. At this point, the ellipsometer should be light-tight. This can be checked by turning on the PM and slowly increasing the gain with the shutter closed. If the chamber is light-tight, then there should be no noticeable increase in the dark-current at the highest gain when the room lights are turned off and on. As it is presently set up, there was a slight increase in the dark current on the order of 1%, which in any case is accounted for during the data measurement.

### 1. Analyzer Symmetry-Peak Difference

The next step is to record the light transmission through the analyzer measured at 250 points per mechanical revolution. Due to the symmetry of the analyzer there are two optical revolutions per mechanical revolution. Thus a peak in the light signal during the first optical revolution should have the same intensity as the peak in the second optical revolution. The percentage peak difference is defined for alignment purposes as the difference in the peak intensities divided by the peak average.

A peak difference $\leq$ 0.10% means that the alignment is symmetric with respect to the analyzer. A peak difference much greater than 0.10% indicates that the alignment should be examined more carefully.

A large peak difference might be caused by one or more of the following.

1.    The light beam is not passing directly through the center of the

analyzer or else it is at an angle with respect to the normal of the analyzer's axis of rotation.

2.     The PM is not oriented properly and possibly should be repositioned.

3.·     The normal to the faces of the analyzer may not be parallel to the axis of rotation of the analyzer. This can be corrected by adjusting the analyzer within its carrier.

Furthermore, a small peak difference at one wavelength does not imply that the peak difference will be small at all other wavelengths. So the next check is to ensure that it is within a certain tolerance, i.e., under 0.30% for all wavelengths. During the normal course of measuring the optical properties of samples, the peak difference is monitored continuously and if some deviations are observed it may be an indication that some optical element is not properly aligned.

## 2. Polarizer Symmetry

The rotation of the polarizer can also be used as a check in system alignment. First, the symmetry of the analyzer as determined by the peak difference should be invariant under any polarizer rotation. As well, using the symmetry of the polarizer, any experimentally determined results such as the measured dielectric function should be the same before and after a rotation of $180°$.

Another important test is whether or not the polarizer can be rotated to a certain angle such that the light transmission through the (stationary) analyzer can be reduced to the dark current of PM, assuming the incident light is linearly polarized. If not, then the polarizer may not be oriented correctly or the analyzer, if positioned backwards, may be pseudodepolarizing the input light (due to its optical activity), although this is fairly easy to test. Note that this test should be performed with the

analyzer kept stationary and not the polarizer, since the lowpass filtering of the anode current smooths out the intensity modulation thereby giving the false impression that the extinction ratio is 100 instead of $1 \times 10^6$!

## C. SAMPLE ALIGNMENT

Once the ellipsometer optics have all been aligned, then the only alignment to be performed is that of a newly inserted sample. As stated before, this alignment should be precise, and therefore reproducible, and accurate with the condition that the procedure should not be too tedious as it will be done on a regular basis.

With the alignment laser, the sample alignment is fairly straightforward. After inserting the sample into the holder it should be rotated to the nominal alignment position, where the laser beam is reflected back to a fixed aperture. By rotating the sample holder one step at time (corresponding to $0.01°$), in the direction the holder usually rotates (to avoid backlash), the horizontal misalignment between the beam spot and the aperture can be eliminated. It is fairly easy to align the sample within one step or $0.01°$. By adjusting the vertical tilt of the sample holder, the vertical misalignment can be eliminated as well.

At this point, the angle of incidence is exactly $45.00°$ with respect to the arc lamp beam, hence a rotation of the sample holder by $22.50°$ will orient the sample at the desired $\phi = 67.50°$.

If the sample thickness had changed from the previous run, then the sample holder must be horizontally translated in order for the reflected beam to pass through the center of the analyzer. One way is to rotate the sample holder until the alignment laser beam is parallel to the sample surface, and then translate the sample holder horizontally until the beam grazes the sample's surface. Alternatively, with

$\phi = 67.50^\circ$, the light beam reflected off the sample should be centered about the aperture in front of the analyzer.

Two important criteria indicating proper sample alignment are :

i) the peak difference should remain small and

ii) system invariants such as the polarizer and and analyzer reference azimuth angles should remain the same if they have not been previously adjusted and if the sample is isotropic.

Furthermore, if the sample is removed, and then re−inserted and re−aligned, the relevant optical data (tan$\psi$,cos$\Delta$) measured before and after should agree within an allowable tolerance (which may vary according to the experimenter's state of mind).

## D. CALIBRATION

### 1. Introduction

After the ellipsometer has been optically aligned it is now necessary to calibrate the reference azimuths of the polarizer and analyzer corresponding to the transmission axes of these optical elements lying in the plane of incidence. [29],[53] That is, the azimuth angles of the polarizer and analyzer as measured by their respective shaft encoders must be calibrated with respect to the plane of incidence. However, in order to reduce the noise bandwidth of the system, the anode current from the PM passes through a low−pass filter which attenuates and phase shifts the voltage signal with respect to the light intensity signal. [54] The low−pass filter affects the apparent polarization state of the reflected light transmitted through the analyzer, and must be corrected for. A further complication is due to the optical activity of the analyzer (discussed previously), which

needs also to be taken into account during calibration and at the data reduction stage.

## 2. Calibration Theory

The calibration procedure for the RAE was developed by Aspnes,[29,54] and the notation in this section is therefore similar to his.

The basic principle involved is as follows: if linearly polarized light is incident onto an isotropic, absorbing surface it will remain linearly polarized after reflection if, and only if, the initial state of polarization was parallel or perpendicular to the plane of incidence (the normal modes of the system). Note that this is not true for a dielectric substrate, where incident linearly polarized light of an arbitrary azimuth angle is always reflected off linearly polarized, and so a dielectric surface cannot be used with this calibration procedure.

As previously discussed, the ac modulation amplitude in the light intensity through the analyzer is a maximum if the light is linearly polarized. This suggests that by rotating the polarizer azimuth through the plane of incidence and observing when the modulation amplitude is maximized, one can determine the reference polarizer azimuth directly.

For the analyzer, as it can only be rotated continuously, its reference azimuth angle is established by first setting the the polarizer in its reference azimuth position and then noting the instantaneous angle at which the light transmission reaches its maximum through the analyzer. This angle then corresponds to the analyzer's reference azimuth lying in the plane of incidence.

In practice, the calibration is slightly different from that described above due to the broad maximum in the ac amplitude modulation about the plane of incidence. The calibration procedure is now made more quantitative and for simplicity the effects of

the low pass filter and analyzer optical activity are neglected for the moment.

If the light incident upon the analyzer is $I_0$, then the transmitted intensity through the analyzer is,

$$I(A) = I_0 \{ \ 1 \ + \ a\cos 2A \ + \ \beta \sin 2A \ \}$$

where $a, \beta$ are the normalized second Fourier coefficients and A is the analzyer azimuth angle measured with respect to an indexing pulse (which occurs once per mechanical revolution). The reference analyzer azimuth $A_S$ is then defined as the angle between the indexing pulse and the plane of incidence.

As the incident light polarization varies between being circularly and linearly polarized then $\zeta^2 = [a^2 + \beta^2]$ will increase from $\zeta = 0$ to 1. The residual $R(P) = 1 - a^2 - \beta^2$, where P is the polarizer azimuth angle (measured with an absolute shaft encoder), has a minimum at $P_S$, the reference azimuth angle, and is quadratic about $P = P_S$. Thus by measuring $(a_i, \beta_i)$ versus $P_i$ for $i = 1, 2, ... N$ about $P \approx P_S$ and fitting a quadratic function $R(P) = c_0 + c_1 P + c_2 P^2$ to the data, $P_S$ can be determined.[54]

The analyzer reference angle $A_S$ corresponds to the maximum in the intensity $I(A)|_{P=P_S}$. Differentiating $I(A)$ and setting it to zero gives $A_S = (1/2)\arctan(\beta / a) +$ $(\pi/2)u(-a)\text{sgn}\beta$, where $u(x) = 1$ for $x \geq 0$, $u(x) = 0$ for $x < 0$, and $\text{sgn}(x)$ is the sign function (note that the second term will be implicitly assumed from now on). In the actual calibration routine [54] $Q(P_i) = (1/2)\arctan(\beta_i / a_i)$ is computed along with $R(P_i)$ and fitted to a quadratic as well, with the result that $Q(P = P_S) = A_S$.

## 3. Signal Conditioning

As previously mentioned, the effect of passing the signal voltage through a low-pass filter is to attenuate and phase shift the signal with respect to the light intensity signal. Therefore if the *actual* measured coefficients are $(a_{2i}, b_{2i})$, and if $1/\eta$ and $A_F$ are the relative attenuation and phase shift of the signal respectively, then[54]

$$\alpha = \eta \ \{ \ a_2 \cos 2A_F \ + \ b_2 \sin 2A_F \ \} \tag{4.1a}$$

$$\beta = \eta \ \{ \ -a_2 \sin 2A_F \ + \ b_2 \cos 2A_F \ \} \tag{4.1b}$$

In terms of calibration, the effect of the attenuation is that now $R(P_S) = 1 - \eta^{-2}$, so in the process of fitting $R(P_S)$, $\eta$ can be determined along with $P_S$ and $A_S$.

The phase shift itself is unimportant (as long as it doesn't change between calibration and experiment!) since the analyzer azimuth angle with respect to the plane of incidence $(A-A_S) = (\ [A-A_F]-[A_S-A_F] \ )$.

## 4. Optical Activity Correction

The theory is explained quite thoroughly by Aspnes,[53] so only the general outline and results will be presented here.

The effect of the optical activity in the analyzer is to change the normal modes of the analyzer from being linear to slightly elliptically polarized. If not corrected for during calibration, the measured reference azimuth angles for the polarizer and analyzer can be altered quite significantly, and change depending upon the calibration wavelength.

The optical activity coefficient for right-handed crystal quartz, for the time convention $\exp(-i\omega t)$, is $\gamma_A = 0.0010(\hbar\omega/eV)$, where $\hbar\omega$ is the photon energy.[53] Now elliptically polarized light incident upon the analyzer will have its ellipticity slightly

changed due to the optical activity. In terms of the calibration, the minimum in the measured residual has now been shifted, so that the measured minimum $P_1$ is different from $P_S$.

The relationship between the measured $(P_1, A_1)$ and the true $(P_S, A_S)$ reference azimuths *parallel* to the plane of incidence is given by

$$P_S = P_1 - \gamma_A \tan\psi / \sin\Delta \qquad (4.2a)$$

$$A_S = A_1 - \gamma_A \cos\Delta / \sin\Delta \qquad (4.2b)$$

where $\rho = \tan\psi \exp\{i\Delta\}$ is the complex reflectance ratio of the sample being calibrated.

## 5. Summary

If the calibration is being performed just after an initial system alignment, then $P_S$ has to be determined approximately before using the above procedure. Perhaps the easiest way is to use a flat vitreous silica ($\geq 3$mm) substrate and place it on the sample holder at its Brewster angle. Then the polarizer is rotated until the light reflected off the surface has been extinguished. At this point the polarizer reference azimuth is approximately in the plane of incidence.

The calibration routine can therefore be summarized :

1.    Insert new sample and optically align it.

2.    Measure coefficients $\alpha, \beta$ vs polarizer angle for a series of points $i = 1, 2, .. N$ centered approximately about $P = P_S$, and at a wavelength where the surface is metallic-like (this can be checked setting $P \simeq 30°$ and observing if $\alpha \simeq \beta \simeq 0$ ).

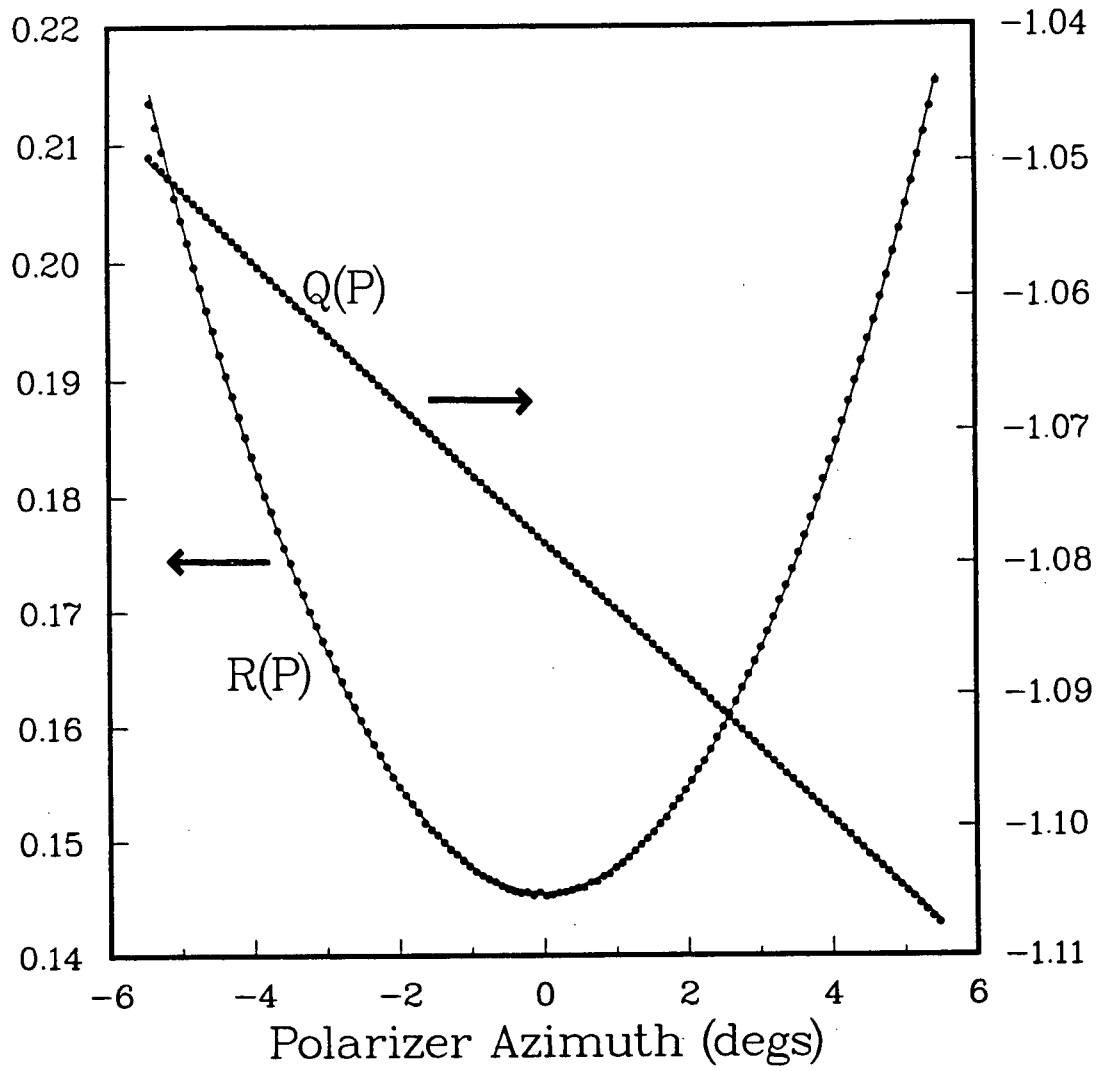3.    Next compute $R(P_i)$, $Q(P_i)$ and fit these functions to quadratics to obtain $P_1, A_1$ and $\eta$.

Figure 4.1. Typical calibration scan of modulation vs polarizer azimuth angle.

4. Move the polarizer azimuth angle to $P \simeq P_1 + 30°$ and measure $(\tan\psi, \cos\Delta)$.

5. Compute $P_S, A_S$ and update the system calibration.

6. If $P_S$ or $A_S$ have changed more than $0.02°$ either the sample is anisotropic, or else the system may have gone out of alignment.

A typical calibration scan is shown in Fig. 4.1, and in Table 4.1, the changes in the calibrated reference azimuths for the polarizer and analyzer are shown vs. wavelength if the optical activity correction is ignored.

## E. PRECISION

As the terms precision and accuracy are sometimes confused, their definitions are as follows. Precision refers to how repeatable a measurement is with all controllable parameters kept constant. Accuracy on the other hand refers to how close the measured values are to the true values. Since precision is a prerequisite for accuracy, it will be discussed first.

### 1. Optimizing Precision

Photometric ellipsometers such as the RAE have a high precision capability when operated under shot-noise limited conditions.[29,43,74] This capability allows third derivative spectra to be computed to enhance any weak structure in the spectra and investigate critical points in the band structure.[73] However, the ultimate precision depends upon operating conditions such as the angle of incidence and the incident polarization azimuth angle. In this section, the optimal conditions for precision will be determined, as well as the limitations on the precision depending on the surfaces being measured.

Table 4.1. Calibration measurements of the polarizer and analyzer reference azimuths as a function of wavelength. $(P_1, A_1)$ and $(P_S, A_S)$ are the azimuths determined before and after the correction for optical activity, respectively.

| $\lambda$ (nm) | $P_1$ | $A_1$ | $P_S$ | $A_S$ |
|---|---|---|---|---|
| 300 | 65.95° C | −62.20° C | 65.62° C | −62.22° C |
| 400 | 65.87° C | −62.25° C | 65.62° C | −62.22° C |
| 500 | 65.84° C | −62.28° C | 65.64° C | −62.23° C |
| 600 | 65.82° C | −62.30° C | 65.64° C | −62.23° C |

Now $\tan\psi$ and $\cos\Delta$ can be expressed in terms of the normalized Fourier coefficients $a$ and $\beta$ as follows,[74]

$$\tan\psi \cdot |\cot(P)| = [(1+a)/(1-a)]^{1/2}, \tag{4.3a}$$

$$\cos\Delta = \beta (1-a^2)^{-1/2} \tag{4.3b}$$

Using (2.12) and (2.22), it can be shown that the uncertainty in $\rho$ is minimized for $a = 0$ with,

$$|\tan(P_{opt})| = \tan\psi, \tag{4.4a}$$

$$\cos\Delta = \beta, \tag{4.4b}$$

and

$$|\delta\rho|_{rms} = [(2-\beta^2)/(1-\beta^2)]^{1/2} \tan\psi \cdot \delta a_{rms} \tag{4.4c}$$

Therefore, the optimum polarizer angle is given by (4.4a) and since $|\delta\rho|_{rms}$ is proportional to $\tan\psi$, the optimum angle of incidence corresponds to the pseudo-Brewster angle, $\phi_B$, where $\tan\psi$ is at a minimum. From (4.4c) it is clear that the uncertainty in $\rho$ can become very large for $|\beta| \approx 1$ corresponding to linearly polarized light. Hence, for a dielectric surface, or a thin film multilayer structure,

where $\Delta \simeq 0$ or $-\pi$, the measured optical properties may have relatively large uncertainties. In particular, $\epsilon_2$ is not determined very accurately[33,74] for any substrate when $\epsilon_2 \simeq 0$.

For an ambient-substrate system (2.13) the uncertainty in $\epsilon_s$ with respect to $\rho$ is given by,

$$|\delta \epsilon_s|_{rms} = |\delta \rho|_{rms} \, f(\phi) / (1-\rho^2) \qquad (4.5)$$

where $f(\phi)$ is a function that depends on the angle of incidence. Therefore $|\delta \epsilon_s|_{rms}$ is minimized when $\rho$ is purely imaginary or $\Delta = -\pi/2$, which corresponds to the principal angle for the substrate. The uncertainty in $\epsilon_s$ with respect to the angle of incidence, $\phi$, is minimized in the range $35° \leq \phi \leq 70°$ and becomes large at normal or grazing angles of incidence. Since the difference between the pseudo-Brewster angle and the principal angle is small, the optimum conditions for minimizing $|\delta \epsilon_s|_{rms}$ are close to that for $\rho$.

Aspnes[29,74] has shown that to achieve shot-noise limited conditions, the signal current should be greater than twice the dark current. Then under the optimal conditions ( $|\tan(P)| = \tan\psi$ and $\Delta = -\pi/2$ ),

$$2\delta\psi = \delta\Delta = \delta\alpha = \delta\beta \simeq 2/\sqrt{N} \qquad (4.6)$$

where N is the number of contributing photoelectrons in a given time interval. The precision can be increased therefore by increasing the light flux or signal averaging over a longer time interval.

## 2. Measured Precision

The above analysis assumes, of course, that all other major sources of noise have been eliminated. This is achieved, as outlined in Chapter II, by stabilizing the light source and detector along with the analyzer rotation frequency and the low pass filtering circuits which would also have a bearing on the precision.

To determine the typical precision of the ellipsometer, the normalized Fourier coefficients were measured with the ellipsometer in the straight-through mode (no sample). The standard deviations for $\alpha$ and $\beta$ were $5 \times 10^{-6}$ and $9 \times 10^{-6}$, respectively, measured at a wavelength of 500 nm over a 40 minute period, with each point averaged over 500 cycles (Fig. 4.2(a)). Therefore the precision in $\tan\psi$ and $\cos\Delta$ is on the order of $1 \times 10^{-5}$, assuming optimum conditions.

The dielectric function of the silicon sample was next measured at 250 points from 1.5 – 6.0 eV. The third derivative of the real part of the dielectric function was then calculated as shown in Fig. 4.2(b). The structures at 3.4 eV and 4.3 eV are related to the critical points in the silicon band structure. This method is especially valuable for correlating the composition of a multi-alloyed semiconductor to the energy gap of the band structure.[34]

## F. ACCURACY

In terms of instrumentation, the most serious impediments to accuracy are 1) the nonlinearity [62] of the detector and the signal processing electronics, 2) incorrect normalization of the Fourier coefficients due to a background signal, 3) alignment of all the optical elements, 4) optical activity of polarizer and/or analyzer and 5) incorrect calibration parameters. As the last three points have already been addressed in the previous sections, the remainder of this section will concentrate on the first two points.
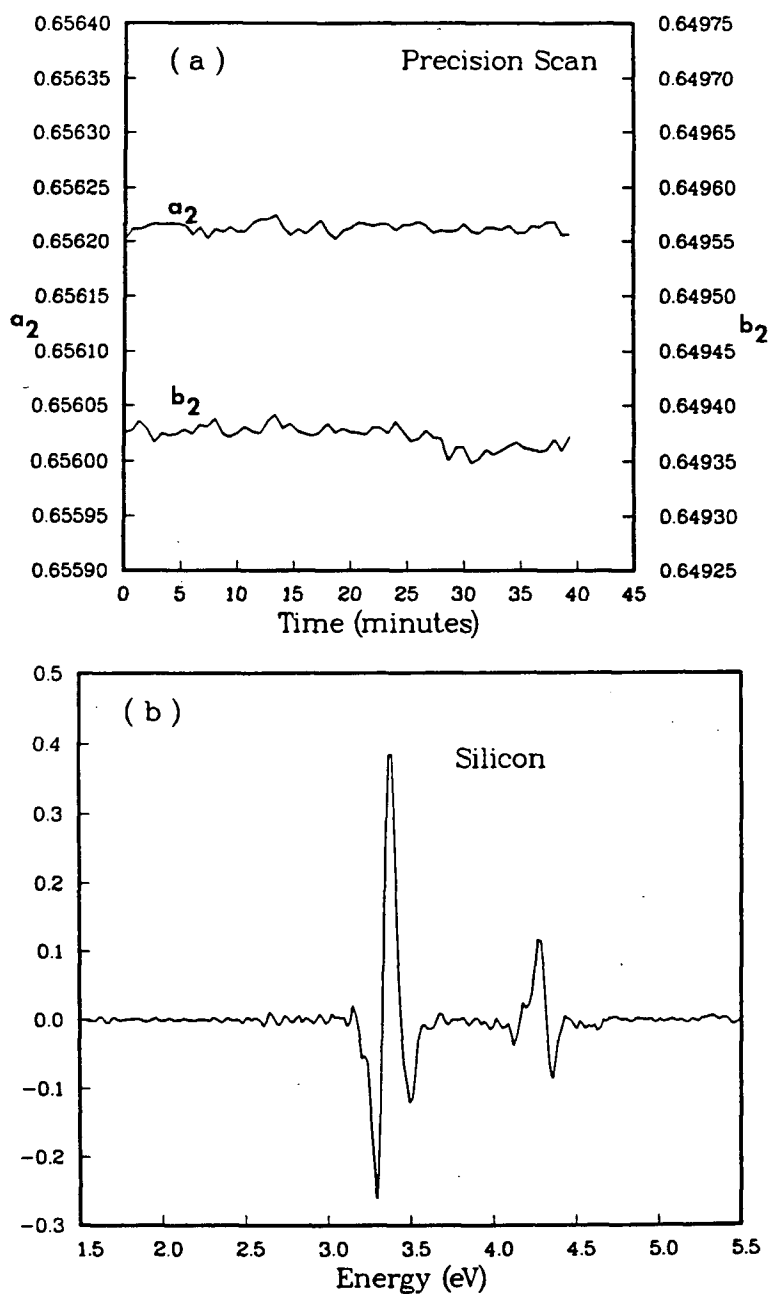
Figure 4.2. (a) Fourier coefficients $(a,\beta)$ measured over 40 minute period with precision $\simeq$ $1\times10^{-5}$. (b) Third derivative of the real part of the dielectric function of Si to enhance the weak structure.

It should be emphasized that an improperly prepared sample may have a more significant effect on the accuracy of the results than the above instrumental systematic errors.[76] Therefore, sample preparation will be discussed in the last part of this section.

### 1. Background Signal

The polarization state of the reflected light is determined from the second harmonic Fourier coefficients normalized to the dc component of the light signal. A background signal arising from stray light, an offset voltage in the A/D converter, or perhaps 60 Hz noise, can significantly affect the accuracy of a measurement if not accounted for during normalization. With the light-tight ellipsometer chamber, the stray light component is essentially negligible. An intentional positive voltage offset was added to the A/D, however, to ensure that the input voltage could never be negative and outside the range of the A/D.

As outlined in the data acquisition section, this background signal can be measured and subtracted from the desired signal. Note, that in some cases the background signal cannot be properly taken into account if it is due to scattered light off the optical elements or to a luminescence from the sample.

### 2. Nonlinearity

Ideally, the light incident upon a detector in a RAE should only have a sinusoidal modulation corresponding to twice the frequency of the rotating-analyzer.[61] Therefore, all the measured Fourier transform coefficients should be lying in the noise regime except for the dc and second harmonic coefficients. A nonlinearity, however, in the detector and/or the signal processing electronics can give rise to a fourth harmonic as follows.

If the measured intensity is,

$$S(I) = I + \gamma' \cdot I^2, \qquad (4.7)$$

where I is given by (2.15), then

$$S(I) = I_0' \{1 + a_2 \cos 2A + b_2 \sin 2A + a_4 \cos 4A + b_4 \sin 4A\} \qquad (4.8)$$

where,

$$a_2 = \alpha(1 + 2\gamma)/\zeta \qquad ,(4.9a)$$

$$b_2 = \beta(1 + 2\gamma)/\zeta \qquad ,(4.9b)$$

$$a_4 = \gamma(\alpha^2 - \beta^2)/2\zeta, \qquad (4.9c)$$

$$b_4 = \gamma\alpha\beta/\zeta, \qquad (4.9d)$$

and

$$\gamma = \gamma' I_0, \qquad (4.9e)$$

$$\zeta = 1 + \gamma(1 + \tfrac{1}{2}[\alpha^2 + \beta^2]) \qquad (4.9f)$$

Therefore, the amplitude of the fourth harmonic coefficients is a measure of the nonlinearity in the RAE. Note that the azimuth angle of the reflected light (2.16a) is not affected by the nonlinearity, as expected, since $\beta/\alpha = b_2/a_2$. In Fig. 4.3a, the theoretical effect of a nonlinearity on the dielectric function of silicon is calculated. To test the above equations, a silicon sample was measured after creating a large nonlinearity in the PM detector. In Fig. 4.3b, the experimental and theoretical effects of the nonlinearity are in good agreement.

The PM detector, previously discussed in Chapter II, is one of the sources of the nonlinearity present in the ellipsometer. Passive techniques to improve the detector linearity such as minimizing the divider network resistance were able to reduce the
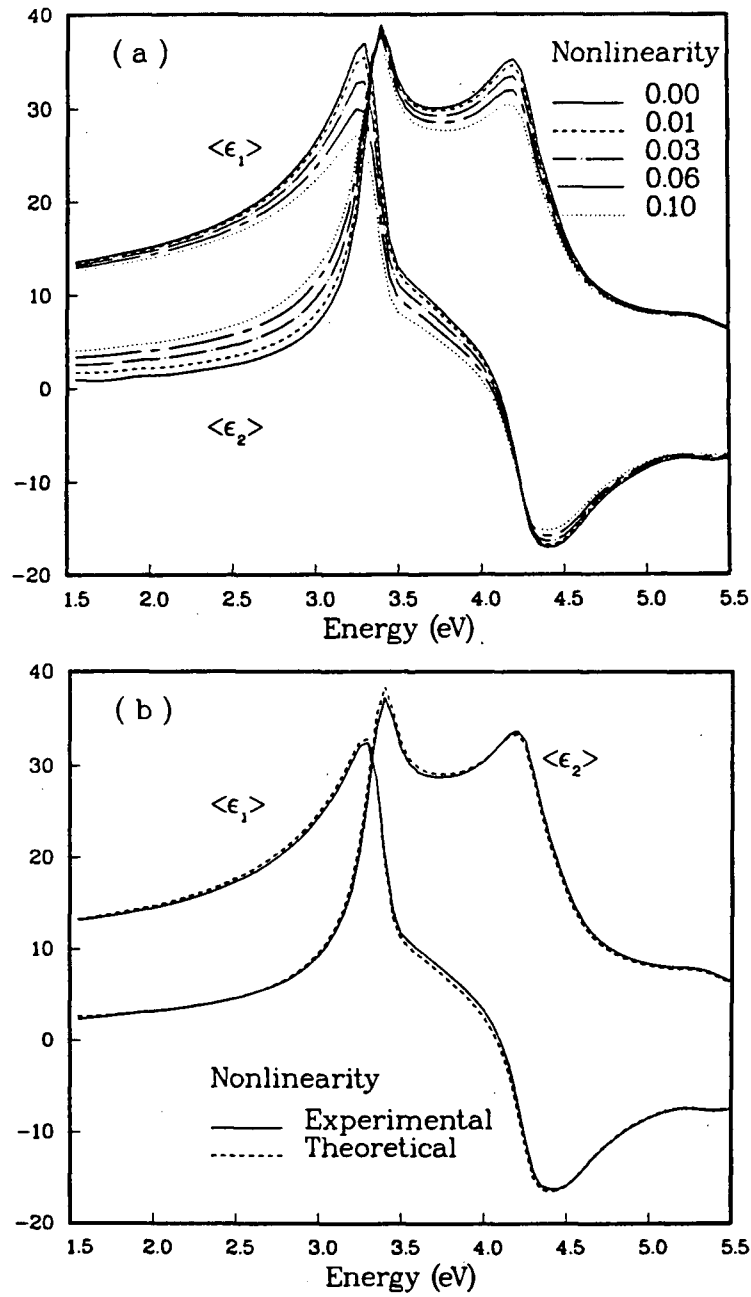
Figure 4.3. (a) Theoretical effects of increasing ellipsometer nonlinearities on the measurement of the dielectric function of Si. (b) Theoretical and experimental curves for nonlinearity in the spectroellipsometer.

amplitude ratio of the 4th harmonic to the 2nd harmonic to $1 \times 10^{-3}$. Aspnes and Studna[64] described an active technique to minimize not only the detector nonlinearity but that due to other components as well. With this method, a small voltage proportional to the anode current is fed back to the PM supply voltage. This feedback voltage is adjusted until the amplitude of the 4th harmonic coefficient has been minimized. It is clear that since the nonlinearity of the PM may change by a factor of three over the voltage range 500 – 1500 V, the total nonlinearity of the system is not necessarily minimized over all wavelengths. As well, the phase of the feedback signal with respect to the PM voltage signal may also be critical.

A linearity control circuit similar to Aspnes and Studna was added to the PM voltage control circuit. The voltage signal from the PM pre-amplifier was sent through an adjustable voltage divider and summed into the input of the PM power supply. However, attempts to reduce the nonlinearity of the system any further were unsuccessful. It was later realized that this was probably due to the feedback voltage being $\simeq 22°$ out of phase to the PM supply voltage. Modifications to eliminate this phase difference (or perhaps make it adjustable) are being made to the linearity control circuit and further tests will be made.

There exists another, less obvious, source of nonlinearity in the RAE with regards to the uniformity of the sampling interval of the intensity.[75] The discrete Fourier transform of a measured data set assumes that the sampling has been uniformly spaced. If, however, there is a periodic variation in the sampling interval due to a systematic error in triggering, this leads to a nonlinear distortion of the light signal similar to that caused by the PM. To check the sampling uniformity, a 68000 assembly program was written to measure the time interval between the encoder pulses. This revealed that although there was a fourth harmonic variation evident (attributed to

vibration in the analyzer) its amplitude was less than 0.01°. Numerical calculations were performed which ensured that this slight variation in triggering had no significant effect on the overall accuracy of the ellipsometer.

To check that there were no major systematic errors present in the ellipsometer the dielectric function of a silicon sample, kindly loaned by Aspnes of Bell Communications Research (BellCore), was measured. The silicon sample had been previously measured on the rotating-analyzer ellipsometer at BellCore and, as seen in Fig. 4.4, the agreement between the two sets of data is very good.[75] The slight difference in the spectra between 2.5 - 3.5 eV might be due to a small nonlinearity or misalignment in the instrument.

## 3. Sample Preparation

For completeness, it should be stated that a major impediment in determining accurate optical constants of solids involves sample preparation and not instrumentation.[76] The microstructure of thin films, for example, can be significantly influenced by the deposition technique, which in turn changes the apparent dielectric function of the films. In bulk samples as well, oxidation or contamination overlayers also affect the accuracy of the results.

There are several approaches that can be taken in dealing with this problem.[28] One, as in the case of bulk samples with surface roughness or contamination overlayers, is to strip off the overlayers or etch away the roughness layer. Then the optical properties of the sample should be measured quickly in an inert atmosphere to prevent re-oxidation or contamination of the surface. Blowing the surface with dry $N_2$ at low pressure is one method to reduce further oxidation of the surface. Monitoring the value of $\epsilon_2$ allows one to gauge the quality of a surface using the "biggest is
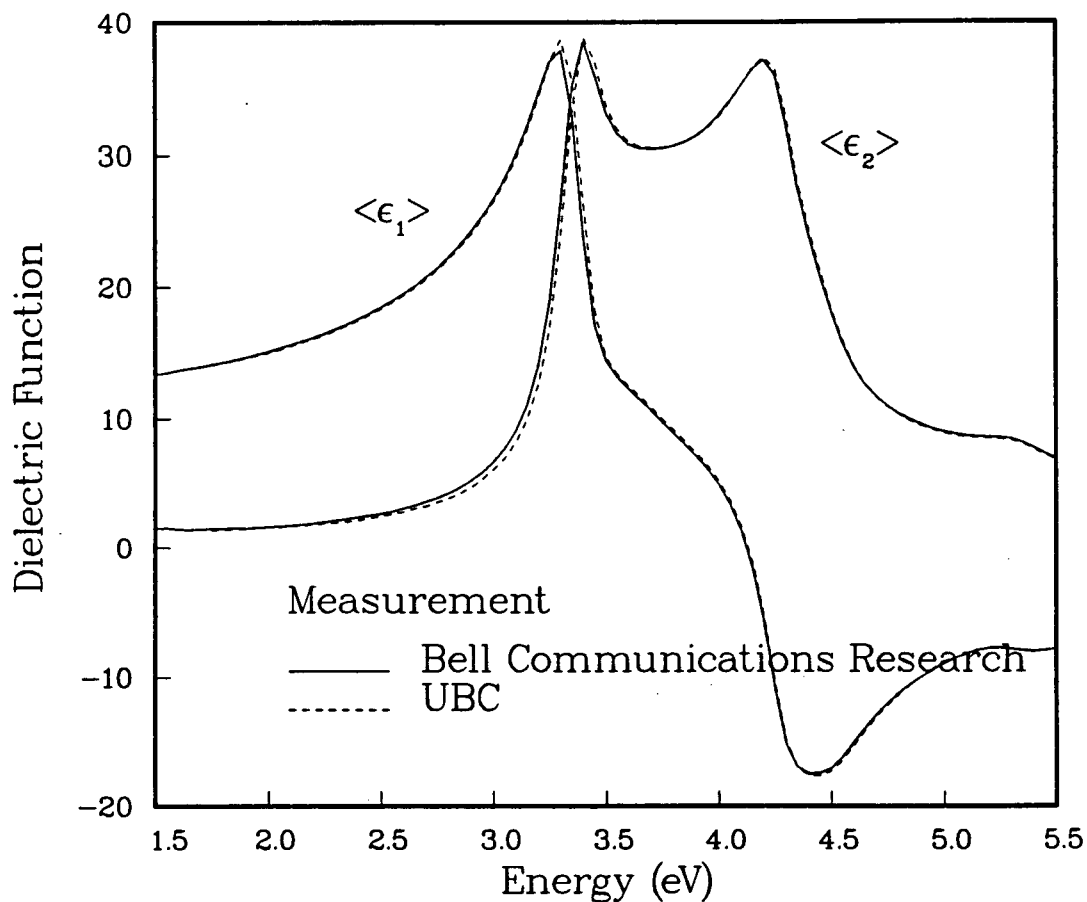
# Silicon



Figure 4.4. Comparison of Si dielectric function spectra measured on UBC spectroellipsometer and Bell Communications Research spectroellipsometer.

best" rule.[78] Since any overlayers tend to decrease the value of $\epsilon_2$, a surface can be etched and measured at the wavelength where $\epsilon_2$ is largest, for maximum sensitivity, until the maximum value for $\epsilon_2$ is obtained.

Another approach, applicable for thin films, is to vary the preparation conditions and model the resulting film microstructure. Then one can determine the optimal conditions for depositing films with the least porosity or microroughness, if desired.

Ellipsometry, as pointed out in Chapter I, is less sensitive to surface imperfections that cause light scattering which could significantly affect the accuracy of other optical techniques such as reflectometry. An example of this was seen in a Pd thin film which was measured before and after an exposure to 1 atmosphere of $H_2$. As is well known, Pd is able to absorb around 900 times its atomic weight in $H_2$ and this can introduce a large stress into Pd thin films. As a result, the thin film after exposure to $H_2$ was severely cracked all along its surface. The pseudodielectric function of the film remained essentially unchanged, however.

# CHAPTER V. OPTICAL MICROSTRUCTURAL ANALYSIS

## A. INTRODUCTION

In the context of spectroellipsometry microstructure refers to spatial inhomogeneities, such as grain boundaries and voids, on the scale of 10–1000 $\overset{\circ}{A}$ where the inhomogeneities are small compared to the wavelength of light, yet large enough to possess a characteristic dielectric response.[28,77 − 80] Similarly, the film macrostructure can be defined as inhomogeneities greater than 1 $\mu$m, i.e., features resolvable with an optical microscope. Thin films deposited by physical vapour deposition (PVD) can have different microstructures depending upon the preparation conditions and the composition of the film. Cermets, for example, consist of metal grains embedded in a ceramic host, while a large variety of materials deposited by PVD exhibit a random aggregate microstructure where the different phases are randomly dispersed throughout the film. In general, one is interested only in the macroscopic properties of the microstructure, such as the volume fractions of the phases involved, and the overall structure of the material, for instance whether a film is 2– or 3–dimensionally isotropic. This chapter deals with the interpretation of the measured optical properties of a bulk or thin film specimen in terms of its microstructure.

In a microscopic, heterogeneous material there is a dielectric discontinuity across an interface between two phases. As a result, light propagating through the material is either reflected or transmitted at the interface according to Maxwell's equations. Macrostructure, on the other hand, such as surface imperfections or roughness on a film leads mainly to light scattering. Hence, the intrinsic optical properties of a material are determined by the microstructure rather than the macrostructure. Now, the effective dielectric function of a film depends primarily upon the composition and

volume fraction of the phases present in the film. At one extreme all the atoms may be interdispersed on an atomic scale while at the other extreme, crystallites of different phases can form homogeneous regions, or grains. In the latter situation, an externally applied electric field leads to formation of a screening charge at the phase boundaries (i.e., grain boundaries), modifying the local field, and hence the dielectric response. Hence a given phase, depending upon its polarizability, can be effectively screened such that its contribution to the overall dielectric response to the applied field is less than that expected on the basis of its volume fraction. The total extent of the screening depends upon the size, shape and orientation of the grains with respect to the applied field.

In optical microstructural analysis, one is therefore interested in solving the inverse problem of deducing the film microstructure from the measured optical properties, i.e., dielectric function. In this regard, the polarized light beam acts as a nondestructive probe into the underlying microstructure in a material. It must be emphasized, however, that inverse problems by their very nature may have more than one acceptable solution if not enough information is available. It is for this reason that accurate dielectric function data over a large spectral range is required to differentiate between possible microstructures.

To characterize the film microstructure, the data were analyzed using a now standard procedure developed by Aspnes.[80] In this method an n-layer model of the film is first constructed, with each individual layer representing a certain aspect of the film, i.e., surface microroughness, bulk film porosity, oxide layers, etc.,.[80-83] Furthermore, as discussed above, the multi-phase layers require an appropriate effective medium theory (EMT) to account for charge screening between the phases. A necessary prerequisite for this analysis is the availability of bulk or reference dielectric data for

all the constituent phases comprising the film.

Wavelength independent parameters such as the volume fractions for each phase and the thicknesses of the individual layers, etc., are then used in the model to calculate the theoretical complex reflectance ratio, $\rho_{calc}$, throughout the spectral range of interest. Nonlinear optimization[84,85] and linear regression analysis[86] (LRA) determine the wavelength-independent parameters by fitting $\rho_{calc}$ to $\rho_{exp}$, the theoretical and experimental complex reflectance ratios, respectively. The LRA provides an estimate of the quality of the fit along with 90% confidence limits on the best-fit parameters and the cross-correlation amongst them. The best models were selected on the basis that the resulting film microstructure was consistent with physical expectations and that the fits to the data were good while maintaining simplicity and reasonably small parameter uncertainties.

In the rest of this section, each of the above steps in the modelling process will be discussed. This will be followed by a description of how the actual optical modelling procedure was implemented.

## B. N-LAYER MODEL

As mentioned previously, the first step in determining the film microstructure is to construct a physical model of the film and from that calculate the theoretical complex reflectance ratio, $\rho_{calc}$. This involves calculating the complex reflectances $r_p$, $r_s$ which in turn are dependent upon all the layer interfaces and thicknesses throughout the film. Simple ambient-substrate and ambient-film-substrate systems have been examined in Chapter II and these theoretical equations can be extended to include further layers if necessary.[1,60,61] With these results, the change in the complex reflectance ratio due to contamination or oxide layers can be modelled as well as that due to surface

microroughness.[80 – 83]

## C. EFFECTIVE MEDIUM THEORY

When a thin film is composed of two or more phases it is necessary to determine the effective dielectric function, $\epsilon$, of the film. This is the province of effective medium theories (EMTs) which take into account the composition, relative volume fractions and the size and shape of the grains throughout the film.[77,87] In this section the multi-phase films are assumed to be microscopically heterogeneous (grains) but macroscopically homogeneous. The dependency of the dielectric averaging process upon the size, shape, and orientation of the grains with respect to the applied field will be discussed. Then a description of several EMTs will be given along with their applicability followed by the bounds on the allowed values for the effective dielectric function, even if the exact microstructure is not known.

The dielectric response of a material is defined as the dipole moment per unit volume and is dependent upon the composition and microstructure. Averaging of the microscopic fields leads to the macroscopic dielectric function defined by,

$$D = \epsilon E = 4\pi P + E \qquad (5.1)$$

where $E$ is the applied electric field and $D$ and $P$ are the resultant displacement and polarization fields, respectively. Thus, solving the microscopic fields for a certain microstructure and then averaging, one obtains the macroscopic dielectric function of interest. Extending this approach to multi-phase materials then leads to different EMT's depending upon the assumed microstructure.

A nice treatment of this problem is given by Aspnes[87] where he develops several of the more common EMTs starting from a simple Clausius-Mossotti model as

follows. For a cubic lattice of atoms with polarizability $a$ one has,

$$\frac{\epsilon - 1}{\epsilon + 2} = \frac{4\pi}{3} n a \qquad (5.2)$$

similarly, for a microstructure consisting of atoms with two different polarizabilities $a_a$ and $a_b$ located randomly throughout a cubic lattice, i.e., interdispersed on an atomic scale,

$$\frac{\epsilon - 1}{\epsilon + 2} = \frac{4\pi}{3} (n_a a_a + n_b a_b) \qquad (5.3)$$

If the individual dielectric functions $\epsilon_a$ and $\epsilon_b$ are known, the above equation gives the familiar Lorentz-Lorenz equation,[88,89]

$$\frac{\epsilon - 1}{\epsilon + 2} = f_a \frac{\epsilon_a - 1}{\epsilon_a + 2} + f_b \frac{\epsilon_b - 1}{\epsilon_b + 2} \qquad (5.4)$$

where $f_a$, $f_b$ are the volume fractions of the 'a' and 'b' phases, respectively.

In solids, the assumption of a vacuum host dielectric is usually not valid, especially if the phases form microscopic homogeneous regions. Furthermore, the microstructure may not possess spherical symmetry and as a consequence the individual phases are screened to a certain extent depending upon the shape and orientation of the grains with respect to the applied field. Thus in general for a two-phase system,[77]

$$\frac{\epsilon - \epsilon_h}{\epsilon + \kappa_z \epsilon_h} = f_a \frac{\epsilon_a - \epsilon_h}{\epsilon_a + \kappa_z \epsilon_h} + f_b \frac{\epsilon_b - \epsilon_h}{\epsilon_b + \kappa_z \epsilon_h} \qquad (5.5)$$

where $\kappa_z$ is the screening parameter and $\epsilon_h$ is the host dielectric function. The Lorentz depolarization factor[90] $q_z = 1/(1 + \kappa_z)$ determines the geometrical screening effect of the grains depending on the orientation of the applied field, where

$0 \leq q_z \leq 1$. For spherical grains or a 3-dimensional isotropic microstructure, then $q_z = 1/3$ or $\kappa_z = 2$. similarly, $q_z = 1/2$ or $\kappa_z = 1$, would be appropriate for a 2-dimensional isotropic microstructure corresponding, for instance, to a thin film with a columnar structure.

In (5.5) the choice of $\epsilon_h = \epsilon_a$ or $\epsilon_h = \epsilon_b$ leads to the Maxwell-Garnett[91,92] (MG) effective medium theory. The MG theory is applicable to a cermet type of microstructure where one phase is encapsulated by the other phase.

However, for some materials it may not be apparent which phase is the host, especially if the volume fractions are nearly equal. Then a self-consistent solution is to choose the effective dielectric function itself to be the host, $\epsilon_h = \epsilon$. With this choice one obtains the Bruggeman[93] effective medium approximation (EMA) which describes a random aggregate microstructure. Many different films prepared by evaporation or sputtering are best described by the EMA.

More recently, a new effective medium theory has been developed by Sen, Scala, and Cohen[94] (SSC) and is relevant for a random coated-particle microstructure where the metal grains are optically isolated from each other.[95,96] Their motivation for deriving this theory was to explain the low frequency conductance of porous sedimentary rocks containing small amounts of water. A conductance path through the rocks was still possible even for small water porosities due to the connectivity of the water channels. For thin metal films, the situation is reversed with the metal grains isolated by void boundaries and if the connectivity of the void channels is high enough then the metal grains become optically isolated and the SSC theory is more appropriate than the EMA.

A brief description of the derivation of the SSC for thin films is as follows. If a metal grain with a dielectric function

$\epsilon_m$ has a coating $\epsilon_v$, then an effective dielectric function for the coated-particle can be derived *geometrically*. If the EMA is used to average over all the coated-particles in the material, it can be shown that,

$$\frac{\epsilon - \epsilon_v}{\epsilon + \kappa_z \epsilon_v} = f_m \frac{\epsilon_m - \epsilon_v}{\epsilon_m + \kappa_z \epsilon_v} \tag{5.6}$$

where $f_m$ is the metal volume fraction. Now this form of the equation is identical to the MG theory assuming $\epsilon_v$ acts as the host phase. However, this equation was derived using a self-consistent approach and unlike the derivation of the MG theory, the question of which is the host phase does not arise. In particular, (5.6) is valid even as $f_v$ approaches zero, whereas in the MG theory the metal phase would normally be considered as the host material.

The next step involves a self-similar model of the material, where the coating of a particle at one level is composed of a mixture of smaller coated-particles. Physically, this corresponds to a fractal approach where the microstructure is essentially the same no matter what scale it is examined upon. Mathematically, this can be realized by using (5.6) to calculate the change in $\epsilon$ when the material at one level is used to coat metal grains for the next level. This is basically the approach used by Hanai[97] in the derivation of the Hanai-Bruggeman (HB) theory which will be discussed shortly. An infinitesimal increment in the total metal volume, $dV_m$, changes the effective dielectric function by $d\epsilon$ where,

$$\frac{d\epsilon}{\epsilon} = \frac{dV_m}{V_m + V_v} \frac{\epsilon_m - \epsilon}{\epsilon_m + \kappa_z \epsilon_v} \tag{5.7}$$

where $V_m$ and $V_v$ are the total volume of the metal and dielectric phases, respectively. Integrating (5.7) over the metal volume fraction, starting from $\epsilon = \epsilon_v$

gives,

$$\frac{\epsilon_m - \epsilon}{\epsilon_m - \epsilon_v} (\epsilon_v/\epsilon)^{q_z} = f_v \qquad (5.8)$$

Note that this is nearly identical to the expression derived by Hanai–Bruggeman, except that the dielectric and metal phases are interchanged. With the HB derivation, the void or dielectric phase is embedded as spheres inside the metal grains, hence, the material remains conducting for small $f_v$, while in the SSC model the grains are optically isolated as a result of the connectivity of the dielectric phase. As well, the SSC is a self–consistent geometrical theory, while the Hanai–Bruggeman expression was derived starting from the MG theory. Note, however, that the Hanai–Bruggeman expression can be derived self–consistently using the SSC approach, except now it is the metal phase which exhibits the high connectivity.

Finally, the bounds on the allowed values of the effective dielectric function will be discussed.[77,87,98–101] As the effective medium theories take into account the geometrical screening of the applied field, one can examine the two extremes of no screening and maximum screening to establish certain bounds. For a two–phase material, if the boundaries between the phases are parallel to the applied field, then no screening takes place and the effective dielectric function is just a simple volume average of the dielectric function of the two phases, i.e.,

$$\epsilon = f_a \epsilon_a + f_b \epsilon_b \qquad (5.9)$$

With the boundaries aligned perpendicular to the applied field, then

$$\epsilon^{-1} = f_a \epsilon_a^{-1} + f_b \epsilon_b^{-1} \qquad (5.10)$$

These two equations are known as the *Wiener* bounds, and place absolute bounds on

the allowed effective dielectric function. Further bounds can be applied if the volume fractions of the phases or the isotropy of the material is known. These bounds can also be used to check if differences in measured dielectric functions can be explained in terms of bulk microstructure or whether a different explanation is required.

## D. NONLINEAR OPTIMIZATION

The motivation for developing the theoretical optical model is to describe the film microstructure in terms of a few wavelength independent parameters and an EMT. Therefore the next step in the modelling process is to determine the parameters which best fit the experimental data for a given model. In this section, the nonlinear optimization methodology will be reviewed along with several different implementations, stating their advantages and disadvantages.[84,85]

In order to determine how well a given model, $\hat{y}(x,\xi_i)$, where $x = (x_1, x_2, ..., x_p)^T$ are the model parameters, fits the measured data,

$$(y_i, \xi_i), \quad i = 1, ..., N \tag{5.11}$$

the following minimization function is constructed:

$$F(x) = \frac{1}{2} \sum_{i=1}^{N} f_i^2(x), \tag{5.12a}$$

where

$$f_i(x) = \hat{y}_i(x) - y_i \tag{5.12b}$$

or,

$$f(x) = \hat{y}(x) - y \tag{5.12c}$$

$F(x)$ is a measure of the difference between the theoretical model and the experimental data, so the object is to minimize this difference by adjusting the

parameters in the model. The gradient is defined by,

$$g = \nabla F(x) = J^T f \tag{5.13}$$

where $J_{ij} = \partial f_i / \partial x_j$ is the Jacobian. For linear least squares,

$$\hat{y} = Jx, \tag{5.14}$$

thus, at the optimization point, $x = x^*$, where $F(x)$ is minimized,

$$g(x^*) = J^T f = J^T \hat{y} - J^T y = 0, \tag{5.15}$$

then

$$J^T y = J^T \hat{y} = J^T Jx \tag{5.16}$$

Solving for $x$,

$$x = (J^T J)^{-1} J^T y \tag{5.17}$$

Hence, the solution for linear least squares is relatively straightforward.

However if $\hat{y}(x)$ is not linear with respect to $x$, the optimization point, $x^*$, has to be reached through iteration. This can be illustrated through the Gauss–Newton minimization technique.

First, begin with an initial value $x_0$. At the kth stage of iteration, $x = x_k$, select a step direction $p_k$ such that,

$$F(x_k + p_k) \leq F(x_k) \tag{5.18}$$

Now,

$$F(x_k + p_k) \simeq F(x_k) + g_k^T p_k + \tfrac{1}{2} p_k^T G_k p_k \tag{5.19}$$

where $g_k^T p_k$ is the rate of change of $F$ in the direction of $p_k$ and $G_k$ is the Hessian of $F$ where,

$$G_{ij} = \frac{\partial^2 F}{\partial x_i \partial x_j} = G_{ji} \qquad (5.20)$$

Expanding $G_{ij}$ leads to

$$G_{ij} = \sum_{i=1}^{N} \left[ \frac{\partial f_i}{\partial x_i} \cdot \frac{\partial f_i}{\partial x_j} + \frac{\partial^2 f_i}{\partial x_i \partial x_j} \right], \qquad (5.21a)$$

or

$$G = J^T J + Q \qquad (5.21b)$$

Near $x^*$, $Q$ is small and can be neglected. Then

$$G \simeq J^T J \qquad \text{(Gauss–Newton)}$$

Let

$$\Phi_k(p_k) = g_k^T p_k + \tfrac{1}{2} p_k^T G_k p_k, \qquad (5.22)$$

Minimizing $\Phi_k$ with respect to $p_k$ gives,

$$G_k p_k = -g_k, \qquad (5.23a)$$

or,

$$p_k = -G_k^{-1} g_k = -(J^T J)^{-1} J^T f_k \qquad (5.23b)$$

The next step is to update $x_{k+1} = x_k + p_k$ and terminate the iteration if the convergence criteria have been satisfied.

The convergence criteria can be stated as follows,

$$| F(x_{k+1}) - F(x_k) | \leq \epsilon \quad \text{and} \qquad (5.24a)$$

$$| x_{k+1} - x_k | \leq \delta \qquad (5.24b)$$

where $\delta$ and $\epsilon$ are specified tolerances. Usually, the above conditions are modified

slightly so as to be independent of scaling in F(x) and x.

There are numerous nonlinear optimization techniques available, but they all have certain advantages and disadvantages depending on the minimization function. They usually differ in how they update the Hessian from one iteration step to the next and in the search direction and search length algorithms. For instance, some algorithms may compute the Newton step direction, $p_k$, as above. While the Newton step leads to convergence very quickly near $x^*$, for some functions $p_k$ may undergo large oscillations away from $x^*$. In the method of steepest descent where the search direction is in the direction of the negative gradient, convergence is assured; however, the process is very slow and inefficient.

Two of the routines employed in this study were the *model trust* algorithms and FLETCH. In the model trust method,[102] the best direction for a given step length is selected. The step length is then increased or decreased depending on whether $F(x_{k+1}) \leq F(x_k)$. In FLETCH, described by Fletcher,[103,104] the algorithm used is a quasi-Newton method, where the step length along the Newton step direction, $p_k$, is varied. Further information on these and other routines can be obtained from numerous books on nonlinear optimization.[84,85]

In the optical microstructural analysis of the thin films, the minimization function used is,

$$F(x) = \frac{1}{2} \sum_{i=1}^{N} |\rho_{exp}(E_i) - \rho_{calc}(x_i, E_i)|^2 \qquad (5.25)$$

where $E_i$ is the photon energy and N the number of data points.

Having determined the optimization point, the next step is to evaluate the integrity of the model and the best-fit parameters. This is accomplished through linear regression analysis.

## E. LINEAR REGRESSION ANALYSIS

Having obtained the best-fit parameters for a certain model, it is now necessary to determine the uncertainty associated with each parameter. These parameter uncertainties along with F(x) help judge the suitability of a given model.

In this section, the results of linear regression analysis (LRA) will first be summarized for linear least squares.[86] Then the validity of applying LRA to the nonlinear case will be argued,[84] followed by a discussion on the criteria for accepting or rejecting models.

For the linear least squares case, the measure of the fit between the theoretical model, $\hat{y}$, and the experimental data, $(y_i, \xi_i)$ is given by the unbiased estimator,

$$\hat{\delta}^2 = \frac{2}{(N-p-1)} F(x) \qquad (5.26)$$

As the number of wavelength independent parameters, p, in the model increases resulting in a smaller F(x), this is partially offset by the prefactor which tries to minimize the apparently better fit through the use of more parameters.

From the previous section for linear least squares it was shown that

$$x = (J^T J)^{-1} J^T y$$

As a result, a covariance-variance matrix, V, can be constructed,

$$V(x) = (J^T J)^{-1} \hat{\delta}^2 \qquad (5.27a)$$

Therefore the variance of $x_j$ is given by,

$$V_{jj} = (J^T J)^{-1}_{jj} \hat{\delta}^2 \qquad (5.27b)$$

and the standard error by,

$$s_j = \sqrt{V_{jj}} \qquad (5.27c)$$

Confidence limits on the optimization parameters, assuming they are normally distributed, can then be established from the Student-t distribution for (N−p−1) degrees of freedom. The $100(1-a)\%$ confidence limits are given by,

$$\delta x_j = s_j t_a \qquad (5.28)$$

where $t_a$ is the Student-t number. That is, for a confidence limit of 90%, there is a 90% probability that the true parameter value, $X_j$, lies within the region

$$x_k - \delta x_j < X_j < x_k + \delta x_j$$

However, these confidence limits must be treated with caution. The fit obtained varying one parameter $x_j$ by $\delta x_j$ might be very poor, but by varying a different parameter within its confidence limits, a good fit can be re-established. Thus the confidence limits for the parameters cannot be used independently of one another. A correlation matrix can also be defined by,[80]

$$C_{ij} = \frac{V_{ij}}{\sqrt{V_{ii}V_{jj}}} \qquad (5.29)$$

where the diagonal elements of this matrix are by definition equal to unity. If any off-diagonal element, $C_{ij}$ approaches $\pm 1$, then the parameters $x_i$ and $x_j$ have a strong cross-correlation between them. As a consequence, the uncertainties in these parameters will be very large as a good fit can be obtained while varying these two parameters together over a large parameter space.

Near the optimization point of a nonlinear model, the parameter region is to a good approximation linear, so that LRA can then be applied. The validity of this, of course, depends upon the extent to which the linear model approximates the true

model.

In the previous section it was shown that the Hessian near the optimization point is given by,

$$G \simeq J^T J$$

Therefore, in analogy with the linear case, the covariance–variance matrix is,

$$V = G^{-1} \hat{\delta}^2 \tag{5.30}$$

The confidence limits then follow as before.

Given the unbiased estimator, $\hat{\delta}$, and the 90% confidence limits, the criteria for accepting a model are as follows. The simplest physical model providing a "good" fit should be chosen over a more complicated model providing an equally good fit. Increasing the number of parameters in a model should increase $\hat{\delta}$ by approximately a factor of 2 if the new model is to be accepted. The confidence limits should not increase as a result of adding another parameter to the model. However, a model should not be precluded on the basis of large cross–correlations alone if a good fit is nevertheless obtained.

In some case, a large uncertainty is not due necessarily to a poor model, but to the fact that the model may be insensitive to that particular parameter. For example, the complex reflectance ratio for an ambient–film–substrate model is insensitive to the actual composition of the overlayer if the thickness is very small ($<10\overset{\circ}{A}$). In this particular circumstance, the composition of the overlayer should be decided on some other physical basis or be assigned arbitrarily as when modelling surface microroughness.

## F. IMPLEMENTATION

In summary, a film model based upon previous experience or physical insight, is first devised and accurate reference dielectric data are supplied for each phase in the film. This model is then solved and the best-fit parameters along with their uncertainties are obtained.

For a given sample, a number of different film models may be attempted before the best model is found and depending upon the model, different sets of reference dielectric data may be required.

For flexibility and to accommodate all the different variations that might be attempted when modelling the film microstructure, an input file for the model was designed, an example of which is shown in Fig. 5.1. This file can be easily modified using a screen editor to change the initial volume fractions or layer thicknesses. The effective medium theory for each layer can be specified as well along with whether or not the volume fractions in an individual layer should be held constant. Three different phases can be specified for each layer and currently four layers, including the ambient layer, are allowed in this file. Each phase is given a suitable name which corresponds to a file containing the representative dielectric function data. Finally, the screening parameter in the effective medium theories is allowed to vary along with the angle of incidence (for alignment checking) if required.

At UBC, a nonlinear monitor is available on the mainframe computer which provides access to a wide variety of optimization routines. A Fortran function subroutine is required which has as input the array of optimizing parameters and returns the rms deviation between the theoretical and complex reflectance ratios. The subroutine first calculates the effective dielectric function for each layer, involving the solution of a nonlinear equation for the EMA and SSC theories, and then determines

```
** Optical Model for Microstructure and Composition Analysis **

Description: Palladium Films- Argon Partial Pressure

ANGLE OF INCIDENCE :67.50:
***************************************************************
Layer------|phase(1)/volume|phase(2)/volume|phase(3)/volume|thickness
Ambient    Air     1.0000 None    0.0000 None    0.0000 0.0000
Film 1     pdref   0.5000 Void    0.5000 None    0.0000 0.0000
Film 2     None    1.0000 Void    0.0000 None    0.0000 0.0000
Substrate  pdref   1.0000 Void    0.0000 None    0.0000 0.0000
***************************************************************
Effective Medium Theory | Constant |   Global           | Initial
Layer_____|emt|_____ |_Volume__|_Parameters_____   |_Values___
Ambient     SSC           no        Screening [kz]  no   2.0000
Film 1      SSC           yes       Grain Size      no   1.0000
Film 2      SSC           no        Incident angle  no   67.500
Substrate   SSC           no        Unused          no   0.0000
***************************************************************

Phase      <Data File>         Description of File:
None       Internal            <no material specified>
Air        Internal            <ambient values generated>
Void       Internal            <ambient values generated>
al2o3      Internal            Malitson's formula
SiO2       Internal            Malitson's formula
Data       pdar30r.data        Measurement : 30 mTorr
pdref      pdar5e.data         Reference :    5 mTorr
pdo        pdoe.data           palladium oxide
```

Figure 5.1. Input file for optical microstructure modelling program for a typical film.

the theoretical reflectance ratio based on the number of layers in the model. Prior to being called, however, the subroutine has to be initialized by reading in the film model file described above and determining the number of optimizing parameters in the model as well as reading in all the data files. Each data file is also checked to ensure the number of data points and the interval between each point are the same for all files.

After initialization, a nonlinear optimization routine can be called to determine the best fit of the model to the data. Due to the complexity of the model, the gradients and the Hessian of the above function are calculated numerically. After optimization, another routine is called which returns with the unbiased estimator, the best-fit parameters along with their 90% confidence limits and the parameter cross-correlation matrix.

# CHAPTER VI. CHARACTERIZATION OF PALLADIUM THIN FILMS

The morphology of thin films grown by physical vapour deposition can be significantly influenced by the preparation conditions[70,71]. It is therefore essential to understand the relationship between the deposition parameters and the resulting microstructure. In this chapter, palladium thin films were deposited while independently varying the substrate temperature,[105] argon partial pressure,[106] and the rf-induced substrate bias.[107] The films were then examined by spectroscopic ellipsometry and other surface analysis techniques to determine the film microstructure. A comparison of the optical constants of the "best" dc sputtered film is also made to previously reported values in the literature.

## A. INTRODUCTION

For thin films prepared by sputtering it is well known that the argon partial pressure and substrate temperature can play a significant role in determining the film microstructure.[70,71,108,109] Thornton[70] devised a structure zone model where the film microstructure could be classified with respect to the argon partial pressure, $P_{Ar}$, and to the deposition temperature normalized to the melting point, $T_m$, of the coating material, $T/T_m$. For low substrate temperatures ($T/T_m < 0.3$) and low argon pressures ($< 5$ mTorr) the film microstructure consisted of densely packed, poorly-defined fibrous grains[70] (zone T). With increasing argon pressure the film morphology underwent a transition to a zone 1 region defined by a columnar grain structure with well-defined void boundaries.

In addition Hoffman and Thornton[110 - 112] have shown through a series of experiments, reviewed in Ref. 71 that for dc magnetron sputtering many deposited metal films are in a state of compression at low argon pressures while above a transition pressure, $P_t$, the films enter into an unstressed or tensile state. They

identified $P_t$ with the zone 1/zone T transition in the microstructure and found that $P_t$ was dependent upon the energy flux reaching the substrate as follows[71].

In the regime of low adatom mobility ($T/T_m < 0.3$), the film growth is dominated by atomic shadowing and random clustering about nucleation centres. Furthermore, interatomic forces generated from deposited surface atoms unable to reach minimum energy sites result in an intrinsic stress being formed throughout the film. For magnetron sputtered thin films, the zone T structure formed at low argon pressures is the result of a considerable energy flux directed toward the substrates, primarily from argon ions that have been neutralized and reflected at the target.[113] This energetic bombardment transfers a downward momentum to atoms beneath the surface region promoting a more densely packed structure and introducing a compressive stress into the films. At higher argon pressures, however, increased gas scattering results in a more oblique incident deposition flux as well as a reduced energy flux to the substrate since the energy of the primary neutrals has decreased due to the lower target voltage.[67] Above the transition pressure the effects of the oblique deposition flux become dominant over the energy flux and the films develop into a more voided columnar structure characteristic of a zone 1 region due to the enhanced atomic shadowing. As well the film is either in an unstressed or tensile state, similar to films prepared by evaporation. Thus, the transition from the zone T to zone 1 region, and the argon pressure at which it occurs, is dependent upon the parameters which affect the energy flux reaching the substrate.

The technique of bias sputtering or ion plating where a film substrate is dc biased during deposition has been widely used to optimize thin film physical properties. [71,118 - 121] For an insulating film substrate, a rf-induced bias can be established on the substrate due to a difference in the electron and ion mobilities. This results in an

increased ion bombardment of the film and higher substrate temperatures. The optimization of the desired film properties can be achieved by controlling the degree of ion bombardment through the dc bias voltage and rf input power.

The enhanced ion bombardment of the film surface and the substrate holder during deposition leads to resputtering of the deposited material and possible contamination of the film. The substrate holders should be designed to achieve uniform resputtering over the film surfaces while minimizing the possibility of film contamination. Vossen *et al.* showed that the amount of resputtered material backscattered to the film can be controlled by varying certain deposition parameters.[119] To minimize film contamination the resputtering rate should be greater than the backscattering rate and the substrate holder should ideally be of the same composition as the film being deposited.

In this study, the microstructure of palladium thin films deposited by dc magnetron sputtering is examined as a function of substrate temperature, dc power, film thickness and argon partial pressure using spectroscopic ellipsometry, scanning electron microscopy (SEM), transmission electron microscopy (TEM) and X-ray diffraction (XRD). Spectroscopic ellipsometry is an indirect technique able to provide quantitative information on the film microstructure in terms of the film porosity, microroughness, etc., as well as determining the type of microstructure (i.e. cermet, random aggregate, ...), through an effective medium analysis (Chapter V). Electron microscopy, on the other hand, allows the film structure to be determined directly from an observation of the film's surface and cross-section while XRD provides information on the stress and the preferred orientation of the film.

The purpose of this investigation is to see, through spectroscopic ellipsometry, how the microstructure is affected by the above preparation conditions and relate this

to Thornton's structure zone model. By providing a thorough characterization of the films, it is hoped that the relationship between the zone T/zone 1 regions and the corresponding microstructure and optical properties can be better understood. In particular, it would be interesting to see whether the zone T and zone 1 regions require different effective medium theories to describe their optical properties.

To investigate the effects of simultaneous ion bombardment and moderate substrate temperatures, palladium films were next deposited by dc planar magnetron sputtering with rf-induced substrate bias (bias deposition). After deposition, the films were characterized by spectroscopic ellipsometry to study how the film microstructure was influenced by the substrate biasing.

Since contamination and nonuniform resputtering of the films may occur, two substrate holders were used in the preparation of the films with one smaller and the other larger in diameter compared to the film substrate. This enabled a comparison between the films prepared on the different holders to determine if there was any evidence of contamination affecting the surface smoothness. As well, the resputtering rates across the films surfaces were measured to determine their uniformity and to estimate the ion current and power densities reaching the substrate. The resputtering measurements were made on previously dc deposited films (no biasing) by applying a rf-induced substrate bias to the films in the absence of any dc sputtering. Finally, the deposition rates were measured for films prepared with and without substrate biasing to see how the coating flux reaching the substrate was affected by the bias potential.

## B. EXPERIMENTAL DETAILS

The palladium films in this study were prepared in a diffusion pumped, dc planar magnetron sputtering system previously described in Chapter III. In the substrate temperature study the substrates were placed on a substrate heater, able to vary the temperature from $20^\circ$ C to $200^\circ$ C, located a distance of 8 cm from the target. The films were deposited for two minutes with a dc current and voltage of 1.0 amp and 400V, respectively, while the argon partial pressure was held constant at 5 mTorr. The deposition rate under these conditions was $33\overset{\circ}{A}/sec$ yielding films approximately $4000\overset{\circ}{A}$ thick. As the actual substrate temperature is difficult to monitor during deposition, a calibration between the holder and substrate temperatures was performed in vacuum, with an error of $\pm 10^\circ$ C. While heating the substrate, the base pressure was monitored to ensure there was no significant outgassing from the holder. Each film was prepared individually during separate runs and the ellipsometer measurement was made immediately after removal of the film from the sputtering system.

In the argon partial pressure study, the substrates were located a distance of 12 cm from the target and during sputtering the argon pressure was varied from 5 mTorr to 30 mTorr. Five substrates were mounted on a rotating substrate holder and each film was deposited, at a different argon pressure, for two minutes at a dc current of 1.0 amp. Under these conditions the deposition rate was approximately $25\overset{\circ}{A}/sec$ and the films were nominally $3000\overset{\circ}{A}$ thick. The films examined by TEM were deposited upon carbon coated grids during a separate run.

Finally, in the rf-induced substrate bias investigation, the films were deposited on substrates attached to either a 2 cm or 5 cm diameter substrate holder using silver paint. The substrate holders were attached via a stainless steel rod to a rf feedthrough and no ground shield was used. The substrate holders had a total surface area of

approximately 200 cm$^2$ and were constructed of stainless steel. The holders were attached to a rf power supply (13.56 MHz) through an impedance matching network which minimized the reflected power. The rf forward power could be varied from 0 to 300 W, generating a dc bias voltage from −5 to −1375 V as measured at the matching network. The films were then deposited, with and without substrate biasing, at a constant dc current of 1.0 amp for two minutes, at an argon partial pressure of 5 mTorr.

After deposition, the films were immediately removed from the sputtering system and measured on the ellipsometer. Prior to measurement, the films were rinsed with methanol and blown dry with filtered N$_2$.

## C. SUBSTRATE TEMPERATURE

### 1. Results

The Pd films prepared by sputtering were found to be very reproducible in their optical properties over the three month period of the study. As well, several film runs were repeated at the higher substrate temperatures and verified the substrate temperature reproducibility. All the films produced were highly reflective, with no evidence of 'milkiness' indicative of light scattering, and free of pinholes.

When the dc power was varied from 20W to 600W, there was no significant change in the optical properties of the Pd films. This was also the case when the film thickness was varied from 70 nm to 1500 nm.

The pseudodielectric function data for the palladium films prepared at various substrate temperatures up to 190°C are shown in Fig. 6.1. Both $|<\epsilon_1>|$ and $|<\epsilon_2>|$ decrease with increasing temperature, consistent with either a possible increase
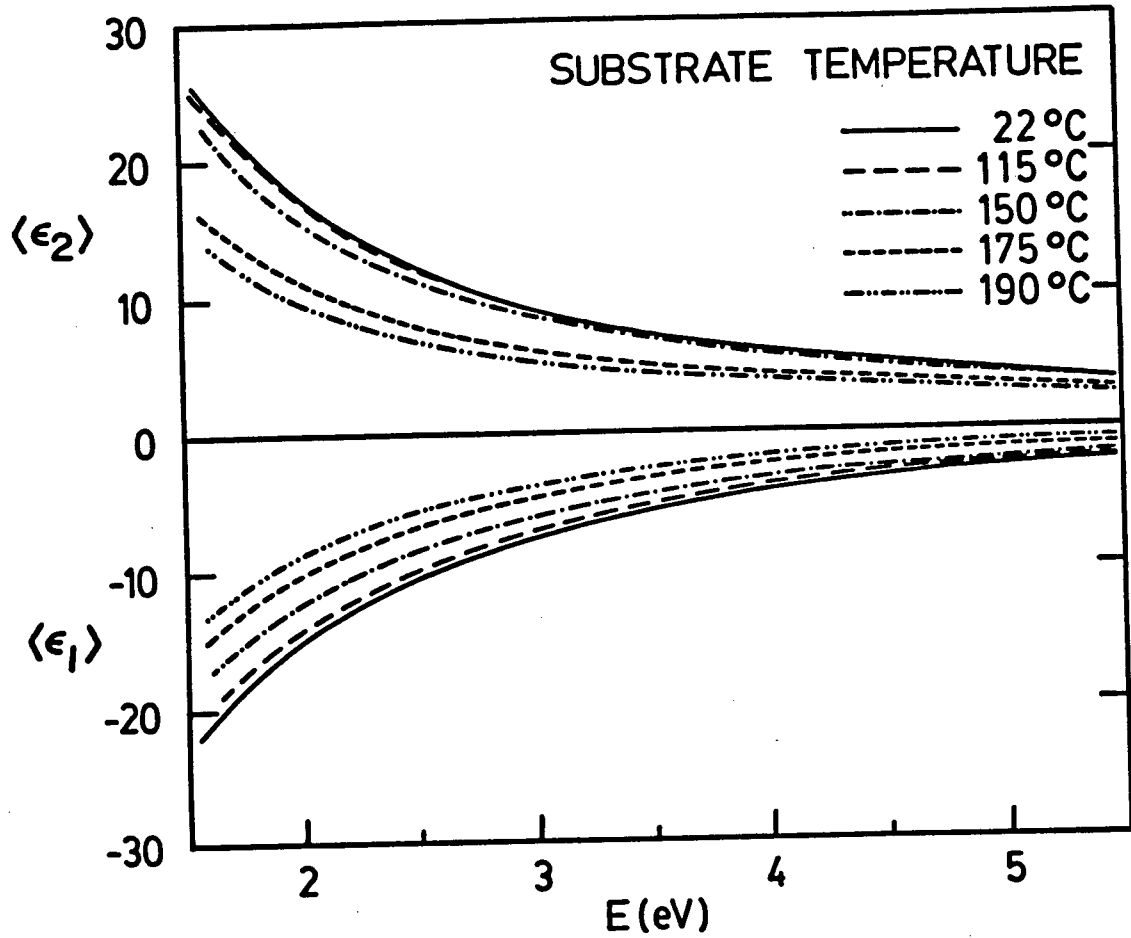
Figure 6.1. Pseudodielectric function $<\epsilon> = <\epsilon_1> + i<\epsilon_2>$ of palladium films deposited as a function of substrate temperature.

in the film porosity and/or the surface microroughness. Grounding of the substrate holder in these runs did not significantly affect the measured dielectic function.

To determine how the film microstructure varied with deposition temperature, several different models were examined to see which provided the best overall description of the Pd films over the temperature range $20^\circ$ C to $200^\circ$ C.

In the models discussed below, the films were assumed to consist of a bulk region and a possible surface microroughness layer. The two principal phases were assumed to be palladium and voids, where the reference dielectric data for the palladium was taken from the film deposited at $22^\circ$ C. Two effective medium theories were examined, first the Bruggeman EMA and then the SSC theory.

In the first model, utilizing the three–dimensionally isotropic Bruggeman EMA, which describes a random aggregate microstructure, the film was assumed to consist only of a bulk region with varying void fractions and a smooth surface. The best–fit parameters, 90% confidence limits and unbiased estimator for this model are presented in Table 6.1. In this one–parameter model, to fit the data for the higher substrate temperature films, the void volume fraction was forced to increase to the point where the palladium density dropped to $74 \pm 2\%$ of that of the reference film. At such a low temperature compared to the melting point of Pd, $T_m = 1552^\circ$ C, this result does not seem reasonable. Nevertheless, the fits to the data are fairly good, especially from 3.0 to 5.5 eV.

Next, surface microroughness was incorporated into the film model, assuming the bulk of the film to be the same density as the reference sample. As seen for model 2 in Table 6.1, the unbiased estimator for the higher substrate temperature films is lower by a factor of three. The trend in the data indicates a growing microroughness with higher substrate temperatures, reaching $88 \pm 6\overset{\circ}{A}$ at $190^\circ$ C with the volume

Table 6.1. Best-fit parameters, 90% confidence limits and unbiased estimator for the various proposed microstructure models described in the text. $f_{pd}$ = Pd volume fraction, d = thickness.

| Model Number | Temperature °C | Surface Layer $f_{pd}$, d | Bulk Region $f_{pd}$ | Unbiased Estimator $\hat{\delta}$ |
|---|---|---|---|---|
| 1 | 115 | ---- | 98 ± 2% | .010 |
|   | 150 | ---- | 93 ± 4% | .022 |
|   | 175 | ---- | 79 ± 2% | .011 |
|   | 190 | ---- | 74 ± 2% | .016 |
| 2 | 115 | 29 ± 43%, 4 ± 5Å | ---- | .010 |
|   | 150 | 30 ± 30%, 17 ± 10Å | ---- | .020 |
|   | 175 | 43 ± 6%, 58 ± 3Å | ---- | .004 |
|   | 190 | 49 ± 5%, 88 ± 8Å | ---- | .006 |
| 3 | 115 | ----- | 98.3 ± 0.6% | .004 |
|   | 150 | 50%, 7 ± 4Å | 96.0 ± 1.4% | .006 |
|   | 175 | 32 ± 4%, 54 ± 2Å | 97.6 ± 1.0% | .002 |
|   | 190 | 30 ± 3%, 80 ± 3Å | 97.0 ± 1.7% | .003 |

fractions of the palladium and voids being equal in the surface layer.

Attempts to model the films with surface microroughness as well as bulk film porosity, using the EMA, led to a very large cross-correlation between the void fraction in the film and the thickness of the surface roughness, an effect previously noted.[81] These large cross-correlations (the correlation matrix element = .99 in one case) result in large uncertainties for the best-fit parameters, with little improvement in the fit.

Next the SSC theory, assuming three dimensional isotropy, was applied in the film modelling procedure. The basis of this theory is a random coated-particle

microstructure such that the connectedness of the void or dielectric network (i.e., grain boundaries) screens the metal volume fraction more effectively than that of a random aggregate described by EMA. One-parameter fits assuming only a bulk film porosity were very poor. However, with the incorporation of surface roughness into the film model, the fits obtained were in excellent agreement with the data. In Table 6.1 the results of this third model, with voids in the bulk region along with surface microroughness, are shown. The fits, improved by a factor of 2 over those of the previous model, again indicate that the surface microroughness increases with substrate temperature, although the Pd volume fraction in the surface layer is lower than that obtained with the EMA model. An interesting aspect of the SSC is the now small cross-correlation between the bulk porosity and microroughness parameters, compared to the same model using the EMA. Models rejected due to poor fits included those with layers composed of palladium/oxide mixtures and any oxide overlayers.

After the above results were obtained from the spectroellipsometry data, the films were examined with electron microscopy and XRD. The micrographs of Pd films deposited at different substrate temperatures, obtained with scanning electron microscopy (SEM), are displayed in Fig. 6.2. The film deposited at $22°C$ was smooth to the extent that at 60K magnification no surface features could be resolved (Fig. 6.2(a)). The trend to increased surface roughness with higher substrate temperatures, indicated by the ellipsometry data, was verified by the SEM micrographs (Figs. 6.2(b)-6.2(e)). The grain structure becomes more noticeable in the higher temperature deposited films and appears to be around 500Å in diameter. The columnar morphology and surface roughness of the $190°C$ deposited film is evident in an SEM micrograph of a fracture cross-section of the film shown in Fig. 6.3(a). In this film the columnar grains have a mean diameter of 500Å and domed tops, with a void separation of 50-100Å
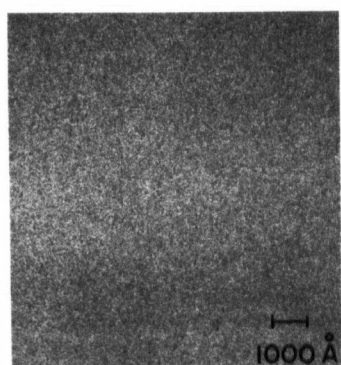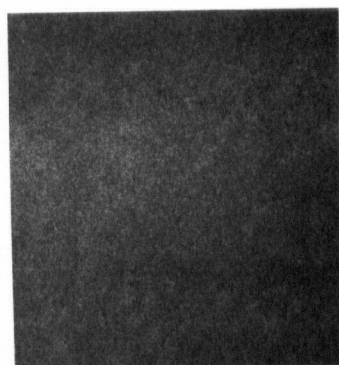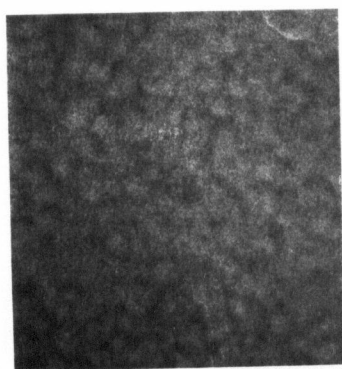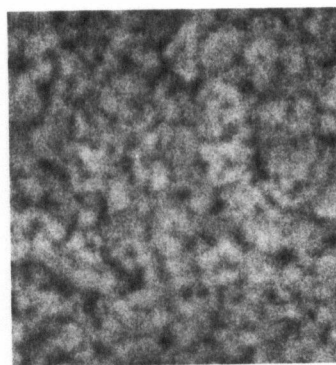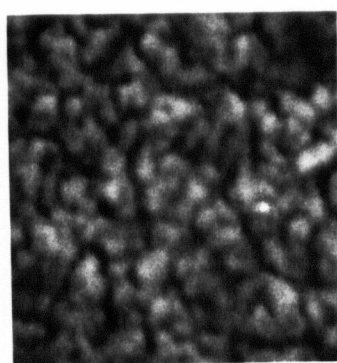
Figure 6.2. Scanning electron micrographs of Pd films versus substrate temperature during deposition. (a) 22°C. (b) 115°C. (c) 150°C. (d) 175°C. (e) 190°C.

between many of the grains, consistent with the surface micrograph in Fig. 6.2(e). Micrographs of the 22°C deposited film indicate an average columnar grain diameter of approximately 300Å. In Fig. 6.3(b), a transmission electron micrograph of a 350Å Pd film deposited at 22°C shows an average crystallite size of 100Å.

Finally, x-ray diffraction analysis revealed the films were polycrystalline. The Pd film deposited at room temperature had a strong preferred (111) orientation with a small (200) peak as observed in other studies.[114] With increasing substrate temperature, however, the preferred crystal orientation of the films changed as the peak intensity ratio $I_{200}/I_{111}$ increased from 3% at 22°C to 27% at 190°C, compared to 42% for Pd powder. Furthermore, as the substrate temperatures were increased, a decrease in the (111) lattice spacing, $d_{111}$, was observed corresponding to a larger compressive stress in the films.

## 2. Discussion

The deposition temperatures, T, examined in this study, 20°C to 200°C, lie in the regime of low adatom mobility, $T/T_m < 0.3$, where shadowing effects and clustering are expected to be dominant during film growth.[71,109] Spectroellipsometry results, based upon the EMA or SSC effective medium theories, indicate a trend to increased surface microroughness with higher substrate temperatures, which was subsequently confirmed by SEM. As well, the palladium volume fraction in the surface layer decreased with increasing microroughness. For example, the surface microroughness of the 190°C deposited film was characterized by a 80Å ± 3Å rms thickness with a Pd volume fraction of 29% with respect to the reference film deposited at 22°C. One possible explanation for the increased surface microroughness is that the growth of larger grains at the higher substrate temperatures leads to a larger relative height difference between

(a)
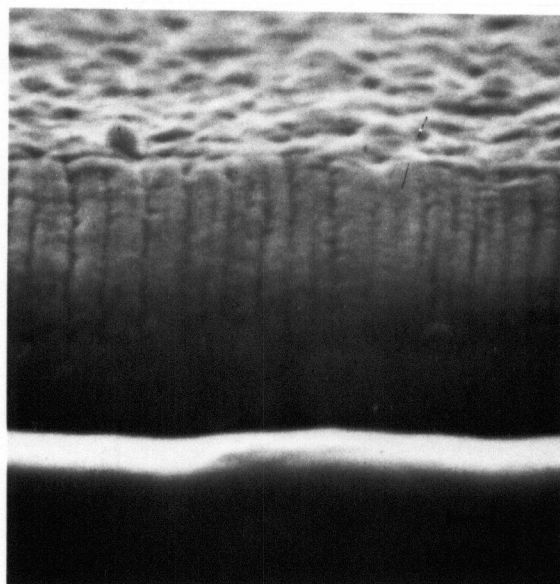


250Å
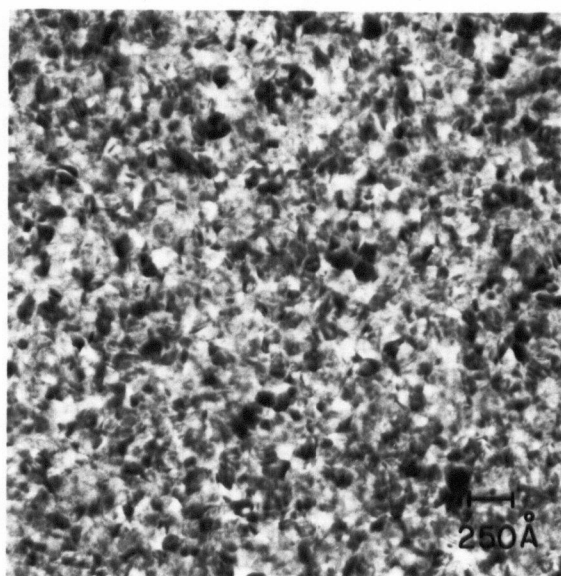
(b)

Figure 6.3. (a) Scanning electron micrograph of a fracture cross–section of the Pd film deposited at 190°C. (b) Transmission electron micrograph of a 350Å Pd film deposited at 22°C.

the individual grains. Alternatively, the microroughness on the surface of each grain may have increased throughout the film.

From the SEM micrographs, the microroughness appears greater than that expected on the basis of the above best–fit models. Indeed, it would be difficult to resolve any features on the scale of 80Å. These results can be reconciled by noting that the spectroellipsometer beam size was of the order of 1 mm², so that the data measured was an optical average over this area.[81] This optical average in turn is dependent upon the distribution of the grain sizes and shapes throughout the film. Thus, the microroughness values obtained from ellipsometry were rms values of the actual microroughness (0 to 1000Å) over the beam sampling area. Previous studies of microroughness measurements have shown spectroellipsometry to be in good agreement with other techniques such as total integrated scattering and profilometry.[82,115]

The XRD analysis indicated a small compressive stress in the Pd films, in agreement with other metal films deposited by sputtering.[108] As well, the strong (111) preferred crystal orientation decreased with substrate temperature towards that of bulk powder palladium.

In conclusion, spectroscopic ellipsometry was able to provide a measure of the overall surface microroughness of the palladium films. From the ellipsometry data, the surface roughness of the films was found to increase with substrate temperature, and this was confirmed by electron microscopy. This microroughness can significantly affect the effective interface region between the palladium film and any subsequently deposited layer. Finally, the SSC theory provided a better description of the film microstructure than the Bruggeman EMA. This is consistent with the sizeable column separation evident in Fig. 6.3(a), where the the void phase is localized about the grain boundaries as opposed to being randomly dispersed throughout the metal film.[95]

## D. ARGON PARTIAL PRESSURE

### 1. Results

All the palladium films prepared at the different argon partial pressures were highly reflective and free of surface imperfections such as pinholes. To check film reproducibility, a second set of films were prepared at the same argon pressures as in the first run. The optical data of the films prepared at the same argon pressure were found to be in good agreement with each other.

Theoretically, as the argon pressure is increased, the scattering of Pd atoms enroute from the target to the substrate should become more pronounced until the deposition is mainly a diffusion process. Consequently, the thickness of the Pd films should decrease with higher argon pressures. To check this, the films were measured with a Tencor stylus profilometer and the thicknesses were found to decrease by 15% from $3100 \pm 100 \overset{\circ}{A}$ at 5 mTorr to $2600 \pm 100 \overset{\circ}{A}$ at 30 mTorr. As well, the target voltage decreased from 390 V at 5 mTorr to 315 Volts at 30 mTorr, with the dc current kept constant at 1.0 amp, thus reducing the energy of the reflected neutrals reaching the substrate. Therefore it is expected that the reduced energy flux and the increased oblique component of the deposition flux over this range of pressures will affect the film microstructure.

The pseudodielectric function of the Pd films versus argon pressure is shown in Fig. 6.4. The magnitude of $<\epsilon>$ is seen to decrease monotonically as the argon pressure is increased. However, for argon pressures greater than 15 mTorr, $<\epsilon_2>$ remains nearly constant while $|<\epsilon_1>|$ continues to decrease. This behaviour in $<\epsilon>$ is reminiscent of the differences seen in the dielectric data of Rh films prepared under different conditions.[95,96,116] Aspnes[95] showed that the Rh data could be explained
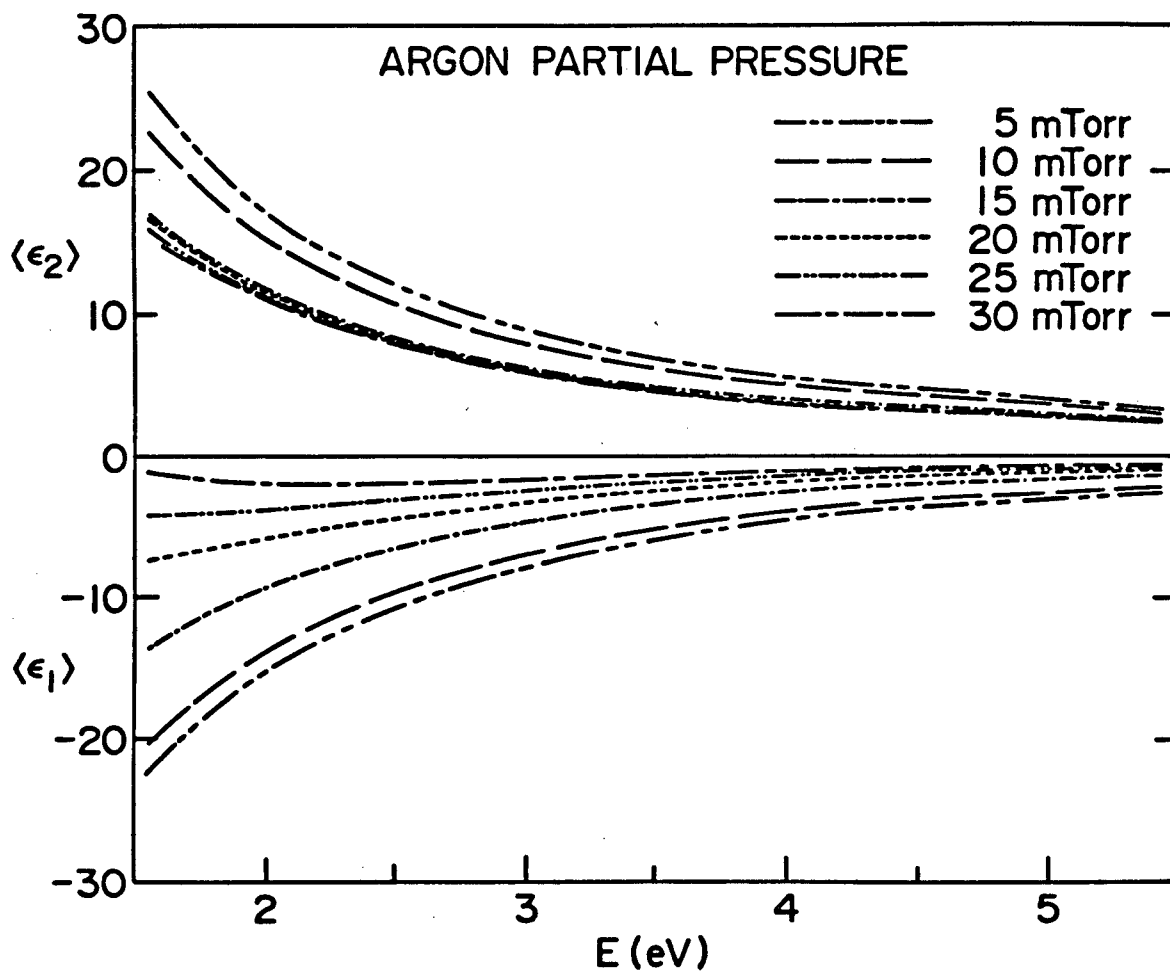
Figure 6.4. The pseudodielectric function $<\epsilon> = <\epsilon_1> + i<\epsilon_2>$ of the Pd films versus argon partial pressure. Note how $<\epsilon_2>$ remains relatively constant for argon pressures higher than 15 mTorr.

using the SSC effective medium theory, describing a metal-rich cermet microstructure where the dielectric or void network effectively isolates the metal grains optically from one another.

In fitting the spectroellipsometric data, different microstructural models were implemented with the criteria that the models should be consistent across the range of argon pressure covered. When modelling film porosity, due to the slow oxidation rate of Pd at room temperature, the dielectric phase was assumed to be voids. The 5 mTorr film was taken to be the palladium reference, so consequently the following best-fit parameters are measured with respect to that film.

First, a one-parameter model was constructed, using the EMA and SSC theories in which the film porosity was varied with the assumption of no surface microroughness. The best-fit parameters are shown in Table 6.2 along with the 90% confidence limits and the unbiased estimator, $\hat{\delta}$. Generally, models were judged to be very good for $\hat{\delta} < 0.010$. In this model, while neither EMT was particularly successful, the SSC theory gave a better description at the higher argon pressures as expected. This can be seen in Fig. 6.5(a), where the best fits based on the EMA and SSC theories are compared to the experimental pseudodielectric data for the 30 mTorr film.

Next surface microroughness was incorporated into the film model, in the form of a surface layer,[81] while assuming no porosity in the bulk region of the film. The thickness of the microroughness layer was calculated on the basis of a 50% Pd volume fraction ($f_{pd}$) in the surface region. From Table 6.3, the rms microroughness values for either the EMA or SSC theory were approximately the same, although the $\hat{\delta}$ for the SSC theory was consistently lower. The average microroughness was found to increase with argon pressure from 15Å at 10 mTorr to 117Å at 30 mTorr.

Table 6.2. Film model incorporating porosity in bulk region of the film, but with no surface microroughness. The best-fit parameters, 90% confidence limits and unbiased estimator are shown for EMA and SSC effective medium theories.

| Bulk Region EMT | $P_{Ar}$ (mTorr) | Bulk Region $f_{pd}$ | Unbiased Estimator $\hat{\delta}$ |
|---|---|---|---|
| EMA | 10 | 93 ± 1% | .003 |
| | 15 | 80 ± 3% | .017 |
| | 20 | 74 ± 7% | .049 |
| | 25 | 70 ± 10% | .074 |
| | 30 | 68 ± 14% | .103 |
| SSC | 10 | 96 ± 4% | .025 |
| | 15 | 86 ± 10% | .073 |
| | 20 | 79 ± 20% | .077 |
| | 25 | 75 ± 10% | .069 |
| | 30 | 72 ± 7% | .057 |

For the SSC theory, the surface microroughness model fares better at lower argon pressures while the bulk porosity model provides better fits at higher pressures. Hence, the true microstructure probably involves a combination of both porosity and microroughness. Therefore, a two-parameter model was next constructed consisting of a surface layer with 50% Pd and void volume fractions, to account for microroughness, along with a bulk film porosity. Attempts to fit this model with the EMA theory led to negative roughness values for the films prepared at argon pressures of 15 mTorr and higher. While the roughness value became positive when the Pd volume fraction in the surface layer was varied, the best-fit parameters had large uncertainties associated with them and the fits remained poor.

The SSC theory was then employed for the bulk film porosity while the SSC,
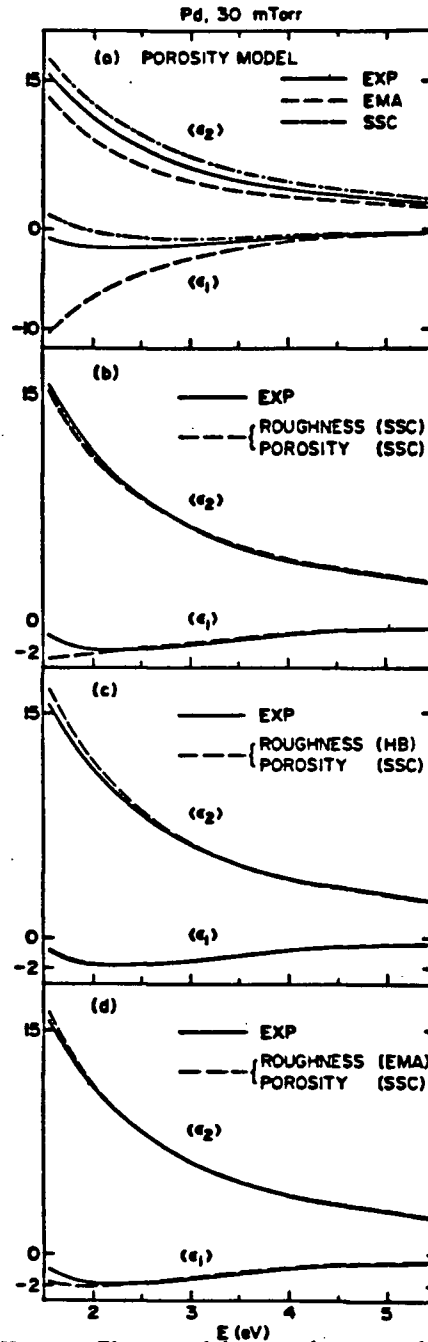
Figure 6.5. Fits of different film models to the pseudodielectric function data $\epsilon$ for the 30 mTorr Pd film. (a) Model assuming only voids in bulk layer of the film and no surface microroughness with the SSC and EMA theories. (b) Model incorporating both surface microroughness (with $f_{pd}=50\%$) and film porosity. The effective medium theories are SSC for the bulk layer and SSC for the surface layer. (c) Same as (b), but with a HB surface layer (d) Same as (b), but with a EMA surface layer.

Table 6.3. Film model incorporating only surface microroughness ($f_{pd}=50\%$) assuming the no porosity in the bulk region of the film. The best–fit parameters, 90% confidence limits and unbiased estimator are shown for EMA and SSC effective medium theories.

| Surface Layer EMT | $P_{Ar}$ (mTorr) | Surface Microroughness d, $f_{pd}=50\%$ | Unbiased Estimator $\hat{\delta}$ |
|---|---|---|---|
| EMA | 10 | $15 \pm 1\overset{\circ}{A}$ | .002 |
| | 15 | $60 \pm 18\overset{\circ}{A}$ | .025 |
| | 20 | $87 \pm 115\overset{\circ}{A}$ | .065 |
| | 25 | $107 \pm 53\overset{\circ}{A}$ | .094 |
| | 30 | $117 \pm 50\overset{\circ}{A}$ | .126 |
| SSC | 10 | $14 \pm 2\overset{\circ}{A}$ | .004 |
| | 15 | $57 \pm 6\overset{\circ}{A}$ | .009 |
| | 20 | $84 \pm 25\overset{\circ}{A}$ | .041 |
| | 25 | $104 \pm 34\overset{\circ}{A}$ | .064 |
| | 30 | $117 \pm 162\overset{\circ}{A}$ | .092 |

HB and EMA theories were applied separately to the surface microroughness layer. The best–fit parameters are given in Table 6.4. All three models, with $\hat{\delta} < 0.020$ for all the Pd films, are a distinct improvement over the previous one parameter models. However, in comparison to the SSC theory, the HB theory provided a consistently better fit, while $\hat{\delta}$ for the EMA theory was smaller by a factor of 2. For the 30 mTorr film the best fits for the above model, using the SSC, HB, and EMA theories for the roughness layer, are displayed in Figs. 6.5(b)–6.5(d), respectively. In Fig. 6.5(b), while the theoretical SSC $<\epsilon_1>$ minimizes the difference with respect to the experimental data, the curves do not closely follow one another, especially between 1.5 – 2.5 eV. In comparison, the calculated $<\epsilon_1>$ based upon the HB theory is in excellent agreement with the experimental $<\epsilon_1>$, as seen in Fig 6.5(c). The lowest

Table 6.4. Film model incorporating both porosity in the bulk region of the film and surface microroughness, assuming 3D isotropy. The analysis for the bulk region uses the SSC model. Best-fit parameters, 90% confidence limits and unbiased estimator are shown for the three different effective medium theories used for the surface layer.

| Surface Layer EMT | $P_{Ar}$ (mTorr) | Surface Microroughness $d$, $f_{pd}=50\%$ | Bulk Region $f_{pd}$ | Unbiased Estimator $\hat{\delta}$ |
|---|---|---|---|---|
| SSC | 10 | $14 \pm 2\text{Å}$ | 100% | .004 |
|  | 15 | $54 \pm 6\text{Å}$ | $98 \pm 2\%$ | .007 |
|  | 20 | $60 \pm 13\text{Å}$ | $90 \pm 3\%$ | .013 |
|  | 25 | $62 \pm 16\text{Å}$ | $84 \pm 4\%$ | .014 |
|  | 30 | $52 \pm 17\text{Å}$ | $78 \pm 3\%$ | .013 |
| HB | 10 | $12.3 \pm 1.3\text{Å}$ | $98.7 \pm 0.5\%$ | .002 |
|  | 15 | $43 \pm 11\text{Å}$ | $91 \pm 3\%$ | .013 |
|  | 20 | $47 \pm 10\text{Å}$ | $82 \pm 2\%$ | .010 |
|  | 25 | $48 \pm 10\text{Å}$ | $75 \pm 2\%$ | .010 |
|  | 30 | $37 \pm 8\text{Å}$ | $71 \pm 2\%$ | .009 |
| EMA | 10 | $14.0 \pm 1.0\text{Å}$ | $99.6 \pm 0.3\%$ | .001 |
|  | 15 | $47 \pm 3\text{Å}$ | $94.2 \pm 0.9\%$ | .004 |
|  | 20 | $51 \pm 5\text{Å}$ | $84.9 \pm 1.3\%$ | .007 |
|  | 25 | $52 \pm 7\text{Å}$ | $78.7 \pm 1.4\%$ | .007 |
|  | 30 | $40 \pm 8\text{Å}$ | $73.4 \pm 1.3\%$ | .008 |

$\hat{\delta}$, obtained with the EMA surface microroughness, gave the best fit to $<\epsilon_2>$ at the expense, however, of $<\epsilon_1>$. The void volume fraction in the bulk of the Pd films is seen to increase with higher argon pressure and by 30 mTorr, 22% – 29% of the film consists of voids, depending upon the effective medium theory used for the surface layer. Hence, the role of gas scattering is more significant than first appears from the 15% decrease in the film thickness, as the palladium volume fraction in the films has also decreased by 20%. The best-fit theoretical and experimental $<\epsilon_1>$ are shown in Fig. 6.6 for the roughness(EMA)/porosity(SSC) model. The theoretical and

experimental $<\epsilon_2>$ curves were not shown as the individual curves could not be discerned due to the large overlap between them.

To check how the presence of a small microroughness on the 5 mTorr reference film would affect the modelling results, a 10$\overset{\circ}{A}$ roughness layer was incorporated into the 5 mTorr data. For the 25 and 30 mTorr films, using the EMA/SSC model, the microroughness decreased by 13$\overset{\circ}{A}$ while the bulk porosity increased by 1%. Therefore, within the 90% confidence limits, the effect of a small surface microroughness on the reference film would be to simply decrease the modelled microroughness values from their true values. That the bulk porosity values did not change significantly can be attributed to the small cross–correlation between the microroughness and bulk porosity parameters in this model.

The above models are 3D isotropic but, as will be seen from the electron micrographs, the Pd films have a columnar structure and therefore a 2D model may be more appropriate. A film anisotropy can be introduced by varying a screening parameter,[77] $\kappa_z$, in the effective medium theories with $\kappa_z = 1$ and 2 for 2D and 3D films, respectively. The best–fit parameters obtained with $\kappa_z = 1$ for the roughness/porosity models are shown in Table 6.5. The HB model could not be calculated with the 50% Pd and void volume fractions with $\kappa_z = 1$ and so was not shown. From the unbiased estimator, the fits based on the 2D and 3D models are equally good with the best fits still given by the EMA/SSC model. Due to the better grain boundary screening in a 2D microstructure, the porosity values for the films have decreased as for example in the 30 mTorr film where the porosity dropped from 26% to 15%. As well, the microroughness values for these films increased, especially for the higher argon pressure films.

Attempts to obtain a better fit with more complicated 3D film models met
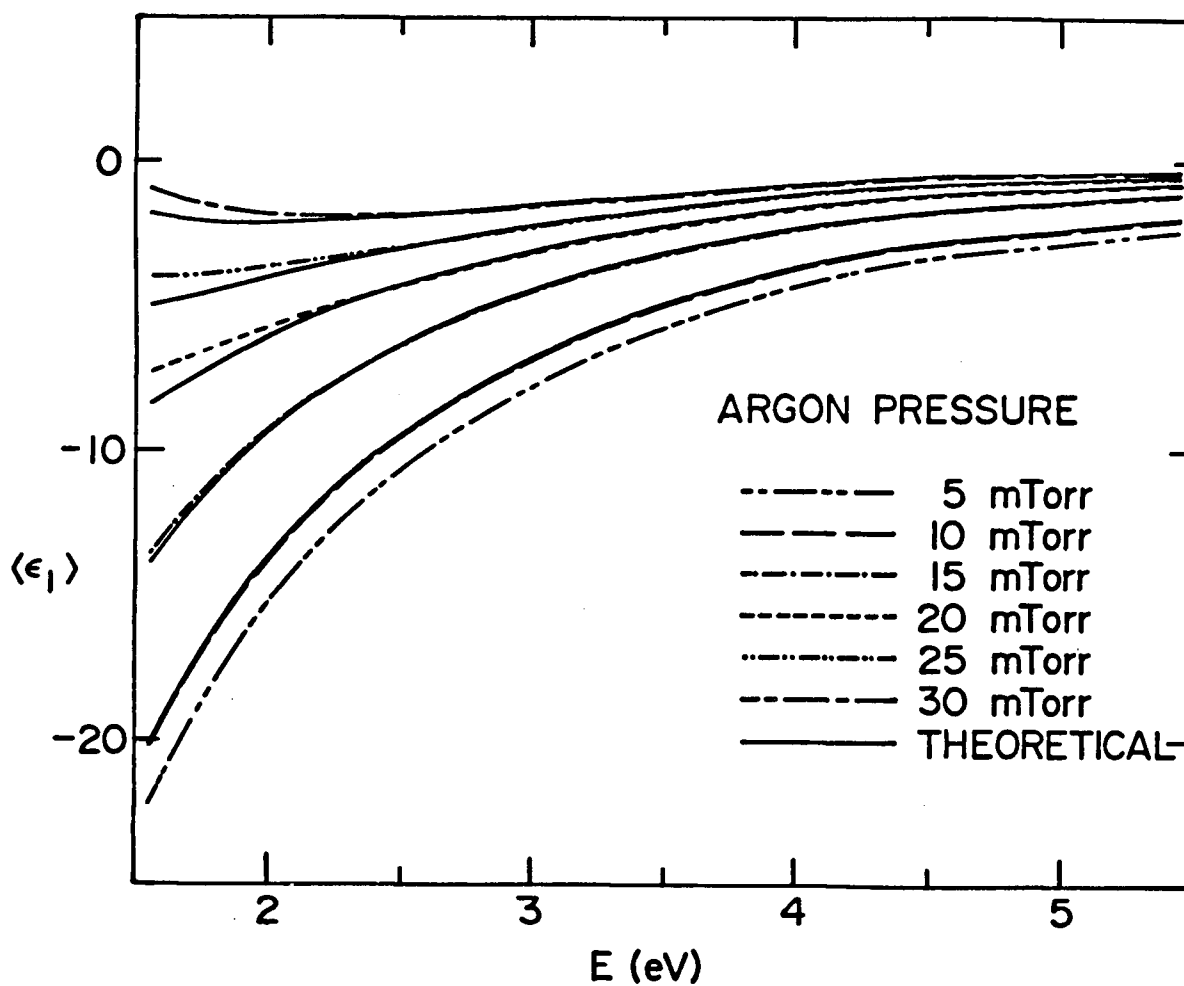
Figure 6.6.    The best fit theoretical $<\epsilon_2>$ curves, based on the 3D
roughness(EMA)/porosity(SSC) film model, compared to the experimental
$<\epsilon_2>$ data for argon partial pressures from 5 mTorr to 30 mTorr.
The fits are in very good agreement except near 1.5 – 2.5 eV for the
higher argon pressure films.

Table 6.5. Film model incorporating both porosity in the bulk region of the film and surface microroughness, assuming two-dimensional isotropy ($\kappa_z=1$). Best-fit parameters, 90% confidence limits and unbiased estimator are shown for models using the EMA and SSC theories for the surface layer and the SSC theory for the bulk regions.

| Surface Layer EMT | $P_{Ar}$ (mTorr) | Surface Microroughness d, $f_{pd}=50\%$ | Bulk Region $f_{pd}$ | Unbiased Estimator $\hat{\delta}$ |
|---|---|---|---|---|
| SSC | 10 | $13 \pm 1\overset{\circ}{A}$ | 100% | .003 |
|  | 15 | $47 \pm 4\overset{\circ}{A}$ | $97 \pm 1\%$ | .0087 |
|  | 20 | $59 \pm 9\overset{\circ}{A}$ | $93 \pm 2\%$ | .015 |
|  | 25 | $66 \pm 11\overset{\circ}{A}$ | $89 \pm 2\%$ | .018 |
|  | 30 | $64 \pm 11\overset{\circ}{A}$ | $86 \pm 2\%$ | .018 |
| EMA | 10 | $15 \pm 1\overset{\circ}{A}$ | 100% | .002 |
|  | 15 | $54 \pm 2\overset{\circ}{A}$ | $98.3 \pm 0.4\%$ | .003 |
|  | 20 | $69 \pm 4\overset{\circ}{A}$ | $93.4 \pm 0.8\%$ | .006 |
|  | 25 | $78 \pm 6\overset{\circ}{A}$ | $89.5 \pm 1.0\%$ | .007 |
|  | 30 | $76 \pm 7\overset{\circ}{A}$ | $85.5 \pm 1.1\%$ | .008 |

with little success. Allowing the palladium volume fraction in the surface layer to vary did not result in any significant improvement where the EMA and HB theories were concerned. Although the model based upon the SSC microroughness did improve by a factor of two, this was only marginally better than the two parameter roughness(EMA)/porosity(SSC) model. To achieve even this factor of two improvement in $\hat{\delta}$, the Pd volume fraction in the surface layer was forced to steadily decrease with argon pressure until $f_{pd} = 8\%$ for the 30 mTorr film. Furthermore, the SSC microroughness/porosity model became singular for argon pressures above 20 mTorr, indicating very strong cross-correlations between parameters. As well, models assuming an oxide or contamination overlayer were discarded.

The films were next examined using XRD to determine the stress and

preferred orientation of the Pd films. [117] The films had a strong (111) preferred orientation which decreased with higher argon pressure. The (111) peaks broadened and shifted with increasing argon pressure. Since the (111) peak positions are related to the interplanar spacing $d_{111}$, the peak shifts corresponding to an increase or decrease in $d_{111}$, are indicative of a tensile or compressive stress, respectively, assuming a stress–strain relationship. In Table 7.6 the change in $d_{111}$, $\Delta d_{111}$, measured with respect to bulk Pd powder is presented. The Pd films had a small compressive stress which gradually increased with argon pressure to a maximum at 15 mTorr. Above this pressure, the compressive stress dropped by a factor of two and remained approximately constant for higher argon pressure.

In Fig. 6.7, TEM micrographs are shown for 350Å Pd films, deposited upon carbon coated TEM grids, prepared at various argon partial pressures. The average crystallite size was approximately 125Å in all the films. From 5 to 15 mTorr, the Pd films were continuous with the grains tightly packed and no evidence of voids ( Fig. 6.7(a), (b) ). In the 20 mTorr film however, a network of small crevices or voids is visible throughout the film, with the largest crevices 25Å in width and extending 300 to 400Å ( Fig. 6.7(c) ). A distinction is made here between the term cracks which implies that the film was torn by stress, and the term crevices which imply the grains during growth never came in contact with one another. Around one–half of the grains have void separations between them throughout the film, with the larger crevices effectively forming clusters composed of 5 to 10 grains each. By 25 mTorr the network of voids has became more extensive with the largest crevices being 50Å in width and 700Å in length as seen in Fig. 6.7(d). Finally by 30 mTorr, most of the grains are isolated by small void boundaries, with larger crevices forming grain clusters around 400Å in diameter. At this pressure, the largest voided areas are 125Å in width
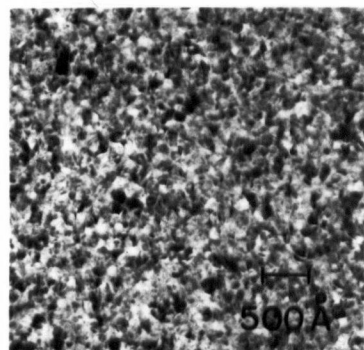
Table 6.6. Interplanar (111) spacing, $d_{111}$, versus argon partial pressure, where $\Delta d_{111} = d_{111} - d_{111}$(bulk).

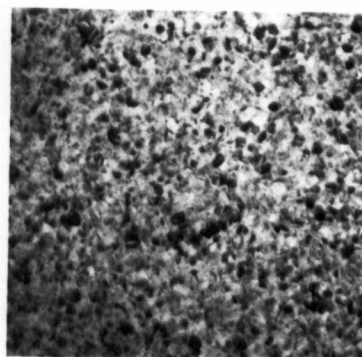| $P_{Ar}$ (mTorr) | $d_{111}$ (Å) | $\Delta d_{111}$ (Å) |
|---|---|---|
| (Bulk) | 2.246 | 0.000 |
| 5 | 2.242 ± 0.001 | −0.004 |
| 10 | 2.236 ± 0.002 | −0.010 |
| 15 | 2.230 ± 0.003 | −0.016 |
| 20 | 2.238 ± 0.003 | −0.008 |
| 25 | 2.240 ± 0.006 | −0.006 |
| 30 | 2.240 ± 0.003 | −0.006 |

and over 1000Å in length. A digital image analysis of the TEM micrographs for the 20, 25 and 30 mTorr films revealed a void volume fraction of approximately 12%, 17%, and 23%, respectively, with an uncertainty of ± 5%. These numbers, which give a rough estimate of the voided area, fall between the porosity results obtained by spectroscopic ellipsometry for the 2D and 3D models. Hence, the film anisotropy probably lies somewhere between the 2D and 3D case.

Next, SEM micrographs of the surface and fracture cross-sections of the 2500-3100Å films are shown in Figs. 6.8 and 6.9, respectively. At 60K magnification, no surface features were resolved on the film prepared at 5 mTorr. For the 10 and 15 mTorr films, shown in Figs. 6.8(a) and 6.8(b) respectively, some surface structure on the order of 300Å is visible but no crevices or voided areas are seen. However by 20 mTorr a network of voids is clearly seen in Fig. 6.8(c) with major crevices extending 5000Å in length and 100Å in width. Faint void boundaries reveal individual grains on the order of 200 to 400Å in diameter. This in agreement with the TEM micrographs where a number of grains were separated by voids. As well the surface
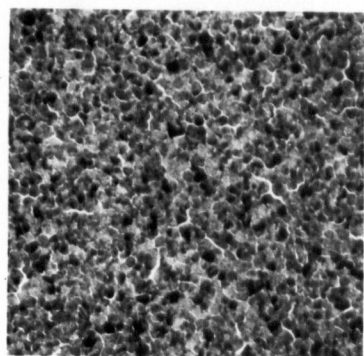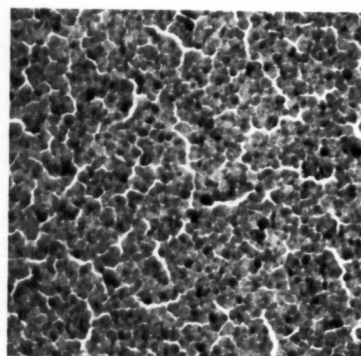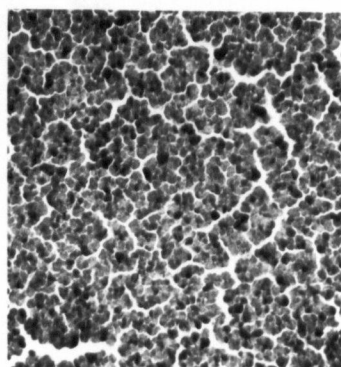
Figure 6.7. Transmission electron micrographs of thin Pd films (350Å) for increasing argon pressure: (a) 5 mTorr, (b) 15 mTorr, (c) 20 mTorr, (d) 25 mTorr and (e) 30 mTorr. All micrographs taken at the same magnification. All the micrograph markers correspond to 500Å.
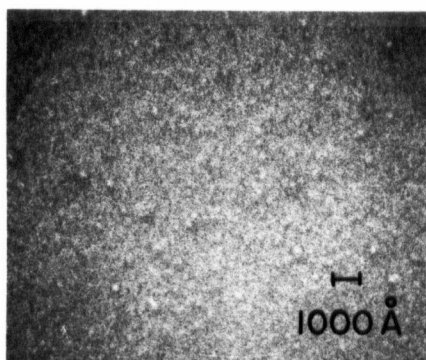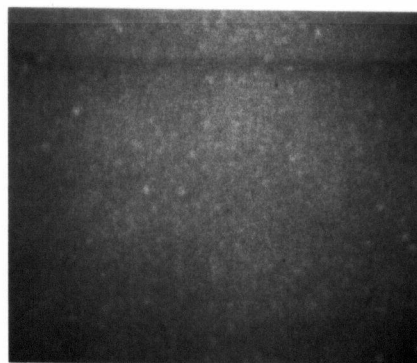
**(a)**     **(b)**
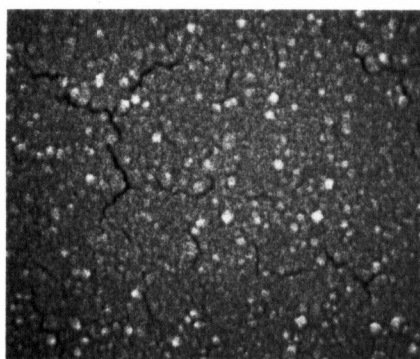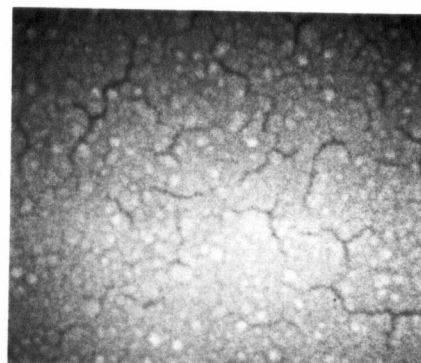
**(c)**     **(d)**
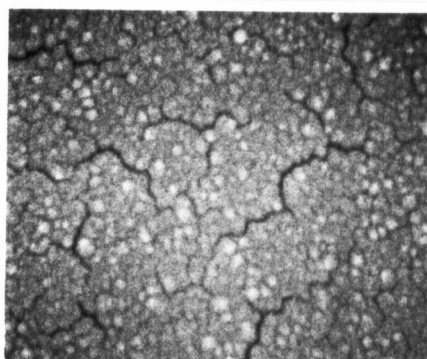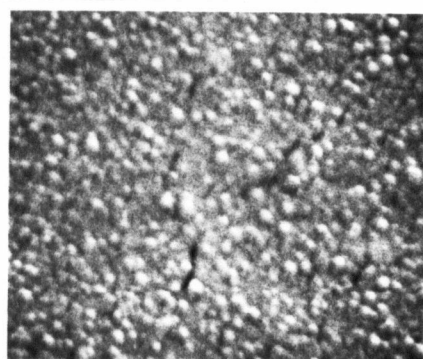
**(e)**     **(f)**

Figure 6.8. Scanning electron micrographs of 2500 – 3100Å Pd films deposited at various argon pressures : (a) 10 mTorr, (b) 15 mTorr, (c) 20 mTorr, (d) 25 mTorr, (e) 30 mTorr, and (f) 30 mTorr tilted 30°. All the micrograph markers correspond to 1000Å.
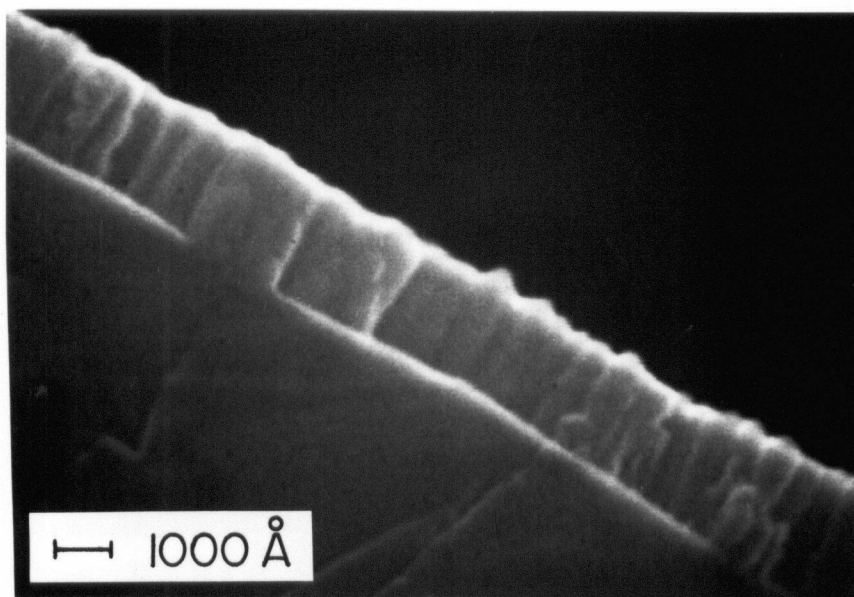
**(a)**
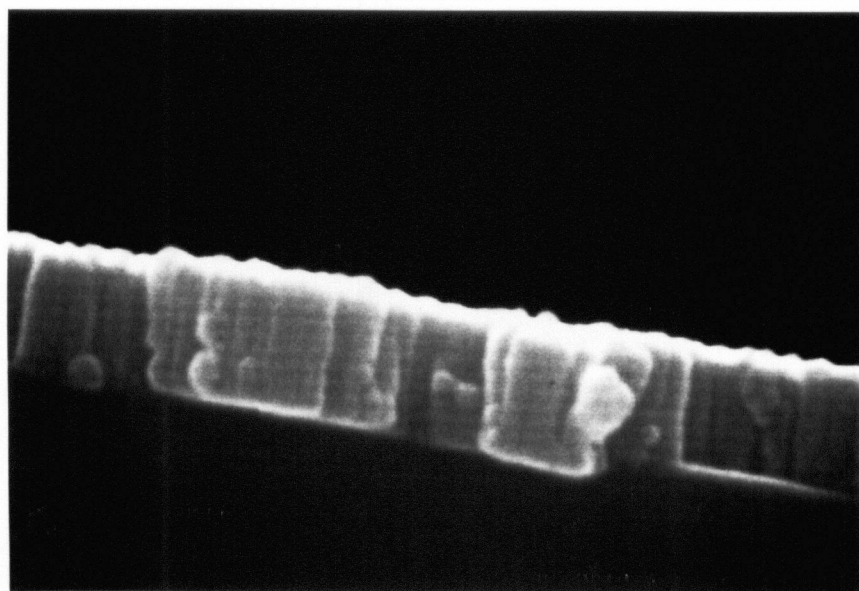


**(b)**

Figure 6.9. Scanning electron micrographs of fracture cross-sections of the Pd films for (a) 25 mTorr and (b) 30 mTorr.

structure evident at 10 mTorr, most likely corresponding to domed columnar tops rising above the surface, has become more prominent.

In Fig 6.8(d), the 25 mTorr surface is shown. The trend towards increased surface roughness and a larger void network continued, with the crevices becoming more connected throughout the film. Finally, a view of the 30 mTorr surface tilted at $0°$ and $30°$ is displayed in Figs. 6.8(e) and 6.8(f), respectively. Large crevices, $150\overset{\circ}{A}$ in width and $5000\overset{\circ}{A}$ in length extend throughout the film and most grains have voided–boundaries. From the $30°$ surface tilt micrograph, the roughness can be clearly identified as hemispherical columnar tops, $300\overset{\circ}{A}$ in diameter.

The Pd films were then fractured to view their cross–sections. For the low argon pressure films, the fracturing process did not produce good cross–sections, an indication in itself of structure of the films. In the 5 mTorr film, a columnar structure was visible, although poorly defined due to the tight packing of columns, with an average column diameter of approximately $300\overset{\circ}{A}$. The SEM fracture cross–section micrographs of the 25 and 30 mTorr films are displayed in Figs. 6.9(a) and (b), respectively. The grain clusters seen in the $350\overset{\circ}{A}$ Pd films are also prominent in the thicker films. The crevices evident from the surface micrographs are seen to extend throughout the film resulting in voided grain boundaries. In both films, individual columns with a mean diameter of around $400\overset{\circ}{A}$ are grouped together in clusters $1500\overset{\circ}{A}$ in diameter.

## 2. Discussion

The effective medium analysis of the spectroellipsometric data clearly indicates that the best description of the bulk region of the thin Pd films is provided by the SSC model, especially at the higher argon pressures. As stated previously, the basis for this

model is a random coated-particle microstructure in which the metal grains are optically isolated from each other. The transmission electron micrographs of the 350Å Pd films show that the crystallites are densely packed and to some extent overlap for films prepared at argon pressures at and below 15 mTorr. Hence one would expect the EMA theory, associated with a random aggregate microstructure, to be applicable in this pressure regime. While the 10 mTorr film data could be modelled with the EMA, an analysis of the 15 mTorr data based on a roughness/porosity model resulted in a negative thickness for the microroughness.

In the 20 mTorr film, a network of small crevices starts to develop throughout the Pd film, isolating the individual crystallites from each other. This grain separation increases with argon pressure until 30 mTorr, when most of the crystallites are surrounded by voids. Thus, the microstructure evident from TEM micrographs is consistent with assumption of optical isolation of the metal particles in the SSC theory. Furthermore the trend towards larger bulk porosity with higher argon pressure, obtained from the microstructural analysis of the spectroellipsometric data, was verified.

The scanning electron micrographs of the 3000Å films are remarkably similar to the TEM micrographs of the 350Å films. While the individual grains are more difficult to discern, the essential features evident in the TEM photos are confirmed. The same onset of crevices and subsequent void boundaries occurs at 20 mTorr and increases in magnitude with higher argon pressure. In addition the surface roughness barely evident at 10 mTorr now dominates the micrograph of the 30 mTorr film. Thus, even though the two sets of Pd films varied in thickness by an order of magnitude, the overall structure was similar as viewed by electron microscopy.

If one compares the TEM micrograph for the 30 mTorr Pd film, Fig. 6.7(e), with that obtained by Aspnes and Craighead [96] for the evaporated Rh thin film

deposited by Arndt *et al.*[116] a close resemblance between the two films is seen. This similarity suggests that the "cracks" in the Rh film are actually crevices formed naturally during film deposition and are not an artifact of TEM preparation. As well, the changes in the dielectric function of both these films with respect to their more bulklike counterparts are nearly identical. The fact that both the Pd and Rh films, with the same voided-boundary structure, are best described by the SSC theory, further supports the concept of a random coated-particle microstructure.

Next, the observed changes in the microstructure for the Pd films as a function of argon pressure are related to those expected qualitatively from Thornton's structure zone model. At the low substrate temperatures of the Pd films deposited in this study, $T/T_m = 0.2$, the microstructure for low argon pressures should correspond to a zone T region. Furthermore, increasing the argon pressure should result in a zone T/zone 1 transition.

Hoffman and Thornton's observations on the effect of argon pressure upon film microstructure formation have identified the transition pressure, where the intrinsic stress changes from compressive to tensile, with the zone T/zone 1 transition. This is supported from the XRD analysis which indicates a maximum compressive stress in the films at 15 mTorr. The compressive stress confirms that the energy flux reaching the surface is modifying the film structure. The film microstructure, as determined from the electron micrographs, appears to be relatively unaffected up to this argon partial pressure. The spectroellipsometric data indicates however that the surface roughness is already gradually increasing along with a decrease in the density of the bulk region of the film. At 20 mTorr, the point where the XRD indicates a large drop in the internal stress of the film, a network of crevices are now observed. The decrease in the compressive stress is the result of the reduced energy flux reaching the substrate

and it not due to a tearing of the film. The voids seen in the films are the result of fewer grains coming into contact with each other during film growth. This in turn is a consequence of the oblique incident angle of the deposition flux enhancing the effects of atomic shadowing to the extent that the grains formed about nucleation sites remain isolated from each other.[71] While the stress appears to remain constant for higher argon pressures, the size of the voided areas throughout the films increase in magnitude. Since the same microstructure was seen in the Rh film prepared by Arndt et al.[116] it appears that during evaporation of the Rh film, a significant component of the deposition flux must have had an oblique angle of incidence.

Thus, the zone T region can be identified from the electron micrographs as corresponding to a densely packed structure, with a relatively featureless surface, as expected. The transition to a zone 1 type structure with well-defined voided boundaries is a result of grain separation caused by the oblique deposition flux angle and reduced energy flux to the film substrate. Clusters of columnar grains then form the next level of the columnar structure in the film, which typifies zone 1 regions.[71] This supports the theory[70] that the zone 1 region is an intrinsic zone T structure with a columnar structure superimposed upon it. The grain clusters themselves probably arise out of regions where the original substrate was relatively smooth so that all the grains in a particular cluster were of the same height preventing wider crevices from forming between them.

Examining the Pd pseudodielectric data directly in Fig. 6.4, one sees that for argon pressures of 15 mTorr and higher, $<\epsilon_2>$ remains approximately constant while $<\epsilon_1>$ decreases appreciably in magnitude. It is also in this pressure range that the SSC theory becomes critical in interpreting the data as the grains become optically isolated from each other. As a result, one is able to optically identify from the

pseudodielectric function data alone the pressure at which the zone T/zone 1 transition occurs.

From the scanning electron micrographs the surface roughness appears to increase significantly for argon pressures above $P_t$ and this can be explained as follows. At low argon pressures the energy flux reaching the substrate is sufficient to minimize differences in grain heights, thus reducing the overall film microroughness. At higher argon pressures however, the energy flux arriving at the surface is reduced while the oblique component of the deposition flux has increased so that the surface begins to gradually become rougher. Above the transition pressure, the grain columns start to become isolated from each other during growth, further limiting the diffusion of adatoms across grain boundaries. This promotes further roughness which in turn enhances the atomic shadowing process, leading to wider voided boundaries and so on. However, the analysis of the spectroellipsometric data indicated that the rms microroughness, which is an optical average of the roughness over the beam area of $\simeq$ 1mm$^2$, remained essentially constant around 50Å for argon pressures greater than 15 mTorr for the 3D model. For the 2D model, the rms microroughness did increase slightly from 54Å to 78Å. Thus it appears that the roughness evident in the electron micrographs does not contribute significantly to the rms microroughness as determined by the spectroellipsometry analysis.

In the optical microstructural analysis, the surface microroughness layer was better described using an effective medium theory other than the SSC employed to model the bulk of the film. In particular, the fit based on $<\epsilon_1>$ alone using the HB theory is excellent, while the best overall description was provided by the EMA with equal palladium and void volume fractions in the surface layer. Therefore, on the basis of the above fits, it appears that the microstructures of the surface and bulk

regions are sufficiently different to require different effective medium theories. The values obtained for the microroughness and porosity of the films were dependent on whether a 2D or 3D microstructure was assumed in the analysis. While both fits were equally good, the 2D results are probably more realistic due to the columnar nature of the films.

In conclusion, the film microstructure determined by spectroellipsometry is in good agreement with that evident from electron microscopy. The films with increasing argon pressure went through a zone T/zone 1 transition around $P_t \simeq 15$ mTorr. The increase in roughness and porosity of the Pd films with higher argon pressures, determined by a microstructural analysis of the optical data, was also seen in the electron micrographs. Furthermore, the Pd films where the the grains were isolated to a certain extent from one another, were best described optically by a random coated-particle microstructure using the SSC theory.

## E. RF-INDUCED BIAS SPUTTERING

### 1. Results

Palladium films were biased sputtered on both the 2 and 5 cm substrates holders while varying the rf input power from 0 to 300 W. The rf powers and the subsequent rf-induced bias voltages used during film deposition are shown in Table 6.7, as measured at the matching network. The actual power density at the film substrate will be lower than the theoretical power density due to rf power losses between the matching network and the film substrate. The high dc bias voltages, $V_{bias}$, are due to the small area, 200 cm$^2$, of the substrate holder leading to a high impedance between the holder and plasma. To ensure that the dc bias measured at

Table 6.7. RF power and bias voltage ($V_{bias}$) on the substrate holder during deposition of the Pd films as measured at the matching network box. The measured resputtering rates (R) along with the sputtering yields (S) for Pd were used to estimate the ion current ($J_{ion}$) and power ($P_{ion}$) densities, and the sheath voltage, $V_s$.

| rf power (W) | $V_{bias}$ (V) | S (atoms/ion) | R (Å/sec) | $J_{ion}$ (mA/cm$^2$) | $V_s$ (V) | $P_{ion}$ (mW/cm$^2$) |
|---|---|---|---|---|---|---|
| 50 | −550 | 2.4 | 2 | .09 | −580 | 50 |
| 125 | −850 | 2.9 | 4.5 | .17 | −885 | 145 |
| 175 | −975 | 3.1 | 6 | .21 | −1020 | 205 |
| 250 | −1225 | 3.3 | 9 | .29 | −1260 | 360 |
| 300 | −1375 | 3.5 | 11 | .34 | −1400 | 470 |

the matching network was the same generated on the insulating substrate, the resputtering rate of Pd films deposited on conducting and insulating substrates was measured. The resputtering rate was found to be the same in both cases, so the true dc bias on the film substrate is close to that measured on the matching network.

The surfaces of the films prepared with negative substrate biases below 850 V were highly reflecting. However, above this dc bias voltage the film surfaces took on a slightly "milky" appearance, especially near the substrate edges, indicating the films were macroscopically rough and causing light scattering. This macroscopic surface roughness of the films was reduced in the areas wherever the silver paint on the substrate holder formed an interface with the film substrate.

The pseudodielectric function data, $<\epsilon>$, of the Pd films prepared at different substrate biasing are shown in Fig. 6.10. The measurements were made at the center of the films, and the reproducibility of the films was checked as well. The magnitude of $<\epsilon>$ decreased monotonically with increasing substrate bias, indicating that the
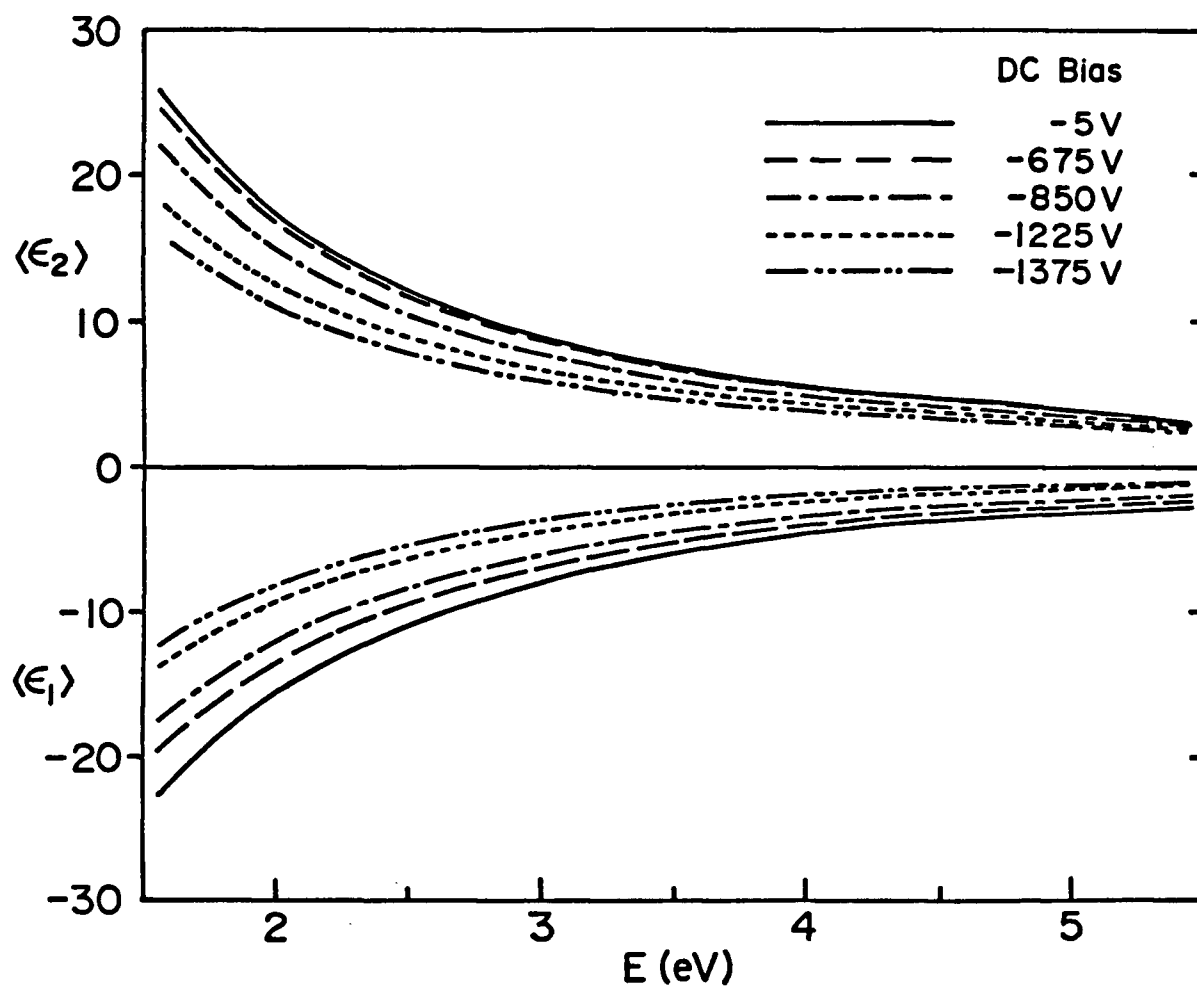
Figure 6.10. The pseudodielectric function, $<\epsilon> = <\epsilon_1> + i<\epsilon_2>$, data of the Pd films prepared as a function of rf-induced substrate biasing. The decreasing magnitude of $<\epsilon>$ with higher bias voltages, is due to the increased surface microroughness and porosity of the films.

surface microroughness and/or porosity of the films were increasing. There was no significant difference in the $<\epsilon>$ data for the Pd films prepared on either the 2 or 5 cm substrate holders.

In the microstructural analysis of the spectroellipsometric data, the reference Pd data was taken from the Pd film deposited with no applied substrate bias. Consequently, all the following best-fit parameters are determined with respect to that unbiased film. To model film porosity, the void volume fraction in the bulk region of the film was allowed to vary while surface microroughness was incorporated into the model using an overlayer consisting of equal volume fractions of Pd and voids and allowing the overlayer thickness to vary.[81]

To determine how the Pd film microstructure was affected by the biasing, several models were examined to see which provided the best description of the films. First, the 3-dimensional isotropic Bruggeman EMA which describes a random aggregate microstructure, was used assuming both porosity and microroughness in the Pd films. However, the analysis using the EMA resulted in negative thicknesses for the microroughness layer or else the fits were relatively poor. Therefore the EMA theory was rejected and the SSC theory was next used in the modelling. The best-fit parameters for the 2-parameter SSC microroughness/porosity model along with their 90% confidence limits and unbiased estimators are shown in Table 6.8 assuming 3D and 2D isotropic films. For the films deposited at the higher bias potentials, the unbiased estimator for the 2D model is lower by nearly a factor of 2 compared to the 3D model. As well, the uncertainties in the best-fit parameters are also smaller by a factor of 3 for the 2D model. Therefore, overall the films appear to be best characterized by a 2-dimensional isotropy which is supported by the columnar structure of the Pd films. It is interesting to note that while going from the 3D to the 2D

Table 6.8. Film models incorporating both porosity in the bulk region of the film and surface microroughness. The best-fit parameters, 90% confidence limits and unbiased estimator are shown for the 3- and 2-dimensional isotropic SSC effective medium theories.

| Model | Bias (-V) | Surface Microroughness d, $f_{pd} = 50\%$ | Bulk Region $f_{pd}$ | Unbiased Estimator $\hat{\delta}$ |
|-------|-----------|-------------------------------------------|----------------------|-----------------------------------|
| 3D    | 550       | $- - - -$                                 | 97.5 ± 0.4%          | .003                              |
|       | 675       | 3 ± 2Å                                     | 97 ± 1%              | .003                              |
|       | 850       | 20 ± 5Å                                    | 97 ± 2%              | .006                              |
|       | 975       | 39 ± 10Å                                   | 96 ± 3%              | .012                              |
|       | 1225      | 44 ± 17Å                                   | 94 ± 5%              | .016                              |
|       | 1375      | 67 ± 18Å                                   | 94 ± 5%              | .019                              |
| 2D    | 550       | 3 ± 1Å                                     | 98.8 ± 0.3%          | .003                              |
|       | 675       | 6 ± 1.5Å                                   | 98.4 ± 0.3%          | .003                              |
|       | 850       | 20 ± 2Å                                    | 97.9 ± 0.4%          | .004                              |
|       | 975       | 38 ± 3Å                                    | 96.8 ± 0.7%          | .006                              |
|       | 1225      | 43 ± 6Å                                    | 95.6 ± 1.3%          | .010                              |
|       | 1375      | 61 ± 6Å                                    | 94.8 ± 1.4%          | .011                              |

model, the rms microroughness values did not change significantly while the porosity values decreased by only $\simeq$ 1%. As the substrate biasing was increased, the rms microroughness increased as well, reaching 61 ± 6 Å for a -1375 V dc bias. These results are consistent with the macroscopic roughness evident from the light scattering off the films prepared at the higher rf powers. In addition, the Pd volume fraction decreased slightly with respect to the unbiased films. Further attempts to improve the fits such as adding oxide or contamination overlayers were unsuccessful.

Measurements on the "milky" regions of the Pd film surfaces showed a slight decrease in the magnitude of the pseudodielectric function data as seen in Fig. 6.11

for the $-1375$ V biased film. Analysis of the data indicated that the rms surface microroughness increased, as expected, to $75 \pm 4$ Å compared to $61 \pm 6$ Å obtained for the highly reflecting region.

Next, the dc deposition, bias deposition and resputtering rates for the Pd films prepared on the 2 and 5 cm substrate holders were measured. The geometry of the substrate holders can directly influence the contamination and uniformity of the films through the electric field and, consequently, the ion bombardment across the film substrate. The rates were calculated from the film thicknesses, measured with a Tencor stylus profilometer, based on the assumption that the film density did not change significantly, which was verified by the spectroellipsometric data.

The bias deposition rate of the Pd films prepared on the 2 cm holder was found to be very nonuniform across the film substrate. With no substrate biasing, the Pd film was uniform across the substrate with a thickness of $3900 \pm 100$ Å. Biasing the substrate at $-1375$ V, however, changed the thickness profile dramatically as the film thickness at the center decreased to 3300 Å, while only 500 Å of Pd film remained at the edge of the film substrate. Hence, most of the resputtering was concentrated around the circular edge of the film. The resputtering was studied separately by applying an bias of $-1375$ V for time intervals ranging from 0 to 3 minutes for a series of Pd films. The thickness profiles of these films are shown in Table 6.9 and the average dc and bias deposition rates along with the resputtering rates are given in Table 6.10. The Pd films were resputtered nonuniformly from the edge inwards towards the center of the film and the average resputtering rate across the film substrate varied from 11 Å/sec at the center to 27 Å/sec at the edge. From these resputtering rates, and the measured dc deposition rate, the expected deposition rate for bias sputtering at $-1375$ V was calculated. A comparison between the
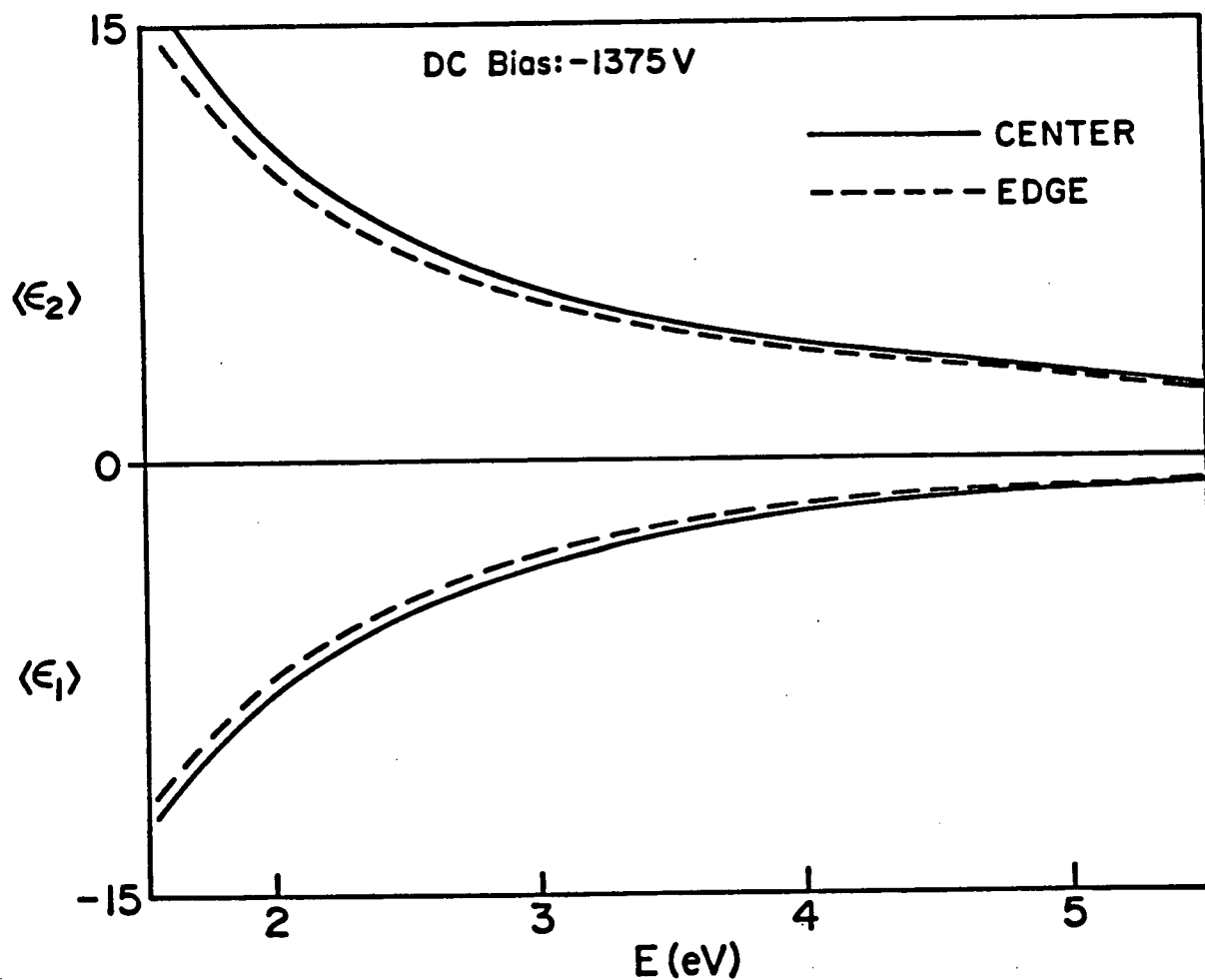
Figure 6.11. The pseudodielectric function data for the −1375 V biased Pd film measured at the center and edge of the film where the surface had a highly reflective and "milky" appearance, respectively.

Table 6.9. Spatial thickness profile, in Å, of Pd films biased at −1375 V for different time intervals on the 2 cm substrate holder.

| Biasing Time | Distance from centre of film (mm) | | | | |
|---|---|---|---|---|---|
| (minutes) | 0 | 3 | 6 | 9 | 11 |
| 0 | 2910 | 2850 | 2960 | 2950 | 2950 |
| 1.0 | 2450 | 2310 | 2240 | 2100 | 1600 |
| 1.5 | 1900 | 1725 | 1550 | 1200 | 500 |
| 3.0 | 950 | 650 | 150 | 0 | 0 |

calculated and measured average deposition rates (Table 6.10) indicate that the measured rate is higher than that expected. Thus, there appears to be an enhancement in the Pd deposition rate during biasing which partially offsets the resputtering rate.

The bias deposition and resputtering rates across the film substrate attached to the 5 cm holder were, in contrast to the smaller holder, fairly uniform. As seen in Table 6.10, the resputtering rate varied from 12 Å/sec at the center to 14 Å/sec at the edge of the film substrate. Again, the measured bias deposition rates were significantly higher than that expected based on the measured resputtering rates. This enhancement will be discussed more fully in the next section.

To determine the ion current and power density at the film substrate, the resputtering rate was measured at the center of the Pd films prepared on the 5 cm holder for different substrate biasing. The resputtering rate increased linearly with the rf input power, with an increase of 1 Å/sec for every additional 25W of rf power, as shown in Table 6.7.

The sheath thickness between the plasma and the center of the substrate holder

Table 6.10. Rates in Å/sec measured a distance, d, from the center of the Pd films. The average deposition rates, ± 1Å/sec, are shown for the films prepared on the two substrate holders, for dc and bias sputtering (bias = −1375 V). Also shown are the measured resputtering rates and the expected bias sputtering deposition rates for the −1375 V biased film.

| Substrate Holder | d (mm) | dc Deposition | Resputtering | Bias Deposition (expected) | Bias Deposition (measured) |
|---|---|---|---|---|---|
| 2 cm | 0 | 32 | 11 | 21 | 28 |
| | 6 | 32 | 16 | 16 | 25 |
| | 11 | 32 | 27 | 5 | 4 |
| 5 cm | 0 | 30 | 12 | 18 | 27 |
| | 6 | 30 | 13 | 17 | 27 |
| | 11 | 29 | 14 | 15 | 25 |

remained constant at 15 ± 1mm as the bias voltage was varied from −550 to −1375 V. To study the dark space region in more detail, a 5cm x 5cm square glass substrate was attached to the 2 cm substrate holder. With the glass substrate biased, the dark space thickness was 15mm above the center of the film substrate, but decreased to 1mm close to the edges of the substrate. After depositing a Pd film on the surface, the dark space was nearly uniform at 15 mm over the entire substrate. Hence, the insulating substrate does not couple very well to the rf and the bias voltage drops close to the floating potential approaching the edge of the substrate. As before, the Pd film was resputtered off this larger insulating substrate from the edge inwards towards the center.

## 2. Discussion

Characterization of the Pd thin films prepared at low substrate temperatures and with argon pressures lower than 15 m Torr showed that they could be characterized by a zone T structure[71] consisting of densely packed, poorly-defined fibrous grains. Similarly, the Pd films deposited at low bias potentials are characterized by a zone T structure as well. From the spectroellipsometric data, the surface microroughness increased with higher substrate biasing, accompanied by a slight decrease in the palladium volume fraction in the bulk region of the film. This would correspond to the Pd film undergoing a gradual transition to a zone 2 structure, similar to that observed for an increase in the substrate temperature of the Pd films. As well, the Pd films were best described by the 2-dimensionally isotropic SSC theory, implying that the grains are optically isolated from each other, which is consistent with the voided-boundary columnar structure in the zone T/zone 2 transition region.

The variation of surface roughness with the rf-induced substrate biasing has also been observed by Vossen[120] for platinum and aluminum films deposited by dc diode sputtering. In particular, the surface roughness of the Al films was minimized at a certain bias potential and then increased with higher biasing. For the Pd films prepared by dc diode sputtering[120] the optimum bias voltage was around −75 V; however, in this study no such optimum voltage was observed. For dc magnetron sputtering, the energetic flux of reflected neutrals from the target[71] that reaches the film substrate may be substantially greater than in dc diode sputtering due, in part, to the lower operating pressures. Therefore, additional ion bombardment appears unnecessary for Pd films as the ion bombardment already present in dc magnetron sputtering is sufficient to produce the most dense films with the smoothest surfaces. This is supported by scanning electron micrographs of the unbiased Pd films, where no

surface features could be resolved at 60K magnification.

The surface microroughness and the overall film porosity of the Pd films increased with higher substrate deposition temperatures, reaching an rms microroughness of $80 \pm 3$ Å by $200^{\circ}$ C. Hence, biasing the film substrate from $-5$ to $-1375$ V modified the Pd film microstructure similar to that seen by raising the substrate temperature from $22^{\circ}$ C to $200^{\circ}$ C. However, the Pd films prepared at different substrate temperatures all had highly reflecting surfaces, while those prepared with bias potentials greater than $-850$ V all had macroscopically (i.e., light scattering) rough surfaces. The macroscopic roughness is attributable to the ion bombardment therefore, and not to the increased substrate temperature. This is agreement with the observation by Dixit and Vook[122] that the surface microroughness of Pd films increased after ion bombardment. Ellipsometrically, the macroscopically rough surfaces have a slightly larger rms surface microroughness compared to the more highly reflecting surfaces. The rms surface roughness value did not increase significantly, however, due to the relative insensitivity of ellipsometry with respect to features $\geq 1000$ Å which cause light scattering.[28]

Film contamination can affect the nucleation and growth of the thin films, and lead to rougher surfaces. The film substrate is less exposed to possible contamination from the 2 cm holder compared to the 5 cm holder, however, from the spectroellipsometric data, which is sensitive to the surface microroughness, no difference was seen in the films whether prepared on the small or larger holders. Hence, the increased roughness is probably not a result of any film contamination. Actually, with the high resputtering rates seen in this study, the contamination of the films from either of the substrate holders is unlikely. Vossen et al.[119] showed that contamination becomes likely only when the backscattering rate of the contaminant atoms is greater

than their resputtering rate. Furthermore, the substrate holders themselves are soon covered by the coating material, so the majority of the resputtered atoms are Pd. In any case, Pd with its low reactivity will not be affected as much by contamination in terms of surface roughness as are more reactive metals such as aluminum.

The ion current and power densities arising from the substrate biasing can be estimated from the measured resputtering rates and the sputtering yields for Pd. The resputtering rate, R, is given by,[108]

$$R = 62.3 \, J \, S \, M_{Pd}/\rho \quad \overset{\circ}{A}/min, \tag{2}$$

where J is the ion current density in mA/cm$^2$, and S, $\rho$, and M$_{Pd}$ are the sputtering yield,[123,124] density (gm/cm$^3$) and atomic weight of Pd, respectively. As seen in Table 6.7, the ion current density varied from 0.09 to 0.34 mA/cm$^2$ corresponding to a flux of 6x10$^{14}$ to 2x10$^{15}$ ions/cm$^2$ sec, respectively. Assuming a space charge limited current across the substrate–plasma sheath, the sheath voltage can be estimated from a modified Child–Langmuir law for a rf discharge.[125] The uncertainties in the resputtering rates, ±1 $\overset{\circ}{A}$/sec, and the sheath thickness, ±1mm, result in an uncertainty of the sheath voltage of ±200V. The estimated sheath voltages shown in Table 6.7 are in good agreement with the measured dc bias voltages. This is actually somewhat surprising considering charge–exchange collisions and rf modulation have been ignored.[67] Finally, the power densities due to the ion current flux have been calculated, and they represent about 25% of the maximum possible power density.

The nonuniformity in the resputtering of the Pd film around the film substrate edges is expected due to the high electric fields around sharp corners or edges.[129] The ion current densities are higher around the edges therefore, leading to higher resputtering rates in those regions as compared to plane surfaces.[126] As well, the ion

flux around the substrate edge is directed towards the film surface at an oblique angle of incidence, affecting the sputtering yield. From these arguments, the Pd deposition during biasing is expected to be fairly uniform for films prepared on the larger holder and considerably less so on the smaller holder.

From Table 6.10, the resputtering rate for the film prepared on the 5 cm holder is nearly uniform within 10% across the film surface. In contrast, the resputtering rate for the film prepared on the 2 cm holder is nearly a factor of 2.5 higher at the edge of the substrate compared to the center region. One might expect that away from the insulating substrate holder edges, that the resputtering rates would be fairly uniform. However, a preferential resputtering of the Pd films from the edges inwards was observed until the films were completely resputtered away. Therefore the rf-induced dc bias voltage is established only on the Pd film itself and not on the insulating substrate, except over the center region. This is supported by the dark space thickness decreasing from 15mm to about 1mm near the edge of the insulating substrate as the Pd film is resputtered away. Hence, for a dc bias to be fully established on an insulating substrate, the rf electrode should be in direct contact with the insulated substrate over its full area.

As seen in Table 6.10, the measured Pd bias deposition rate was higher than expected on the basis on the measured resputtering rate, except near the edge of the film substrate for the 2 cm holder. Hence, some enhancement in the deposition rate must occur to partially offset the resputtering. Vossen and O'Neill[118] noted that for dc sputtering at a constant dc voltage, the dc current increased linearly with the substrate biasing due to an enhancement of the plasma ionization. The higher dc power led to an increased deposition rate until the resputtering rate became significant. This was also observed by Cuomo et al.[127] who also attributed the increase in the deposition rate to

an increase in ion density. In this study however, the dc sputtering was controlled by a constant dc current of 1.0 amp. Applying a rf bias of $-1375$ V, the dc target voltage dropped, as expected, from $-375$V to $-355$V resulting in a 5% decrease in the dc power. Hence, from this argument, the slight decrease in the dc power with rf–induced biasing would be expected to further decrease the overall deposition rate and not enhance it. To test that the overall flux from the target did not increase, another film substrate on a grounded holder was placed alongside the biased holder. The deposition rate for the film on the grounded substrate holder did not change while substrate biasing the other film. Therefore, another mechanism must be responsible for increasing the overall Pd flux reaching and staying at the film substrate.

Locally around the negatively biased substrate, an ion–assisted deposition process may be responsible for the deposition enhancement by capturing Pd ions which would have normally bypassed an unbiased substrate. Additionally, the increase in deposition energies of the Pd ions may lead to a greater sticking probability. However, it is uncertain whether the number of Pd ions in the plasma is enough to nearly offset the resputtering rate. Bland *et al.* [128] reported seeing a factor of 2 increase in the deposition rate for vacuum–evaporated chromium after biasing the substrate, for a ion current density of 0.1 mA/cm$^2$. As well, Vossen and O'Neill [126] noted an increase in deposition, attributable to Al ions, around the edge of film substrate. Alternatively, the argon ion bombardment, while responsible for the resputtering, may also be increasing the sticking probability of the Pd atoms reaching the substrate.

## 3. Summary

The pseudodielectric function of palladium films deposited by dc planar magnetron sputtering while biasing the film substrate, was measured by spectroscopic ellipsometry. The enhancement in the ion bombardment and the higher substrate temperatures associated with the rf—induced biasing led to an increased surface roughness of the films, while the overall Pd density decreased slightly. The changes in the Pd microstructure were similar to that produced by varying the substrate temperature alone. Due to the high resputtering rates varying from 2 to 11 Å/sec for bias voltages of −550 to −1375 V, contamination of the film from the substrate holders was not a problem. The nonuniformity in the resputtering of a Pd film off an insulating film substrate attached to a smaller diameter rf electrode could be attributed to electric field edge effects and the poor rf coupling into the insulating film substrate. Finally, it was observed that the deposition rate while rf substrate biasing was higher than that expected on the basis of the measured resputtering rate. Several mechanisms were proposed to account for the deposition rate enhancement.

## F. DIELECTRIC FUNCTION COMPARISON

Typically, the "best" film in terms of density and surface quality also displays the largest magnitude in the real and imaginary parts of the dielectric function. For dc planar magnetron sputtering, the best films have been consistently prepared at low argon partial pressures (≤ 5 mTorr) and at low substrate temperatures (295 K).

Over the last twenty years, a number of measurements on the optical properties of Pd thin films and bulk specimens have been reported. [130] − [140] However, the agreement between the measured values have not been very good. In Fig. 6.12 the dielectric function of Pd measured over the spectral range 1.5 −6.0 eV by various

authors is compared to the data obtained in this study. Perhaps the most salient feature of this graph is the wide variation in the reported results for $\epsilon_2$ while the $\epsilon_1$ values are in generally good agreement.

Since the sample preparation methods varied from group to group, it is not surprising that the microstructure, and hence, the optical properties vary also. The fact that the real and imaginary components do not scale together, however, indicates that the EMA cannot account for the observed changes in terms of bulk density alone. As for the SSC theory, nearly the opposite behaviour is expected with $\epsilon_2$ component remaining constant while the $\epsilon_1$ decreases magnitude depending upon the bulk porosity. Surface roughness, from previous experience with Pd films, tends to change $\epsilon_1$ in the same manner as bulk porosity, so the observed effect cannot be explained by a combination of surface microroughness and porosity acting in tandem. Indeed, any argument based on two competing effects exactly cancelling out any changes in the $\epsilon_1$ data would appear to be unlikely. Also, as will be seen, oxide layers are unlikely to resolve the observed behaviour because of the slow oxidation rate of Pd and the care taken to minimize the exposure of the films to air. Given that the data is accurate, one possible explanation for the data would be a grain boundary scattering mechanism which essentially scales up the $\epsilon_2$ component in magnitude, and leaving $\epsilon_1$ unchanged. Another explanation might be based on the fact that the contributions to the real and imaginary components of the dielectric function from the intraband (free–electron) and interband transitions are different.

The sample preparation methods used by the authors to deposit the Pd films, along with the optical measurement techniques, are shown in Table 6.11. Except for Weaver and Benbow [135] (WB), who examined a bulk Pd sample by calorimetric measurements at 4.2 K, the selected set of Pd data was determined by optical means
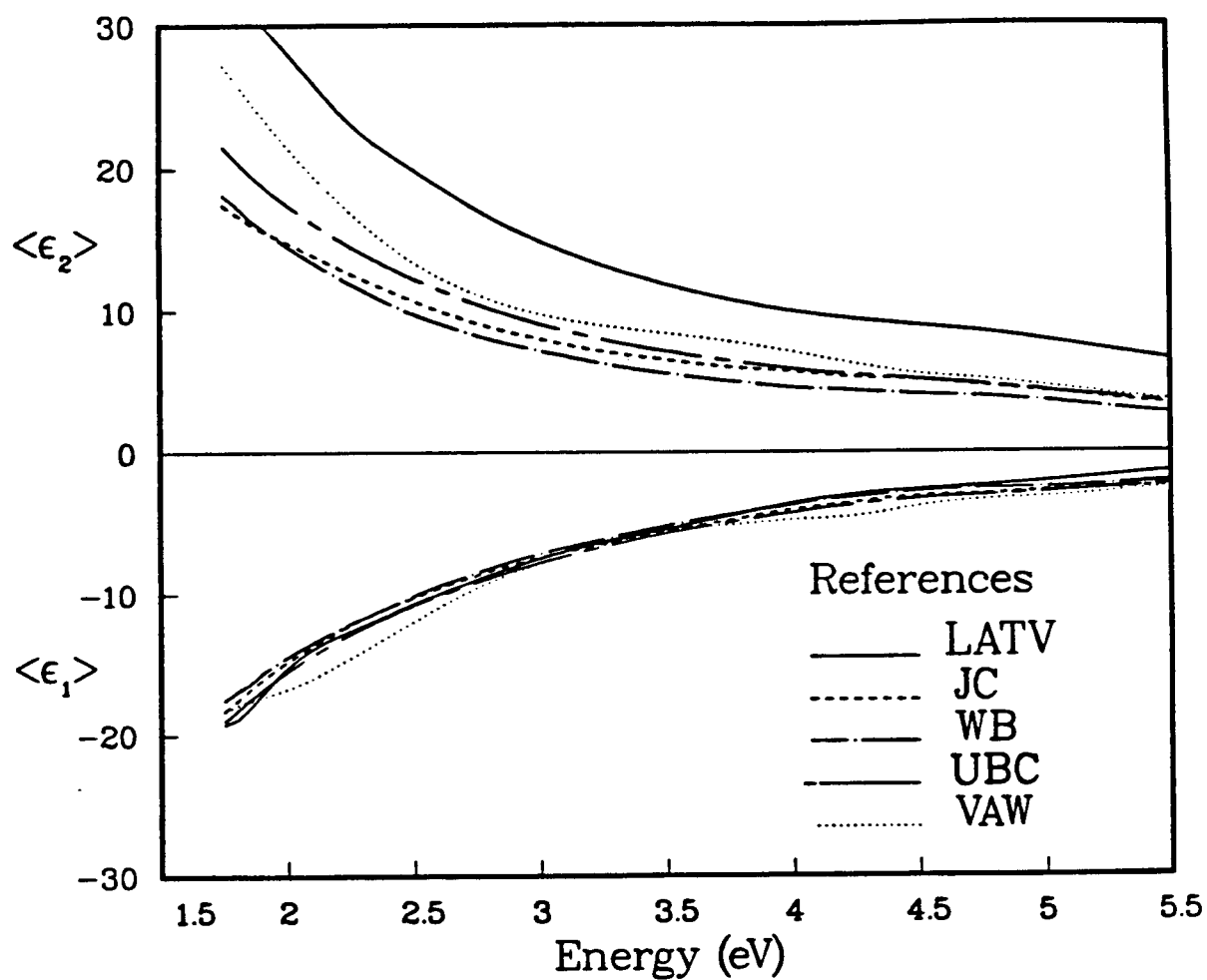
Figure 6.12. Comparison to previous measurements of the dielectric function of Pd reported in the literature. These data are discussed, along with the preparation conditions for each film, in the text.

Table 6.11. Sample preparation conditions and measurement techniques used by different authors in measuring the optical constants of Pd.

| Authors | Deposition (Torr) | Rate ($\mathring{A}$/sec) | Thickness | Annealed | Measurement |
|---|---|---|---|---|---|
| LATV | evaporated ($1 \times 10^{-8}$) | 60 | 320 $\mathring{A}$ | Yes | R,T (Air) |
| VAW | evaporated ($1 \times 10^{-8}$) | 150 | 2000 $\mathring{A}$ | No | R ($1 \times 10^{-8}$ Torr) |
| UBC | dc sputtered ($1 \times 10^{-6}$) | 25 | 3000 $\mathring{A}$ | No | UBC Ellip (Air) |
| JC | evaporated ($3 \times 10^{-6}$) | 50 | 375 $\mathring{A}$ | No | R,T ($N_2$) |
| MPR | rf sputtered ($1 \times 10^{-8}$) | 15 | 2000$\mathring{A}$ | No | UBC Ellip (Air) |
| WB | bulk | -- | --- | Yes | Calorimetric (4.2K) |

using thin films. Lafait, Abeles, Theye and Vuye[136,137] (LATV) and Johnson and Christy [133] (JC) both evaporated thin films around 350 $\mathring{A}$ in thickness and used reflectance and transmittance methods to measure the optical constants. Vehse, Arakawa, and Williams[131] (VAW) evaporated a film (approximately 2000 $\mathring{A}$ thick) and used reflectance methods and a Kramers–Kronig analysis to determine the dielectric function. In this study, three differently prepared samples were examined using the spectroellipsometer : 1) a dc planar magnetron sputtered film (UBC) (25 $\mathring{A}$/sec), 2) a dc planar magnetron sputtered film, deposited on a different system (JA) (7 $\mathring{A}$/sec), and 3) a rf–sputtered film from MicroTel Pacific Research (MPR).

To investigate if the differences in the dielectric data could be reconciled in terms of a simple microstructure involving bulk porosity, a Wiener bounds plot was constructed as shown in Fig. 6.13, using the Pd data from LATV at 3.0 eV and an void phase. The circular arc corresponds to the bounds determined by maximum
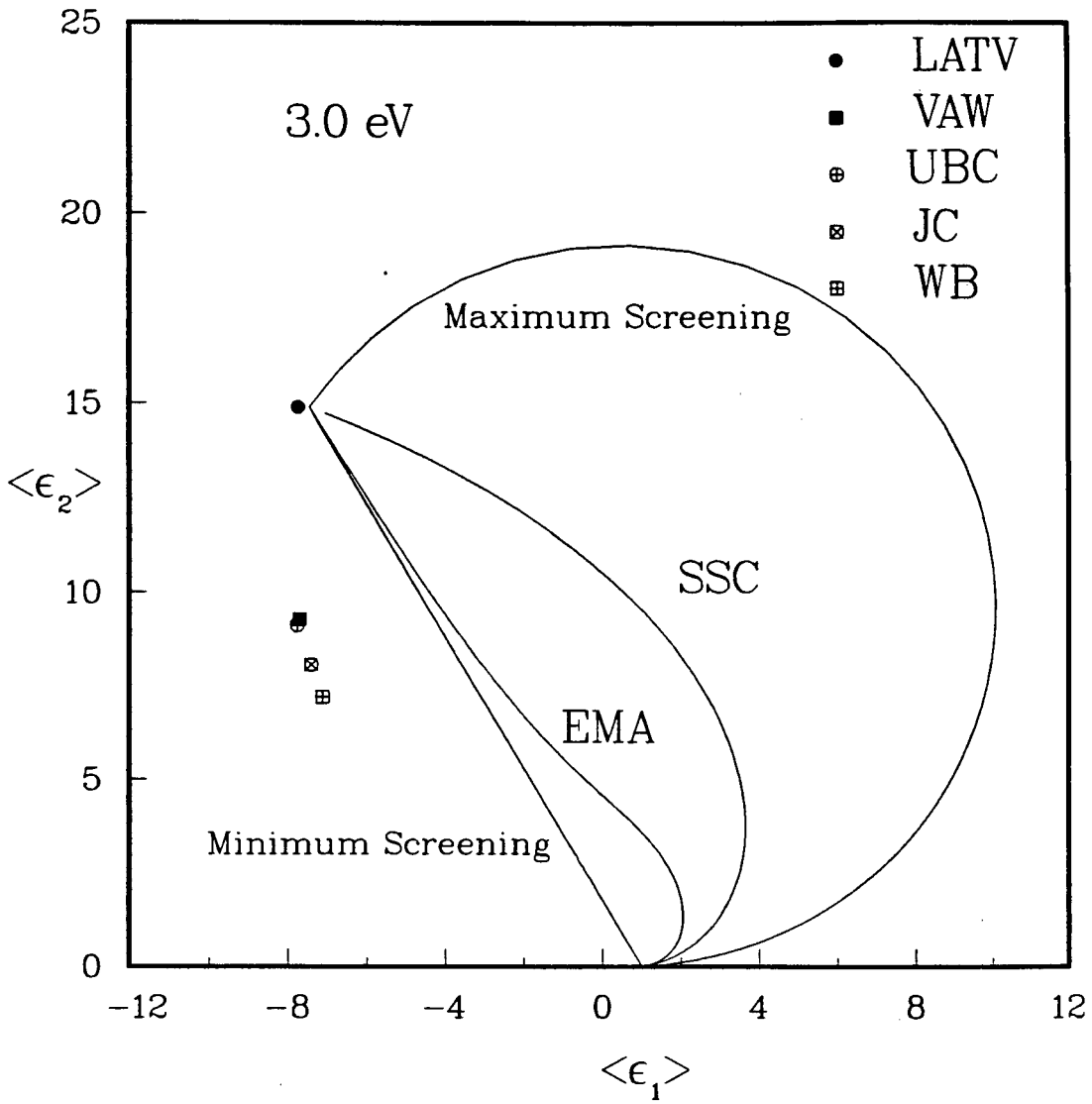
Figure 6.13. Wiener bounds on dielectric function at 2.5 eV assuming Pd and void phases. Pd phase taken from LAW data.

screening in the sample while the linear boundary follows assuming no screening in the sample. Also shown are the trajectories of the dielectric function as the Pd volume fraction is varied from 0 to 1 for the 3-dimensional EMA and SSC effective medium theories. The Pd data for 3.0 eV from the other authors is also shown and theses points are seen to lie outside the absolute Wiener bounds. Therefore, the difference in the dielectric spectra has to be explained by a different microstructure. An optical microstructural analysis using surface microroughness and bulk porosity was also unable to account for the observed differences.

Next, the possibility of an oxide or contamination overlayer affecting the measurements is addressed. A Pd film prepared by dc-sputtering was immediately measured on the spectroscopic ellipsometer after deposition. Three weeks later the same film was again measured, before and after a methanol rinse. The pseudodielectric data of these films with different overlayer thicknesses is shown in Fig. 6.14. The Pd film had a contamination overlayer thickness of $13.7 \pm 0.6$ Å prior to the methanol rinse, as determined by microstructural analysis involving the original film. After the methanol rinse, the overlayer thickness decreased to $4.5 \pm 0.5$ Å. The overlayer remaining after the rinse probably corresponds to a mixture of oxide or chemisorbed atoms while the 10 Å or so of material removed by the rinse was probably due to loosely bounded contaminants, i.e., hydrocarbons. Therefore after three weeks, roughly one monolayer of "oxide" accumulated onto the Pd film surface. Since the above investigations carried out by the different groups were either in ultra-high vacuum or immediately after deposition, one can discount the possibility of any significant oxide forming at room temperature during the deposition-measurement time interval.

Several Pd films deposited by other groups were also measured on the UBC spectroellipsometer. First, a film was prepared on a different dc planar magnetron

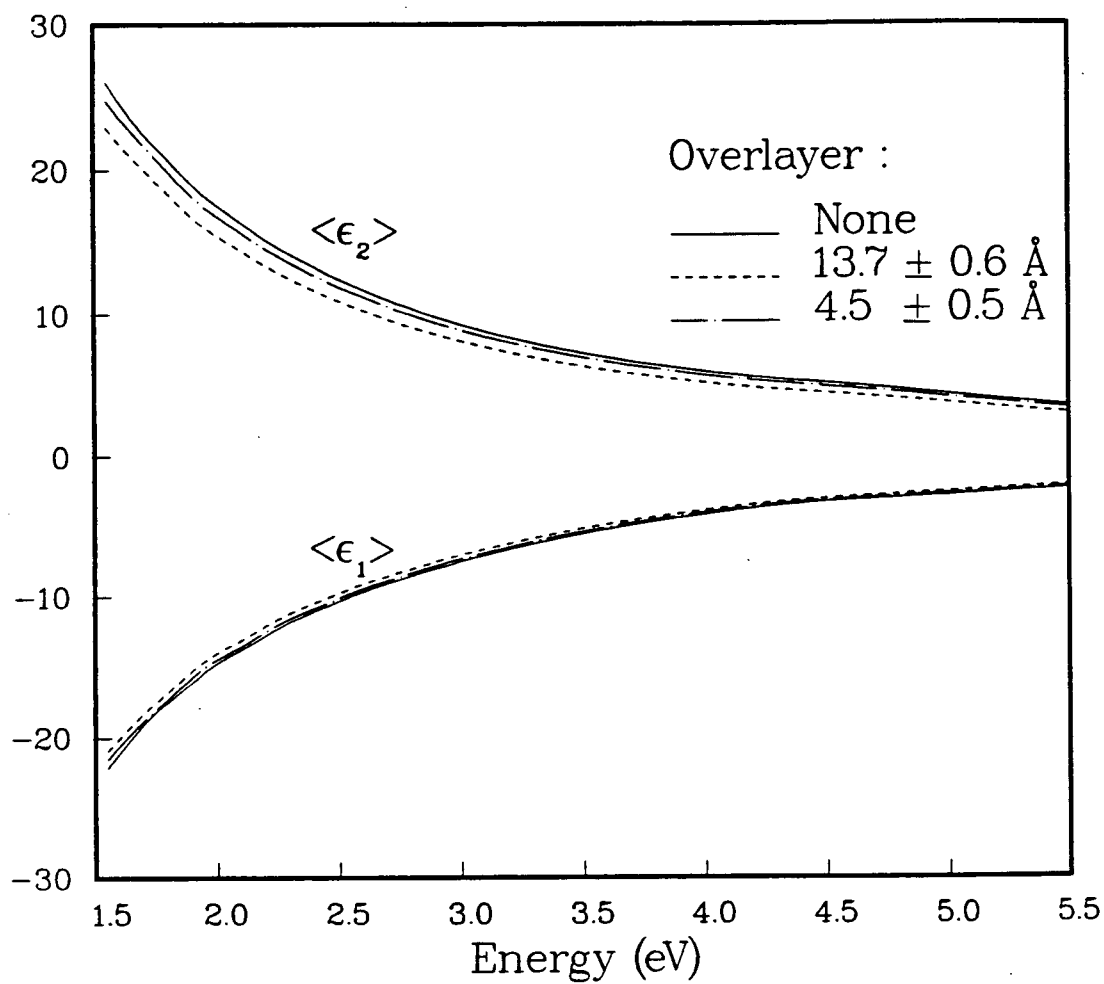Figure 6.14. Effect of contamination and oxide layers on Pd film. Pseudodielectric function of Pd immediately after deposition and three weeks later before and after a methanol rinse of surface.

system by J. Affinito, at an argon partial pressure of 2 mTorr and a deposition rate of 7 $\overset{\circ}{A}$/sec. As seen in Fig. 6.15a, the two sets of measurements are in very good agreement. This indicates that the deposition rate in dc planar magnetron sputtering does not play a significant role in determining the microstructure confirming an earlier study. This is in contrast to evaporation methods where low deposition rates were seen to cause increased surface roughness on the Pd films.[133] Next, a rf–sputtered film prepared in an argon pressure of 18 mTorr was examined several days after deposition. The dielectric function of this film compared to the dc sputtered films shows that the $\epsilon_2$ curve is scaled downwards with the $\epsilon_1$ curving remaining approximately the same.

To examine the role of contamination during deposition, a Pd film was deposited in air at a partial pressure of 5 mTorr (Fig. 6.15b). The surface quality of the film was visually quite good and the $\epsilon_2$ data matches the argon dc–sputtered films almost exactly while $\epsilon_1$ decreased in magnitude. It is therefore unlikely that contamination during sputtering could account for the scaling in the $\epsilon_2$ data. The films prepared by evaporation by the other groups was performed in high to ultrahigh vacuum, so contamination is not a likely source of the difference.

The mean free path of electrons in Pd is around 230 $\overset{\circ}{A}$.[142,143] Therefore if the grain size is smaller than the electron mean free path, grain boundary scattering becomes significant and can affect the measured optical properties.[144] In the optical regions where intraband transitions dominate, the free electron drude theory can be used to determine the change in the relaxation time and this can be related to the average grain size in the material. Electron microscopy can be used in conjunction with this technique to verify (or determine) the average grain size to see if the results are consistent. However, for Pd, interband transitions are also present so that the number
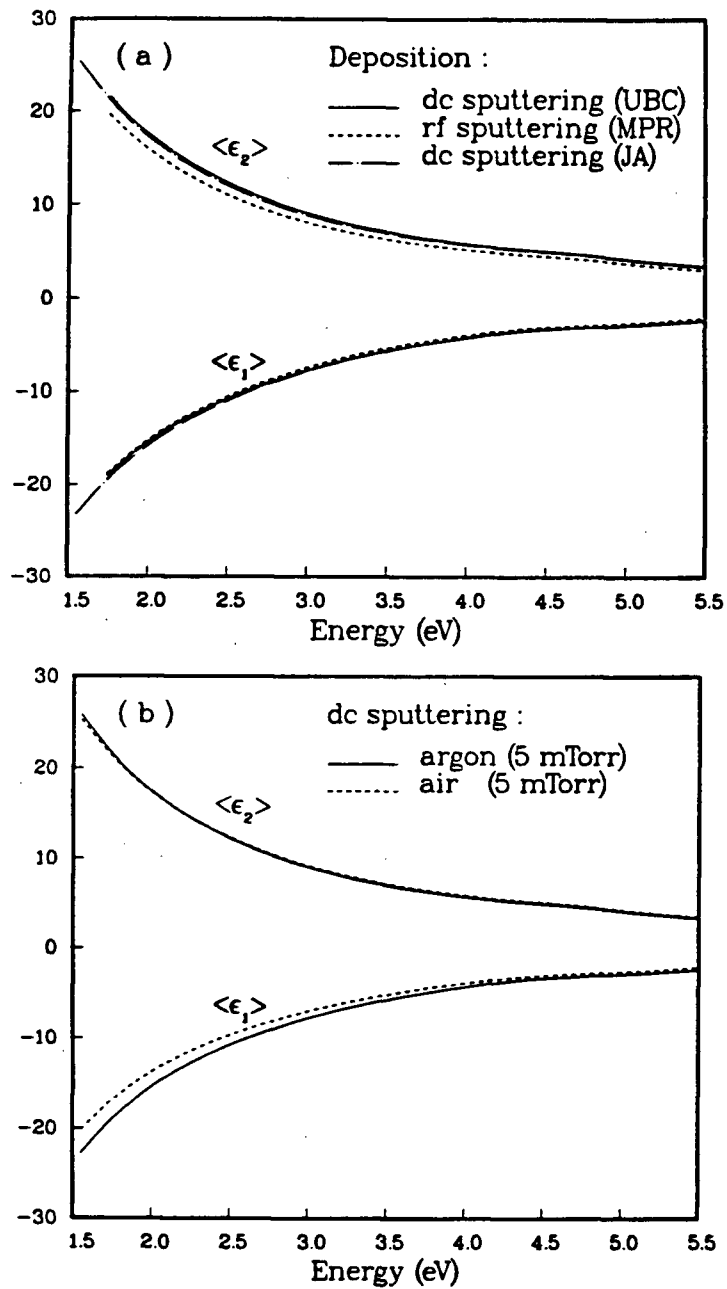
Figure 6.15. Pseudodielectric function $<\epsilon> = <\epsilon_1> + i<\epsilon_2>$ of palladium films deposited using different deposition techniques.

of phenomenological parameters increases to the extent that determination of the decreased relaxation time due to the grain boundary scattering becomes difficult. One can show qualitatively, however, that the effect of decreasing the relaxation time is to scale $\epsilon_2$ upwards in magnitude with little effect on $\epsilon_1$. The dielectric data from Fig. 6.12 does follow this behaviour to a large extent, however, it is difficult to relate this scaling to the actual microstructure. If grain boundary scattering is the cause of this scaling then it would appear that the data most affected by grain size effects is that of LATV. However, they annealed their films so one would expect grain size effects to be less important for their films than that prepared by other groups. They report that their 320 Å film [136] consisted of large crystals ($\simeq$3000 Å) embedded in smaller crystallites ($\simeq$300 Å), so that grain boundary scattering would not appear likely. While the small thickness of their film may play a role, the Pd film of Johnson and Christy was of approximately the same thickness and their results for $\epsilon_2$ disagreed almost by a factor of two!

To determine the actual reasons for the discrepancy in the optical constants of physical vapour deposited films will require a more extensive investigation. First the results measured for the evaporated Pd films should be reproduced if possible, in conjunction with other surface analysis techniques such as electron microscopy. As well, an error analysis of the optical techniques, used by the various groups to determine the dielectric function, should be made to see if some systematic error (such as in the thickness of the film) could significantly affect the imaginary component while leaving the real component unchanged. Finally, it should be pointed out that is unlikely that the films deposited by evaporation and sputtering should have the same microstructure. Therefore, it is somewhat surprising that the $\epsilon_1$ data agrees so well for these different films.

# CHAPTER VII. CONCLUSION

The stated objectives of this thesis have been achieved: (1) the design and construction of an automatic spectroscopic ellipsometer and (2) the microstructural characterization of palladium thin films prepared under varying deposition conditions. Through spectroellipsometry, the evolution of the microstructure of thin metal films was correlated to the changing deposition environment. A critical examination of different effective medium theories showed that the Pd films prepared by dc planar magnetron sputtering were best described by a new theory based on a random coated–particle microstructure where the grains are optically isolated from one another. This is significant as this theory has been applied to only one other material[96] and because of the striking confirmation by electron microscopy of the isolation of grains by void boundaries.

This thesis entailed the development of the spectroellipsometer from its conception including the individual testing and alignment of all the components and integration of the optical, hardware, and electronic sections of the ellipsometer through real–time data acquisition and control software. In addition, the microstructural analysis software was also developed for the characterization of thin films. It has been demonstrated in this thesis that the optical properties of thin metal films can provide quantitative microstructural information which can be related to other surface analysis techniques.

As has been shown, spectroscopic ellipsometry is a powerful surface analysis technique which can be applied to investigate a wide variety of topics in surface science of current interest. Foremost will be to study if the effective medium theory of Sen, Scala, and Cohen can be applied to other materials and deposition processes. With regard to palladium, there are several avenues of research worth exploring. Of

particular interest is the absorption of hydrogen into palladium and its effect on the microstructure and optical properties of palladium films. This absorption can be studied in real time to investigate the saturation and the subsequent deabsorption rate. Similarly, the optical properties of PdO, a semiconductor, are of interest and have not been well studied. Another interesting topic concerns the interface region between two deposited thin film layers, which is especially important in the microelectronics industry. It should be possible, as preliminary investigations have shown, to determine the composition and thickness of an interface between palladium and titanium for instance. As the interface forms as a result of either the surface microroughness of the first layer or the diffusion of one layer into the other, it should be possible to monitor in real-time how this region evolves under annealing for example. Measurement of the optical properties of the high-$T_c$ thin film superconductors is also an important, and currently unexplored, area of research. A particularly important measurement would be to observe how the dielectric function of these films evolves as the temperature is lowered past the superconducting transition temperature. With relatively minor modifications to the spectroellipsometer these measurements could be quickly performed. As well, the thin films could be characterized to determine how their microstructure is affected by the deposition conditions and post-deposition annealing in atmospheres of argon and oxygen for example.

# REFERENCES

1    R.M.A. Azzam and N.M. Bashara, *Ellipsometry and Polarized Light,* (North–Holland, Amsterdam, 1977).

2    E. Passaglia, R.R. Stromberg, and J. Kruger, Eds., *Ellipsometry in the Measurement of Surfaces and Thin Films* (National Bureau of Standards, Misc. Publ. 256, 1964).

3    N.M. Bashara, A.B. Buckman, and A.C. Hall, Eds., *Proceedings of the Symposium on Recent Developments in Ellipsometry* (North–Holland, Amsterdam, 1969); Surf. Sci **16**, (1969)..

4    N.M. Bashara and R.M.A. Azzam, Eds., *Proceedings of the Third International Conference on Ellipsometry* (North–Holland, Amsterdam, 1976); Surf. Sci. **56**, (1976).

5    R.H. Muller, R.M.A. Azzam, and D.E. Aspnes, Eds., *Proceedings of the Fourth International Conference on Ellipsometry* (North–Holland, Amsterdam, 1980); Surf. Sci. **96**, (1980).

6    F. Abeles, Ed., *Ellipsometry and other Optical Methods For Surface and Thin Film Analysis* J. de Physique **C10, Suppl. 12**, (1983).

7    E. Whittaker, *A History of the Theories of Aether and Electricity,* Vol. 1 (Nelson, London, 1951).

8·   A. Rothen, Ref. 2, p. 7.

9    A.C. Hall, Surf. Sci. **16**, 1 (1969).

10   A.B. Winterbottom, Ref. 2, p. 97.

11   E. Hecht and A. Zajac, *Optics,* (Addison–Wesley, 1974).

12   E.L. Malus, Nouvel Bull. Soc. Philomath. **1**, 266 (1808).

13   D. Brewster, Phil Trans. **105**, 125 (1815).

14   A. Fresnel, Oeuvres Vol. i, p 247, 767.

15      J. Jamin, Compt. Rend. **31**, 696 (1850).

16      L. Lorenz, Ann. Physik **3**, 460 (1860).

17      P. Drude, Ann. Physik **36**, 865 (1889).

18      Rayleigh, Phil. Mag. **33**, 1 (1892).

19      P. Drude, Ann. Physik **36**, 532 (1889).

20      M. Richartz and H. Hsu, J. Opt. Soc. Am. **39**, 136 (1949).

21      A. Rothen, Rev. Sci. Instr. **16**, 26 (1945).

22      B.D. Cahan and R.F. Spanier, Surf. Sci. **16**, 166 (1969).

23      D.E. Aspnes, Opt. Comm. **8**, 222 (1973).

24      D.E. Aspnes, Surf. Sci. **101**, 84 (1980).

25      D.E. Aspnes and A.A. Studna, SPIE Vol. **276**, 227 (1981).

26      D.E. Aspnes, in Ref. 6, p. 3.

27      D.E. Aspnes, Appl. Surf. Sci. **22/23**, 792 (1985).

28      D.E. Aspnes, in *Handbook of Optical Constants of Solids*, edited by E.D. Palik (Academic Press, New York, 1985) p 89.

29      D.E. Aspnes, in *Optical Properties of Solids: New Developments*, edited by B.O. Seraphin (North–Holland, Amsterdam, 1976) p. 799.

30      K. Vedam, P.J. McMarr, and J. Narayan, Appl. Phys. Lett. **47**, 339 (1985).

31      R.W. Collins, W.J. Biter, A.H. Clark, and H. Windischmann, Thin Solid Films, **129**, 127 (1985).

32      R.W. Collins, B.G. Yacobi, K.M. Jones, and Y.S. Tsuo, J. Vac. Sci. Technol. A **4**, 153 (1986).

33    D.E. Aspnes and A.A. Studna, Phys. Rev. B **27**, 985 (1983).

34    D.E. Aspnes, S.M. Kelso, R.A. Logan, and R. Bhat, J. Appl. Phys. **60**, 754 (1986).

35    P.S. Hauge, SPIE Vol **88**, 3 (1976).

36    P.S. Hauge, Surf. Sci. **96**, 108 (1980).

37    R.H. Muller, Surf. Sci. **56**, 19 (1976).

38    W. Budde, Appl. Opt. **1**, 201 (1962).

39    C.V. Kent and J. Lawson, J. Opt. Soc. Am. **27**, 117 (1937).

40    R. Greef, Rev. Sci. Instr. **41**, 532 (1970).

41    S.N. Jasperson and S.E. Schnatterly, Rev. Sci. Instr. **40**, 761 (1969).

42    P.S. Hauge and F.H. Dill, IBM J. Res. Develop. **17**, 472 (1973).

43    D.E. Aspnes, Appl. Opt. **14**, 1131 (1975).

44    W.E.J. Neal, Surf. Technol. **6**, 81 (1977).

45    W.E.J. Neal, Appl. Surf. Sci. **2**, 445 (1979).

46    W.-K. Paik, in *Physical Chemistry, Series 1, Vol. 6*, edited by J. O'M. Bockris (Butterworth, London, 1973) p. 239.

47    W.A. Shurcliff, *Polarized Light* (Harvard Press, Cambridge, Mass., 1962).

48    J.D. Jackson, *Classical Electrodynamics* 5th ed. (Wiley, New York, 1975).

49    M. Born and E. Wolf, *Principles of Optics*, 5th ed. (Pergamon, Oxford, 1975).

50    R.H. Muller, Surf. Sci. **16**, 14 (1969).

51    J.M. Bennett and H.E. Bennett, in *Handbook of Optics*, Section 10, (Optical Society of America, 1978).

52    P.S. Hauge, R.H. Muller and C.G. Smith, Surf. Sci. **96**, 81 (1980).

53    D.E. Aspnes, J. Opt. Soc. Am **64**, 812 (1974).

54    D.E. Aspnes and A.A. Studna, Appl. Opt. **14**, 220 (1975).

55    A.R. Reinberg, Appl. Opt. **11**, 1273 (1972).

56    D. Charlot and A. Maruani, Appl. Opt. **24**, 3368 (1985).

57    H. Arwin and D.E. Aspnes, Thin Solid Films **113**, 101 (1984).

58    H. Arwin and D.E. Aspnes, Thin Solid Films **138**, 195 (1986).

59    S.S. So and K. Vedam, J. Opt. Soc. Am. **62**, 16 (1972).

60    P. Yeh, Surf. Sci. **96**, 41 (1980).

61    P.J. Lin–Chung and S. Teitler, J. Opt. Soc. Am. A **1**, 703 (1984).

62    D.E. Aspnes and A.A. Studna, Rev. Sci. Instr. **49**, 291 (1978).

63    P.L. Land, Rev. Sci. Instr. **42**, 420 (1971).

64    D.E. Aspnes and A.A. Studna, SPIE Vol **112**, 62 (1977).

65    J.F. Nye, *Physical Properties of Crystals* (Oxford University Press, 1957).

66    H.G. Jerrard, J. Opt. Soc. Am. **38**, 35 (1948).

67    Brian Chapman, *Glow Discharge Processes*, (John Wiley & Sons, New York, 1980), Ch. 6.

68    J.L. Vossen and W. Kern, *Thin Film Processes* (Academic Press, New York, 1978).

69    R.F. Bunshah *et al.*, Eds., *Deposition Technologies for Films and Coatings* (Noyes Publications, New Jersey, 1982) p. 170.

70    J.A. Thornton, Ann. Rev. Mater. Sci., **7**, 239 (1977).

71    J.A. Thornton, J. Vac. Sci. Technol., A **4**, 3059 (1986).

72    J.A. Thornton, Surf. Engineering **2**, 283 (1986).

73    D.E. Aspnes, Surf. Sci. **135**, 284 (1983).

74    D.E. Aspnes, J. Opt. Soc. Am. **64**, 639 (1974).

75    D.E. Aspnes, *Private Communication*, April, 1986.

76    D.E. Aspnes, E. Kinsbron, and D.D. Bacon, Phys. Rev. B **21**, 3290 (1980).

77    D.E. Aspnes, Thin Solid Films **89**, 249 (1982).

78    D.E. Aspnes, J. Vac. Sci. Technol., **18**, 289 (1981).

79    D.E. Aspnes, in *Basic Properties of Optical Materials*, edited by A. Feldman (National Bureau of Standards, Special Publication 697, 1985).

80    D.E. Aspnes, SPIE Vol. **276**, 188 (1981).

81    D.E. Aspnes, J.B. Theeten and F. Hottier, Phys. Rev. B, **20**, 3292 (1979).

82    J.R. Blanco, P.J. McMarr, and K. Vedam, Appl. Opt., **24**, 3773 (1985).

83    R.W. Collins and C.J. Tuckerman, J. Vac. Sci. Technol., A **4**, 2343 (1986).

84    N. Draper and H. Smith, *Applied Regression Analysis, 2nd Ed.* (John Wiley and Sons, New York, 1981).

85    P.E. Gill, W. Murray, and M.H. Wright, *Practical Optimization* (Academic Press, New York, 1981).

86    E.S. Keeping, *Introduction to Statistical Interference* (van Nostrand, Princeton, 1962) Ch. 12.

87    D.E. Aspnes, Am. J. Phys. **50**, 704 (1982).

88    L. Lorenz, Ann. Phys. Chem. **11**, 70 (1880).

89    H.A. Lorentz, *Theory of Electrons* (Teubner, Leipzig, 2nd edn., 1916).

90    P. Rouard and A. Meessen, in *Progress in Optics, Vol. 15*, edited by E. Wolf (North–Holland, Amsterdam, 1977) p. 79.

91    J.C. Maxwell Garnett, Philos. Trans. R. Soc. London **203**, 385 (1904).

92    J.C. Maxwell Garnett, Philos. Trans. R. Soc. London, Ser. A **205**, 237 (1906).

93    D.A.G. Bruggeman, Ann. Phys. **24**, 636 (1935).

94    P.N. Sen, C. Scala, and M.H. Cohen, Geophysics, **46**, 781 (1981).

95    D.E. Aspnes, Phys. Rev. B **33**, 677 (1986).

96    D.E. Aspnes and H.G. Craighead, Appl. Opt. **25**, 1299 (1986).

97    T. Hanai, in *Emulsion Science*, edited by P. Sherman, (Academic, New York, 1968), pp. 353–478.

98    D.J. Bergman, Phys. Rev. Lett. **44**, 1285 (1980).

99    G.W. Milton, Appl. Phys. Lett. **37**, 300 (1980).

100   D.J. Bergman, Ann. Phys. **138**, 78 (1982).

101   D.E. Aspnes, Phys. Rev. B **25**, 1358 (1982).

102   D.M. Gay, ACM Trans. Math. Soft. **9**, (1983).

103   R. Fletcher, Computer Journal **13**, 317 (1970).

104    R. Fletcher, *FORTRAN Subroutines for Minimization by Quasi-Newton Methods* (Atomic Energy Research Establishment, Harwell, England, Report 7125, 1972).

105    B.T. Sullivan and R.R. Parsons, to be published in Thin Solid Films, proceedings of the 14th International Conference on Metallurgical Coatings, San Diego, 1987.

106    B.T. Sullivan and R.R. Parsons, submitted to J. Vac. Sci. Technol. A, March 1987

107    B.T. Sullivan and R.R. Parsons, submitted to J. Vac. Sci. Technol. A, May 1987

108    J.A. Thornton, in *Deposition Technologies for Films and Coatings*, edited by R.F. Bunshah *et al.* (Noyes Publications, NJ, 1982), p. 170.

109    R. Messier, J. Vac. Sci. Technol. A **4**, 490 (1986).

110    D.W. Hoffman and J.A. Thornton, Thin Solid Films **40**, 355 (1977).

111    D.W. Hoffman and J.A. Thornton, J. Vac. Sci. Technol. **17**, 380 (1980).

112    J.A. Thornton and D.W. Hoffman, J. Vac. Sci. Technol. **18**, 203 (1981).

113    H.D. Hadstrum, in *Inelastic Ion Surface Collisions*, edited by N.H. Tolk, J.C. Tully, W. Heiland, and C.W. White (Academic, New York, 1977), p. 1.

114    E. Kay, F. Parmigiani, and W. Parrish, J. Vac. Sci. Technol. A, **5**, 44 (1987).

115    J.R. Blanco, K. Vedam, P.J. McMarr, and J.M. Bennett, in *Multiple Scattering of Waves*, edited by V.V. Varadan and V.K. Varadan (Technomic Publ. Co., Lancaster, PA, 1986).

116    D.P. Arndt, R.M.A. Azzam, J.M. Bennett, J.P. Borgogno, C.K. Carniglia, W.E. Case, J.A. Dobrowolski, U.J. Gibson, T.T. Hart, F.C. Ho, V.A. Hodgkin, W.P. Klapp, H.A. Macleod, E. Pelletier, M.K. Purvis, D.M. Quinn, D.H. Strome, R. Swenson, P.A. Temple, and T.F. Thonn, Appl. Opt., **23**, 3571 (1984).

117    T.C. Huang, G. Lim, F. Parmigiani, and E. Kay, J. Vac. Sci. Technol., A **3**, 2161 (1985).

118    J.L. Vossen and J.J. O'Neill, Jr., RCA Rev. **29**, 566 (1968).

119    J.L. Vossen, J.J. O'Neill, K.M. Finlayson, and L.J. Royer, RCA Rev. **31**, 293 (1970).

120    J.L. Vossen, J. Vac. Sci. Technol. **8**, S12 (1971).

121    R. Messier, A.P. Giri, and R.A. Roy, J. Vac. Sci. Technol. A **2**, 500 (1984).

122    P. Dixit and R.W. Vook, Appl. Surf. Sci. **24**, 239 (1985).

123    N. Laegreid and G.K. Wehner, J. Appl. Phys. **32**, 365 (1961).

124    H. Oechsner, Z. Phys. **261**, 37 (1973).

125    J.A. Thornton and A. Penfold, in Thin Film Processes, edited by J.L. Vossen and W. Kern, (Academic Press, New York, 1978), p. 99.

126    J.L. Vossen and J.J. O'Neill, Jr., RCA Rev. **31**, 276 (1970).

127    J.J. Cuomo, R.J. Gambino, and R. Rosenberg, J. Vac. Sci. Technol. **11**, 34 (1974).

128    R.D. Bland, G.J. Kominiak, and D.M. Mattox, J. Vac. Sci. Technol. **11**, 671 (1974).

129    D.M. Mattox, in *Deposition Technologies for Films and Coatings*, edited by R.F. Bunshah *et al.* (Noyes Publications, NJ, 1982), p. 224.

130    J.H. Weaver, C. Krafka, D.N. Lynch, and E.E. Koch, in *Physics Data: Optical Properties of Metals*, Fachinformationszentrum Energie, Physik, Mathematik GmBH, Karlsruhe, 1981, pp. 178–189.

131    R.C. Vehse, E.T. Arakawa, and M.W. Williams, Phys. Rev. B **1**, 517 (1970).

132    Zh. Duisebaeva, M.I. Korsumskii, and G.P. Motulevich, Opt. Spectrosc. **37**, 82 (1974).

133    P.B. Johnson and R.W. Christy, Phys. Rev. B **9**, 5056 (1974).

134     J.H. Weaver, Phys. Rev. B **11**, 1416 (1975).

135     J.H. Weaver and R.L. Benbow, Phys. Rev. B **12**, 3509 (1975).

136     J. Lafait, *Proc. Int. Conf. on Physics of Transition Metals, Toronto, 1977*: Inst. Phys. Conf. Ser. **39**, 130 (1978).

137     J. Lafait, F. Abeles, M.L. Theye and G. Vuye, J. Phys. F **8**, 1597 (1978).

138     A. Y-C. Yu and W.E. Spicer, Phys. Rev. **168**, 497 (1968).

139     F. Meyer, J.H.J.M. Buster, B.G. Bagley, and D.E. Aspnes, J. Non-Cryst. Solids **34**, 441 (1979).

140     J.T. Lue, H.-W. Chen, and S.-I. Lew, Phys. Rev. B **34**, 5438 (1986).

141     P.O. Nilsson and M.S. Shivaraman, J. Phys. C **12**, 1423 (1979).

142     S.M. Shivaprasad, L.A. Udachan, and M.A. Angadi, Phys. Lett. **78A**, 187 (1980).

143     S.M. Shivaprasad and M.A. Angadi, J. Phys. D **13**, L171 (1980).

144     G.A. Niklasson, D.E. Aspnes, and H.G. Craighead, Phys. Rev. B **33**, 5363 (1986).

## PUBLICATIONS

B.T. Sullivan and R.R. Parsons, "Investigation of RF-Induced Substrate Biasing on the Sputter Deposition and Microstructure of Palladium Films," submitted to J. Vac. Sci. Technol. A, May 1987.

Z.H. Li, B.T. Sullivan and R.R. Parsons, "Application of the 4x4 Matrix Method to Magneto-Optical Recording Media," submitted to Applied Optics.

G. Rostoker and B.T. Sullivan, "Polarization Characteristics of Pc5 magnetic Pulsations in the Dusk Hemisphere," Planet. Space Sci. 35 (1987) 429.

B.T. Sullivan and R.R. Parsons, "A Spectroellipsometric Investigation of the Effect of Argon Partial Pressure on Sputtered Palladium Films," to be published in J. Vac. Sci. Technol A.,

B.T. Sullivan and R.R. Parsons, "Effect of Substrate Temperature on the Microstructure of Palladium Thin Films," to be published in the proceedings of the 14th International Conference on Metallurgical Coatings, San Diego, California, 1987.

B.T. Sullivan and R.R. Parsons, "Kinetics of Bound Excitons and Multi-Exciton Complexes in Si(B)," Can. J. Phys. 61 (1983) 288.

B.T. Sullivan and W. Israel, "The Third Law of Black Hole Mechanics: What is it?," Phys. Lett. 79A (1980) 371.